Development and characterization of carbon nanofiber/carbon nanotube/graphene reinforced aluminum matrix composite

（カーボンナノファイバー/カーボンナノチューブ/グラフェン強化アルミニウムマトリックス複合材料の開発と特性評価）

September 2020

GAO FEI

Development and characterization of carbon nanofiber/carbon nanotube/graphene reinforced aluminum matrix composite
(カーボンナノファイバー/カーボンナノチューブ/グラフェン強化アルミニウムマトリックス複合材料の開発と特性評価)

Dissertation for the Degree of
Doctor of Philosophy

Department of Mechanical System Engineering

Graduate School of Engineering

Hiroshima University, Japan

Associate Professor Choi Yong Bum, Advisor

GAO FEI

September 2020

CONTENTS

Chapter 1 Background and objectives

Contents *1*

1.1 Introduction *2*

1.2 Thermal management solution for electric and electronic component *4*

  1.2.1 Trends of thermal management solution *4*

  1.2.2 Development the commercialized heat sink materials *7*

1.3 Previous studies on MMCs for thermal management *10*

1.4 Fabrication processes of MMCs *15*

1.5 Problems of previous studies and objective of this study *18*

1.6 Outline of this thesis *20*

Reference *22*

Chapter 2 Development and characterization of porous VGCF/MP by spacer method

Contents *27*

2.1 Introduction *28*

2.2 Manufacturing process of porous VGCF/MP and characterization *30*

  2.2.1 Raw materials *30*

  2.2.2 Manufacturing process and carbonization of porous VGCF/MP *32*

  2.2.3 Observation of microstructure of porous VGCF/MP *35*

  2.2.4 Porosity of porous VGCF/MP *36*

  2.2.5 Test of compressive property and TC of porous VGCF/MP *37*

2.3 Result and Discussion *40*

2.3.1 Effect of volume fraction of NaCl Particles on microstructure and porosity of porous VGCF/MP 40

2.3.2 Effect of carbonization on porous VGCF/MP 45

2.3.3 Effect of Mixing method on closed pores of porous VGCF/MP 48

2.3.4 Compressive strength of porous VGCF/MP 50

2.3.5 TC of porous VGCF/MP...53

2.4 Summary 55

Reference...56

Chapter 3 Development of VGCF/MP reinforced al matrix composite by low pressure infiltration method and their thermal property

Contents 58

3.1 Introduction 59

3.2 Experimental..60

3.2.1 Raw materials and preparation of the porous VGCF/MP............................60

3.2.2 Fabrication of VGCF/MP/Al composites by LPI method...............................61

3.2.3 Characterization of microstructure, porosity, and thermal conductivity.......66

3.3 Results and Discussion 67

3.3.1 Effect of volume fraction ratio of VGCF and MP on the Microstructure and porosity of the porous VGCF/MP 67

3.3.2 Microstructure of the VGCF/MP/Al composites 70

3.3.3 TC of porous VGCF/MP and VGCF/MP/Al composites 75

3.4 Summary 77

Reference...79

Chapter 4 Microstructure and thermal conductivity of carbon nanotube block reinforced aluminum matrix composite

Contents *82*
4.1 Introduction *83*
4.2 Experimental *84*
  4.2.1 Raw materials and electroless Cu plating on CNT block *84*
  4.2.2 Fabrication of CNT block/Al composite and characterization *88*
4.3 Results and Discussion *89*
  4.3.1 Effect of plating time on the thickness of the Cu layer *89*
  4.3.2 Microstructure of the CNT block/Al composites *93*
  4.3.3 Thermal stress at the interface between CNT block and Al matrix *98*
  4.3.4 TC of the CNT block/Al composites *102*
4.4 Summary *104*
Reference *105*

Chapter 5 Development of graphene reinforced aluminum matrix composite by spark plasma sintering

Contents *108*
5.1 Introduction *109*
5.2 Experimental *110*
5.3 Results and Discussion *113*
  5.3.1 Observation of composite powders *113*
  5.3.2 Microstructures and phase analysis of Graphene/Al composites *114*
  5.3.3 TC and hardness of Graphene/Al composites *119*
5.4 Summary *121*
Reference *122*

Chapter 6 Conclusion

Conclusion *123*

List of Figures

Fig. 1.1 Various processes of fabrication of MMCs.

Fig. 1.2 The longitudinal cross-section of one-direction arrayed CF/Al composite with mountain shape.

Fig. 2.1 Images of raw material: (a) VGCFs; (b) MP; and (c) NaCl particles.

Fig. 2.2 Schematic diagram of fabrication process of porous VGCF/MP.

Fig. 2.3 Photo of carbonization furnace.

Fig. 2.4 Device of compressive strength test.

Fig. 2.5 Schematic view of a thermal conductivity measuring device.

Fig. 2.6 SEM images of porous VGCF/MP (sample No. 1).

Fig. 2.7 Porosity of porous VGCF/MP with different volume fractions of NaCl particles.

Fig. 2.8 SEM images of the porous VGCF/MP: (a), (b), and (c) porous VGCF/MP with total porosity is 75.09%, 83.76%, and 91.51%, respectively; (d), (e), and (f) higher magnification images of each porous VGCF/MP, respectively

Fig. 2.9 SEM images of the cell wall of porous VGCF/MP: (a) low magnification, (b) and (c)high magnification.

Fig. 2.10 TEM images of porous VGCF/MP: (a) before carbonization, and (c) after carbonization; (b) and (d)high magnification TME images of locations of (a) and (c), respectively.

Fig. 2.11 TEM images of MP insert with FTT: (a) before carbonization, and (b) after carbonization.

Fig. 2.12 XRD patterns of as-received, before and after carbonization MP, and *FWHM of (002) corresponding pattern. (*FWHM: full width at half maximum).

Fig. 2.13 Microstructures of porous VGCF/MP fabricated (fabricated with 90 vol.% NaCl particles) fabricated by different mixing method.

Fig. 2.14 Compressive stress–strain curve of porous VGCF/MP with different porosity and same fraction of raw materials (VGCF: MP= 3:7) before carbonization.

Fig. 2.15 Compressive stress-strain curves of 83.76 % total porosity porous VGCF/MP (VGCF: MP= 3:7) before carbonization.

Fig. 2.16 Schematic diagram cracks in each region.

Fig. 2.17 Photograph of porous VGCF/MP after compressive strength test.

Fig. 2.18 TC of porous VGCF/MP with different porosity before carbonization and porous aluminum alloy 6011

Fig. 2.19 TC of porous VGCF/MP (total porosity:75.09%, VGCF:MP=3:7) before and after carbonization.

Fig. 3.1 Schematic description of the forces exerted on the flowing melt in a capillary tube, where P_{ram}, P_{cap}, P_{back}, f and G are externally applied pressure, capillary resistance pressure, back pressure, internal viscous friction of the melt and gravity, respectively.

Fig. 3.2 Schematic of the fabrication process for preparing the VGCF/MP/Al composites.

Fig. 3.3 SEM images of porous VGCF/MP: (a) only MP and before carbonization, (b) only MP and after carbonization, (c) MP & 0.5 vol.% VGCFs and after carbonization, and (d) MP & 3 vol.% VGCFs and after carbonization (the inserts are higher magnification images of each porous VGCF/MP's cell wall).

Fig. 3.4 Porosity of porous VGCF/MP with different fabricated conditions.

Fig. 3.5 BSE image of electroless Ni plated porous VGCF/MP (only MP and before carbonization) buried by resin.

Fig. 3.6 SEM images of VGCF/MP/Al composites: (a) with only MP and before carbonization, (b) with only MP and after carbonization, (c) with MP & 0.5 vol.% VGCFs and after carbonization, and (d) with MP & 3 vol.% VGCFs and after carbonization.

Fig. 3.7 SEM images of interface between VGCF/MP and Al matrix: (a) with MP & 0.5 vol.% VGCFs and after carbonization; (b), and (c) with MP & 3 vol.% VGCFs and after carbonization.

Fig. 3.8 Schematic of of interface between VGCF/MP and Al matrix: (a) with MP & 0.5 vol.% VGCFs and after carbonization; (b), and (c) with MP & 3 vol.% VGCFs and after carbonization.

Fig. 3.9 Element distribution of VGCF/MP/Al composites fabricated with condition of MP & 0.5 vol.% VGCFs and after carbonization: (a) BSE image (inset for location and result of point analysis), (b) Al element, (c) C element, and (d) Ni element.

Fig. 3.10 TC of (a) porous VGCF/MP and (b) VGCF/MP/Al composites with different fabricated conditions.

Fig. 4.1 SEM image of as received CNT blocks.

Fig. 4.2 Schematic diagram of electroless Cu plating on CNT blocks.

Fig. 4.3 Schematic image of fabrication process of CNT block/Al composites.

Fig. 4.4 SEM images of (a), (c), (e), and (g) electroless Cu-plated CNT blocks of 15, 30, 60, and 180 s and (b), (d), (f), and (g) higher magnification of electroless Cu-plated layer of each sample, respectively.

Fig. 4.5 BSE images of cross section of electroless Cu-plated CNT blocks with different plating times: (a) 15 s, (b) 30 s, (c) 60s, and (d) 180s.

Fig. 4.6 Relation of thicknesses of Cu layers on electroless Cu-plated CNT blocks with different plating times.

Fig. 4.7 SEM images of microstructures fabricated CNT block/Al composites with different CNT block:Cu volume ratios: (a) 8.8:1.2, (c) 7.9:2.1, (e) 6.8:3.2, and (g) 3.7:6.3; (b), (d), (f), and (h) high-magnification images of (a), (c), (e), and (g), respectively.

Fig. 4.8 Element distribution of fabricated CNT block/Al composite fabricated with condition of CNT block:Cu volume ratio of 3.7:6.3: (a) BSE image (inset for location and result of EPMA), (b) C element, (c) Al element, and (d) Cu element.

Fig. 4.9 XRD patterns of fabricated CNT block/Al composites with different CNT block:Cu volume ratios.

Fig. 4.10 The schematic diagram of shrinkage of CNT block/Al composite.

Fig. 4.11 (a) Temperature and (b) cooling rate of sample on condition of furnace cooling.

Fig. 4.12 Thermal stress on the interface between CNT block and Al matrix.

Fig. 4.13 TCs of fabricated CNT block/Al composites with different CNT block:Cu volume ratios.

Fig. 5.1 SEM image of as received (a) graphene particles and (b) aluminum powders.

Fig. 5.2 The schematic of the fabrication process for preparing the Graphene/Al composites.

Fig. 5.3 SEM images of powder composites fabricated by (a) V-type mixing and (b) by planetary ball milling.

Fig. 5.4 SEM images of Graphene/Al composites (10 vol.% graphene) with different sintering temperatures: (a) 773K, (c) 793K and (e) 813K; high magnifications of (a), (c) and (e), respectively.

Fig. 5.5 SEM images of Graphene/Al composite with different volume fractions: (a) 10 vol.%, (c) 20 vol.% and (e) 30 vol.%; high magnifications of (a), (c) and (e), respectively.

Fig. 5.6 Interface of Graphene/Al composite.

Fig. 5.7 (a) Defects in 10 vol.% Graphene/Al composite and its element distribution: (b) BSE image, (c) C element and (d) Al element.

Fig. 5.8 XRD pattern of 10 vol.% Graphene/Al composite.

Fig. 5.9 TC of Graphene/Al composites with different volume fraction of graphene.

Fig. 5.10 TC of Graphene/Al composites with different volume fraction of graphene.

List of Tables

Table 1.1 Thermal management solutions in recently years.

Table 1.2 The development of the commercialized heat sink materials and application.

Table 1.3 Thermal properties and density of several semiconductor materials, aluminum and copper.

Table 1.4 Density and thermal properties of materials as reinforcements and matrices for the fabrication of MMCs.

Table 1.5 Thermal properties of the various MMCs.

Table 2.1 Volume fraction of raw material and mixing method to fabricated porous VGCF/MP.

Table 3.1 Parameters of molten Al infiltrate to porous VGCF/MP.

Table 3.2 Fabricated conditions of porous VGCF/MP.

Table 4.1 Properties of Cu and Ni.

Table 4.2 Bathes used in electroless Cu plating of each step.

Table 4.3 Thicknesses of Cu layer and CNT block:Cu volume ratios with different plating times.

Table. 4.4 CTE and elastic modulus of CNT and Al.

Table 5.1 Fabrication conditions of Graphene/Al composites.

Chapter 1

Background and Objectives

Contents

Contents *1*

1.1 Introduction *2*

1.2 Thermal management solution for electric and electronic component *4*

1.2.1 Trends of thermal management solution *4*

1.2.2 Development the commercialized heat sink materials...................................... *7*

1.3 Previous studies on MMCs for thermal management.. *10*

1.4 Fabrication processes of MMCs.. *15*

1.5 Problems of previous studies and objective of this study *18*

1.6 Outline of this thesis *20*

Reference.. *22*

1.1 Introduction

Since 21st century, electric and electronic devices are widely used in daily life and industrial production, such as personal computer, automobiles and commercial server. Electric and electronic devices have made remarkable development with the invention and innovation of the technologies. However, increasing power densities and miniaturization are the development trends of high-performance electric and electronic devices. Otherwise, the generated heat will lead to the overheat of the CPU. Thus, to solve this problem, manufactured heat sink with high thermal conductivity (TC) are need for the stability and lifetime of CPU. Moreover, the heat sink materials were basically required coefficient of thermal expansion (CTE) matching to the heat generation components for avoiding thermal stress. But the conventional heat sink materials, such as aluminum and copper, cannot simultaneously meet both of them. Thus, new materials were developed to solve this problem, such as new alloy and composites. Especially, composites are considered having the tailorable TC and CTE by controlling the addition of the reinforcement in matrix. According matrix, composite can be classified as metal matrix composites (MMCs), ceramic matrix composites (CMCs) and polymer matrix composites (PMCs). Especially, the aluminum has a relatively high TC among metals and about 1/3 weight of steels. Thus, the aluminum as the matrix in composites is attribute to the application to portable electronic devices, automobiles and other fields. Even if the CTE of Al is much higher than that of the electronic components such as semiconductors, the CTE of Al-based composites can be controlled by reinforcement. A range of materials have been considered for use as reinforcements in Al-based heat sink composite materials, including silicon carbide (SiC), aluminum nitride (AlN), and various carbon materials. The recently developed carbon nano fibers (CNFs) and carbon nano tube (CNT) are promising because of their outstanding TCs and low CTE, high strength and light weight. Therefore, the CNF or CNT reinforced Al-based composites are expected to replace the conventional heat sink materials, such as aluminum and copper. On the other hand, the fabrication process for composites is one of the key factors in terms that the cost is a limitation of MMCs to industrial production. The die casting process for the MMCs is developed in recently years. However, this method requires high presssure raised the production cost by the complex production equipment. While, the low-pressure infiltration (LPI) method has been used to fabricate MMCs with high volume fractions of reinforcements. In this method, a molten metal is infiltrated into a porous preform at a low pressure the casting process using low pressures, which is thought be attribute to the industrial production of Al-based composites. Therefore, the CNFs or CNTs reinforced Al-based composites fabricated by the LPI method is the promising candidate in the heat sink materials.

1.2 Thermal management solution for electric and electronic component

1.2.1 Trends of thermal management solution

In the electric and electronic component fields, the components have been becoming high power capacity according to increasing power consumption with the industrial development. The metal–oxide–semiconductor field-effect transistor (MOSFET) is the basic building block of modern electronics, such as central processing unit (CPU). Since 1971 to 2019, the MOSFET technology node is evolved from 10 μm to 7 nm. However, since2005, the CPU's clock speed is usually less than or equal to 4GHz, which is owing to the clock speed higher than 4GHz leading to the generation a lot of heat under working conditions [1]. Besides, the hybrid electric vehicle (HEV) systems or electric vehicle (EV) systems in the transportation fields is focused in recently years for the reduction of carbon emissions [2]. The power battery is the core of the new energy vehicle. The optimal operating temperature range of the power battery is generally within a narrow window of 20-35 ℃. The temperature directly affects the life, performance and safety of the battery system. It can be found that, in the electric and electronic component fields, components are undergoing a revolution because of a number of key factors: increasing power consumption; increasing reliability requirements; increasing lifetime; light weight and cost constraints [1-3]. Thus, the thermal management solution become a challenge of the modern electronic industry for its increasing required properties.

The worldwide market for thermal management products is predicted to grow from about $8.8 billion in 2013 to $15.56 billion by 2018, at an average annual growth rate of 12.1% [4]. Many commercial thermal management solutions using advanced technologies have been developed by the companies in all over the world. In Japan, Panasonic Corp. developed many new material or air-cooling components, such as a graphite sheet (PGS) as thermal interface material (TIM) for the power module of automotive LED, server and etc.; and cooling fan with unique hydro dynamic bearing be able to use in wide operating temperature range (-40~105 °C) for the LED-headlamp and DC-DC converter of HEV or EV systems in automobile [5]. As most servers are packed in cabinet which result heat generated in a small pace. Thus, heat exchangers are designed compacted. In USA, Ice Qube, Inc. is providing the Qube Series of air conditioners, which the company described as the world's smallest (widths as narrow as six inches) compressor-based air conditioner and an ideal cooling solution for compact enclosures with high heat loads. ACT designed and manufactured HiK™ plates are aluminum or aluminum silicon carbide heat spreaders having embedded heat pipes for insulated gate bipolar transistor (IGBT) heat spreaders or high power lasers and LEDs [6]. In the field of HEV and EV, the modern computational fluid dynamics (CFD) simulation software developed by Siemens for challenging problems predicts the temperature and airflow distribution, which helps determine high-temperature locations and airflow deficiencies [7]. Besides, advanced solid-state lithium battery thermal management have been developed by Koolkwic from the USA [8]. This technology no need for liquid cooling circuits within the battery pack, which has a benefit to health and safety of the passengers in the HEV or the EV. In Germany, NORMA Group manufactured the pipes from thermoplastics by thermal simulation to reduce their weight by around 30 percent compared with conventional elastomer pipes. Due to the lower weight, less drive energy is required, relieving the load on the battery cells and generating less heat [9]. These thermal management solutions are summarized in Table 1.1.

For operating high power devices at peak condition, the components mentioned above was produced to solve the problem of high heat generation. The heat sink is a key part of thermal management solution, which is in urgent need to develop the high-performance materials with outstanding TC and matchable CTE to replace the traditional heat sink materials, such as aluminum and copper. Moreover, the novel fabrication processes of heat sink materials are also needed to meet the demand of increasing thermal management solution's market.

Table 1.1 Thermal management solutions in recently years.

Company	Application	Country	Ref.
Panasonic Corp.	PGS as thermal interface material (TIM) for the power module; cooling fan for LED or DC-DC converter	Japan	[5]
Ice Qube	Qube Series of air conditioners for server	USA	[10]
ACT	HiK™ plates for IGBT heat spreaders or high-power lasers and LEDs	USA	[6]
Siemens	CFD simulation software for EV or HEV	Germany	[7]
Koolkwic	Solid-state lithium battery for EV or HEV	USA	[8]
NORMA Group	Light weight pipes for reduce heat generation in EV or HEV	Germany	[9]

1.2.2 Development the commercialized heat sink materials

Driven by the development of electric and electronic devices, the market of thermal management solution expanded dramatically. Most of the share of commercialized heat sink materials is aluminum and copper. However, the aluminum and copper cannot meet the need of high-power electric and electronic devices. Therefore, many companies were focused on the development of commercialized heat sink material with high performance to meet the demand. Moreover, as metal has a relatively high TC and low price, many kinds of metal matrix composites were developed in recently years. As the typical of advanced industrial country, the Japan and the USA have a lot of companies concentrating on developing the advanced heat sink materials. In Japan, FJ composite developed a series of multilayered MMCs named "S-CMC® (super CMC)". These series MMCs contains molybdenum reinforced Cu-based (Mo/Cu) composites and tungsten reinforced Cu-based (W/Cu) composites. And a kind of carbon reinforced Al-based composite were also developed by FJ composite. These can be applied to various semiconductor fields, and particularly suitable as a heat sink for GAN elements used for 4G / 5G communication [11]. Denka Co., Ltd. Developed Al-diamond composites for the application of medical equipment and high frequency device of communication satellite [12]. A.L.M.T. Corp. developed a series of Mg-SiC, Ag-diamond, and Cu-Mo composites for the application of the IGBT module, high power devices, and 4G / 5G communication, respectively [13]. For the inexpensive raw material cost and significant process cost reduction, JFE Precision Co. developed the Cr-Cu composite for optical communication module, 4G/5G communication module, inverter of vehicle, and LED etc [14]. Japan Fine Ceramics CO.,LTD. also developed a series of SiC/Al and SiC/Al composites for application of asteroid probe and large machine tools [15]. From the USA, Edgetech Industries LLC [16], S-Bond Technologies [17], Material innovations Inc. [18], and CPS Technologies Corp. [19] have developed and produced diverse composite materials with high performance thermal dissipation for the heat sink applications. Those companies mainly developed Mo/Cu, and W/Cu Si/Al SiC/Al, C/Al and SiC/Si composites for the heat sink. The development of the commercialized heat sink materials and application in those companies is summarized in Table 1.2.

Table 1.2 The development of the commercialized heat sink materials and application.

Company	Applications	Materials	Country	Ref.
FJ composite	4G/5G communication	Mo/Cu, W/Cu and C/Al composites	Japan	[11]
Denka Co., Ltd.	Medical equipment communication satellite	Al-diamond composites		[12]
A.L.M.T. Corp.	IGBT module, high power devices, and 4G/5G communication	Mg-SiC, Ag diamond, and Cu-Mo composites		[13]
JFE Precision Co.	4G/5G communication, inverter of vehicle, and LED	Cr-Cu composite		[14]
Japan Fine Ceramics CO.,LTD.	Asteroid probe and large machine tools	SiC/Al and SiC/Al composite		[15]
Edgetech Industries LLC.	Power transistors and optoelectronics	Mo/Cu and W/Cu composite	USA	[16]
S-Bond Technologies	Avionics	Si/Al composites		[17]
Material innovations Inc.	Commercial avionics	Graphite fibers and preforms reinforced MMCs		[18]
CPS Technologies Corp.	IGBT baseplates and heat spreaders	SiC/Al		[19]

1.3 Previous studies on MMCs for thermal management

As mentioned in above chapters, there are a lot of efforts have been done on thermal management solution to meet the require of the electric and electronic devices developed in recently years. Specifically, under working condition, a lot of heat is generated by the high-power electric and electronic devices. With insufficient thermal diffusion, the temperature of those devices may be increased by the generated heat. As semiconductor chips in those devices have to be operating in their temperature ranges, otherwise their operation efficiency may be decreased, even cause the overheat. As semiconductors chip are manufactured by several kinds of semiconductor, which have a relatively low CTE with the range from 2.8 to 5.9 × 10^{-6} K^{-1}. The thermal properties

Table 1.3 Thermal properties and density of several semiconductor materials, aluminum and copper.

Materials	CTE [$\times 10^{-6}$ K^{-1}]	TC [$W \cdot m^{-1} \cdot K^{-1}$]	Density [$g \cdot cm^{-3}$]	Ref.
AlGaAs	5.2	90	2.3	[20]
GaAs	5.8~5.9	46~58	5.3	[21-23]
GaN	3.2	150	6.1	[22]
Ge	5.8~5.9	58~60	5.3	[24]
InP	4.5	68	4.81	[25]
Si	2.8~4.2	139~150	2.3~2.34	[21, 22, 26]
SiC	2.8~5.0	80~490	3.1~3.21	[21, 22]
SiGe	5.2	130	3.8	[27]
Al	22.3	237	2.7	[21-23]
Cu	16.5-17	385	6.9	[21-23]

of the representative semiconductors are listed in Table 1.3. Therefore, thermal tress may be caused by the unmatchable CTE of heat sink. In total, the heat sink material is closely related to the lifetime and stability of the electric and electronic devices. Specifically, the required properties of heat sink materials are as high as TC and matchable CTE. The conventional heat sink materials had considerable difficulties to may be caused by the unmatchable CTE of heat sink. In total, the heat sink material is closely related to the lifetime and stability of the electric and electronic devices. satisfy both CTE matching and high TC. The properties of aluminum and copper is also summarized in Table 1.3. As shown in Table 1.3, aluminum and copper have relatively high TCs than other metals. But the CTEs of aluminum and copper are unmatchable to semiconductor materials.

To solve this problem, a series new material was developed, such as graphite or carbon foam [28, 29], MMCs [30-32], ceramic matrix composites (CMS) [33], polymer matrix composites (PMS) [34] and etc. However, the graphite or carbon foam and CMCs need high fabrication costs due to high temperature of the fabrication process and the PMCs have too low melting point of matrix to apply at the high heat generation objects. While, MMCs were focused on in recently years due to following reasons: the relatively high TCs of the metals as matrix, good cost performance, high temperature resistance, and good workability. The candidate materials for the fabrication of MMCs are summarized in Table 1.4. As summarized in Table 1.4, the metals, including aluminum, have TC over 200 $W \cdot m^{-1} \cdot K^{-1}$. While, the metal, such as aluminum and copper, have unmatchable CTEs with the semiconductor materials. Thus, a series of reinforcement with outstanding TC and low CTE is chosen to fabricate MMCs. Especially, the carbon-based materials such diamond, graphene, CNT and etc. is thought to be the promising reinforcement of MMCs for the relatively have TCs and nearly zero CTEs.

Therefore, a series of MMCs were developed in recently years to meet the demand of as high as TC and matchable CTE. The MMCs for heat sink can be generally classified as carbon-based/MMCs, ceramic/MMCs and metal/MMCs. The properties of MMCs developed in recently years are summarized in Table 1.5. As summarized in Table 1.5, different volume fractions of various reinforcements were utilized to fabricate MMCs for the application of heat sink. Most CTEs of the MMCs, such as diamond/Cu , C/Cu, C/Al and SiC/Al composites, achieved the goal of matching the CTEs of the semiconductors which were approximately ranged from 4 to 7×10^{-6} K^{-1}. However, the MMCs show the wide range of TCs depending on the different composition of the materials.

Among the MMCs in Table 1.5, the diamond/Cu, diamond/Al have high TC and matchable CTE due to the extremely high TC and low CTE of the diamond. And graphene reinforced MMCs and silver matrix composite also have outstanding properties. However, the application of these MMCs is limited in the military and aerospace industry for the high price of diamond, graphene and silver. On the other hand, ceramic/MMCs, the CTEs remarkably decreased in comparison with the traditional heat sink material, such as aluminum and Cu. However, the high TC and matchable CTEs are not simultaneously achieved. But the heat sinks are usually machined to fin type and pin type, which have a complex shape to enlarge surface area to raise the efficiency of the heat exchanger. Thus, there is also another problem of ceramic/MMCs, which is poor workability of ceramics materials resulted in poor workability of whole ceramic/MMCs. While, CF/MMCs and CNT/MMCs shows excellent workability. Moreover, the CF/MMCs and CNT/MMCs show matchable CTEs to those semiconductor materials due to the nearly zero CTEs of CF and CNT reduced the high CTEs of matrix such as Al alloy or Cu.

Table 1.4 Density and thermal properties of materials as reinforcements and matrices for the fabrication of MMCs.

Material	Density [g·cm^{-3}]	CTE [×10^{-6} K^{-1}]	TC [(W·m^{-1}·K^{-1})]	Ref.
Reinforcement				
Diamond	3.5	2.3	1300~1800	[35, 36]
Graphite	2.26	-1.0	1600~2000	[37-39]
Graphene	2.26	-8.0	4840~5300	[40]
Carbon fiber (CF)	1.75~2.00	-1.45~-0.6	800~1100	[41]
Vapor grown carbon fiber (VGCF)	2	-1.0	1200	[42]
Carbon nano tube (CNT)	2	-1.0	6600	[31, 43]
Silicon carbide (SiC)	3.1~3.21	2.8~5.0	80~490	[27, 44]
Aluminum nitride (AlN)	3.26~3.3	3.3~4.5	125~250	[45]
Tungsten (W)	19.3	4.5	180	[46]
Molybdenum (Mo)	10.28	4.8	138	[11]
Matrix				
Aluminum	2.7	22.3	237	[21-23]
Copper	6.9	16.5~17	385	[21-23]
Gold	19.3	14	316	[23]
Silver	10.5	19	431	[23]
Molybdenum	10.2	5	138	[23]

Table 1.5 Thermal properties of the various MMCs.

Composite	Reinforcement	vol.%	CTE $[\times 10^{-6}\,K^{-1}]$	TC $[W\cdot m^{-1}\cdot K^{-1}]$	Ref.
Carbon-based/MMCs					
Diamond/Al	Diamond particle	60	7	365	[47]
Diamond/Cu	Diamond particle	50~70	3~12	226~742	[36]
Graphite/Al	Graphite flake	10-50	22~25	*60~200	[39]
Graphene/Cu	Graphene	5~35	~	*350-500	[48]
VGCF/Al	VGCF	18.8~39.3	23~24	175	[42]
CNT/Al	CNT	0.5~5%	-	*130~200	[49]
CNT/Ag	CNT	3~6	-	*480~550	[50]
CNT/Cu	CNT	5~10	-	*320~338	[51]
CF/Al	Long carbon fiber	30	-	*273	[52]
CNF/Cu	CNF	1~15	14~17.5	80~400	[53]
Ceramic-based/MMCs					
SiC/Al	SiC particle	55	10.8	125	[44]
SiC/Cu-Si alloy	porous SiC	48	6	110	[54]
AlN/ Si-Al	Porous α-Si_3N_4	46	6.5	107	[55]
AlN/Cu	AlN powder	40~60	7.9~14.5	39~85	[56]
Metal/MMCs					
Mo/Cu	Molybdenum layer	5~20	6.6~14.8	290-381	[11]
W/Cu	Tungsten particle	10~30	-	190~250	[46]

**in xy-plane*

1.4 Fabrication processes of MMCs

MMCs are prepared through a variety of processing techniques in recently years. Fig. 1.1 shows the various processes that have been adopted for fabrication of MMCs [11, 36, 39, 42, 44, 46-56]. The fabrication process of the MMCs is mainly divided into many routes: powder metallurgy route, melting and solidification route and other routes, such as torsion/friction welding, molecular level mixing and etc. As the application of MMCs to heat sink materials, solid-state process and liquid-state process route are usually used. These two routes are mainly introduced in following parts.

Powder metallurgy (PM), as one of solid-state process, is a popular and widely applied technique for fabrication of MMCs. The PM methods are based on the mixing of matrix powders and reinforcing materials (powders, flakes and short fibers), then further conducted on pressing and sintering. The mainly mixing method includes ball-milling, mechanical alloying and etc. The pressing is normally applied on the mixture to achieve a green part for sintering. And the sintering is usually conducted lower than the molten point of matrix to achieve the combination of matrix powders by the atomic diffusion. Especially, with the application of new equipment, the steps of pressing and sintering can be simultaneously conducted on, such as spark plasma sintering (SPS) method and hot-pressing method. The method described above, on account of its simplicity, and suitable for the matrix of high melting point alloys which is difficult to use for the liquid-state process by their high melting point, is applied widely for the production of MMCs. However, a high pressure to achieve high relative density of MMCs and a various of novel mixing method are also developed to achieve the homogeneous mixture of matrix power and reinforcement, such as particles composite system (PCS) [51] and molecular level mixing [53]. Thus, PM method is limited to fabricate MMCs with low volume fraction of reinforcement. and is also limited by high equipment cost which is caused by high pressure. Also, the SPS method and hot-pressing method can be directly utilized as sandwich processing to fabricate multi-layers MMCs using layer materials, such as W-Cu composite which is no need of mixing.

As to the liquid-state process, which is a promising fabrication process for the MMCs. For low-melting-point metals such as aluminum, the liquid-state process is a viable route. The liquid-state process of fabrication MMCs for heat sink mainly include two types: casting and metal infiltration. As other fabrication processes are not suitable to fabricate MMCs for heat sink, such as melt spinning and laser deposition, which are not introduced in this work. As to the casting method, the stirring casting is one of the most widely used method for the simple fabrication process. The stirring casting method is a method via blending of reinforcing elements in molten alloy matrix to produced MMCs reinforced by dispersion particles and short fibers. However, the aggregation of reinforcement is easily caused in the stirring process, which results the low ductility of the final product. While, metal infiltration method utilizes the molten metal infiltrate into a porous preform and obtain the final product by solidification. Generally, the raw materials of preforms, such as diamond, CF and SiC, have a bad wettability with the molten metal. Therefore, a high infiltrating pressure are required to the infiltration method with unpretreated preform. Same as mentioned above, the high infiltration pressure also caused a high equipment and die cost. Moreover, a high pressure also may damage the structure of preform. In this case, the infiltration method is limited in the application of MMCs with relatively simple shapes. Thus, LPI method is focused on in recently years. To decrease the infiltration pressure, a various of pretreatment is utilized. For example, the TiC plating on diamond were reported to improve the wettability of diamond and aluminum [47]. Thus, the application of LPI method makes possible the production of more complex MMCs.

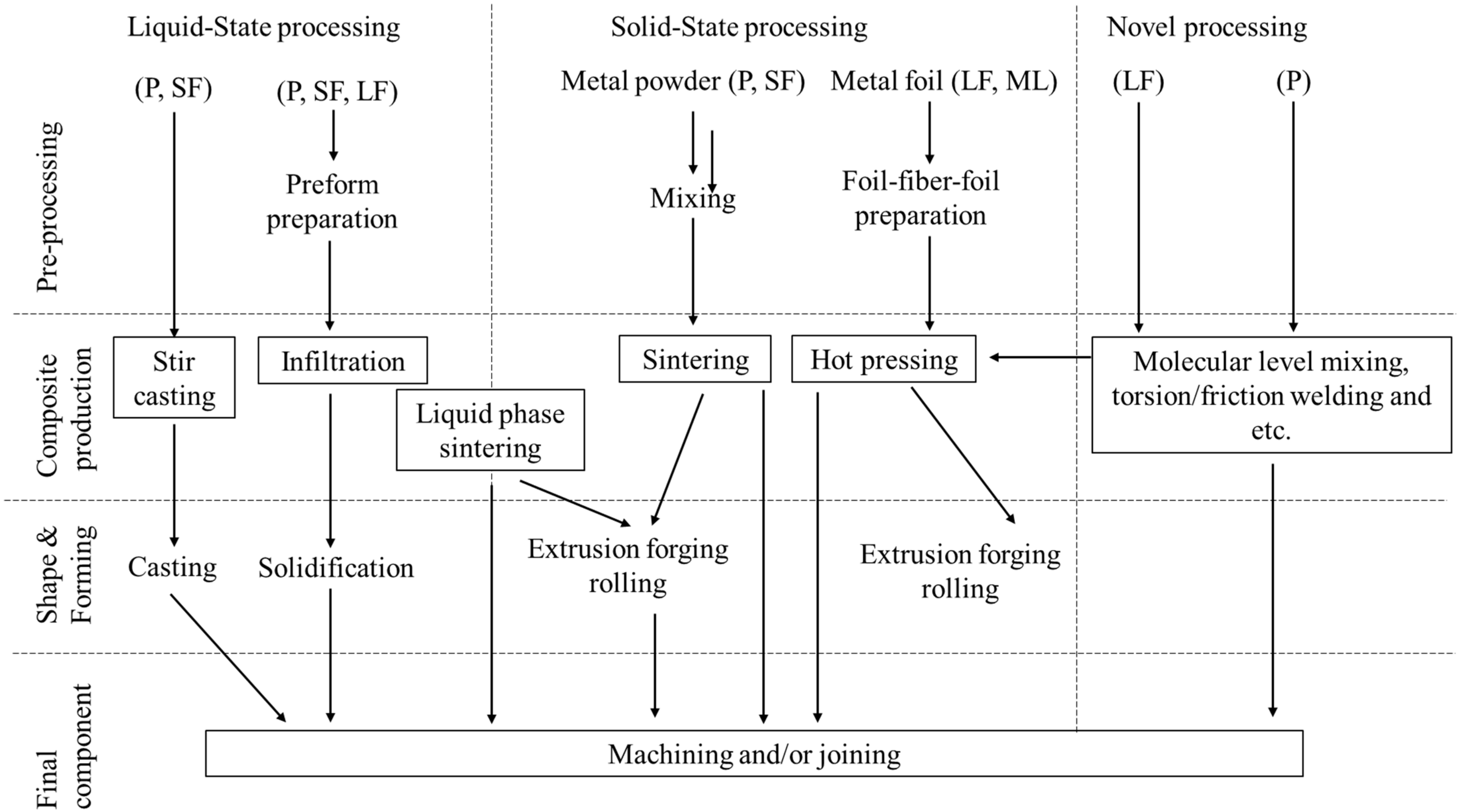

P: particle/MMCs, SF: short fiber/MMCs, SF: long fiber/MMCs and ML: multi-layer/MMCs

Fig. 1.1 Various processes of fabrication of MMCs.

1.5 Problems of previous studies and objective of this study

As summarized in Table 1.5, various ceramics and carbon-based material are utilized in fabrication of the MMCs for application of heat sink in recently years. And aluminum and copper are the mainly matrix of MMCs for heat sink for their outstanding TC comparing and acceptable price. However, there are still some problems with MMCs for heat sink materials. The problems are summarized as following. Firstly, for the commercialization of MMCs for heat sink, the acceptable cost of their fabrication process and outstanding thermal properties should be simultaneously achieved. Even the diamond reinforced MMCs show the best TC and matchable CTE, the high price of diamond limited the application of this kind of MMCs. Secondly, heat sinks are usually machined to fan type or pin type to enlarge the surface for high effective of thermal diffusion. Therefore, the diamond and ceramics reinforced MMCs have the problem which is bad workability. Besides, the graphite, graphene and carbon fiber have an anisotropy. With condition of these reinforcement are arrayed in same direction, the MMCs show an outstanding TC and matchable CTE in xy-plane of the graphite, graphene or along the carbon fiber direction. To solve this problem, a company name lake wood CO [57] in USA developed a heat sink with one-direction arrayed CF and machined to the mountain shape , and the longitudinal cross-section of this MMCs is shown in Fig. 1.2. By this method, the problem is solved, but the processing cost is increased. Besides, the multilayer MMCs also have the anisotropy. Thus, the MMCs having the anisotropy are suitable to the packing material and the sheet plane rather than the heat sink. As to the matrix of MMCs, aluminum and copper are most attractive metals for their relatively high TCs and acceptable prices. But there is a trend of light weight of the heat sink of automobile, portable electronic devices [2, 58]. Thus, the aluminum is a more potential matrix than the copper.

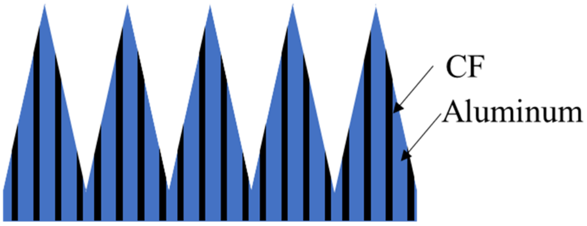

Fig. 1.2 The longitudinal cross-section of one-direction arrayed CF/Al composite with mountain shape.

As mentioned above, the PM method the and high pressure infiltration method both utilize a pressure to fabricate MMCs. This factor results that MMCs with a complex shape is difficult to be fabricated by the PM method and the high pressure infiltration method. As well, the high pressure in the fabrication processing result a high equipment cost. While, the using of LPI method to fabricate MMCs can solve these problems by a low pressure which ranges 0~1 MPa. Thus, the LPI method [44, 52, 55, 59, 60] is a suitable method to fabricate MMCs for the application heat sink with complex shape and low cost.

Besides, the balance between properties and price of the reinforcement material should concerned as another key factor to MMCs for heat sink. As the VGCF [42, 61, 62] and the CNT [31, 50, 51, 63-65] have the outstanding thermal properties and low price, the isotropic VGCF/Al composites and CNT/Al which were fabricated by LPI method were developed in this study. And their microstructure and thermal properties were investigated in this study. Moreover, the interfaces between reinforcement and aluminum matrix of these composites were also discussed.

Mover, as introduced above, the MMCs with high TC are also utilized as electric packing material. As the direction of heat transform in electronic component is from semiconductor to electric packing material, then to the heat sink. Thus, the electric packings of semiconductor have a small size and simple shape. Thus, graphene reinforced aluminum matrix (Graphene/Al) composites fabricated by SPS method were also developed in this thesis.

1.6 Outline of this thesis

In the Chapter 1 of this thesis, the trend and development method of MMCs for the application of heat sink are reviewed. The required properties of MMCs and the problems of the development of MMCs were also discussed. To meet the requirement and solve the problems, a various VGCF/Al composites and CNT/Al composites which are fabricated by LPI method for heat sink is proposed as mentioned in above of this thesis.

As the preform is a key factor to the properties of MMCs which are fabricated by LPI method, the development of the porous VGCF/MP preform is introduced in Chapter 2. In this chapter, the microstructure, the porosity and compressive properties of porous VGCF/MP are discussed.

In Chapter 3, the fabrication of the VGCF/MP/Al composites by LPI method is presented. Especially, the carbonization and the electroless nickel plating were carried on the porous VGCF/MP to improve the TC and wettability between porous VGCF/Al and aluminum matrix, respectively. Also, the mutual interfaces of porous VGCF/Al and aluminum matrix, and the TC of the VGCF/MP/Al composites are studied.

As CNTs easily aggerate in composites with high volume fraction of CNTs. Therefore, a novel reinforcement which is called CNT block, which is no need of dispersion, were utilized to fabrication of the CNT block/Al composites with by LPI method. This part is presented in Chapter 4. The electroless copper plating were curried on the CNT block. And the copper plating was utilized as binder and to improve the wettability between CNT block and aluminum matrix. The interfaces of CNT block/Al, and the TC of the CNT block/Al composites were studied.

The graphene has outstanding thermal property and ease of machining. Therefore, the Graphene/Al composites were presented in Chapter 5. These composites were fabricated by SPS method for the simple fabrication process. The microstructure of Graphene/Al composites, and their TC were studied.

As the last past part, the results from above mentioned studies are summarized in Chapter 6.

Reference

[1] S. Peterson, USA, Available at. https://medium.com/artis-ventures/omicia-moores-law-the-coming-genomics-revolution-2cd31c8e5cd0 (Accessed 20.05.16).

[2] S. Mallik, N. Ekere, C. Best and R. Bhatti: Appl. Therm. Eng. **31** (2011) 355-362.

[3] P. K. Schelling, L. Shi and K. E. Goodson: Mater. Today. **8** (2005) 30-35.

[4] IRAP Inc., USA, Available at. http://www.innoresearch.net/report_summary.aspx?id=91&pg=206&rcd=ET-123&pd=12/13/2014 (Accessed 20.05.16).

[5] Panasonic Corp., Japan, Available at. https://industrial.panasonic.com/ww/products/thermal-solutions (Accessed 20.05.16).

[6] Advanced Cooling Technologies Inc., USA, Available at. https://www.1-act.com/electronics-cooling/#section-1 (Accessed 20.05.16).

[7] Siemens, Germany, Available at. https://new.siemens.com/global/en/company/about.html (Accessed 20.05.16).

[8] Koolkwic, Available at. https://www.koolkwic.com/advanced-solid-state-lithium-battery-thermal-management/).

[9] Norma Group, Germany, Available at. https://www.normagroup.com/corp/en/norma-group-to-develop-thermal-management-systems-for-electric-vehicles-of-chinese-car-manufacturer_/ (Accessed 20.05.16).

[10] Ice Qube Inc., USA, Available at. https://www.iceqube.com/air-conditioners/qube-series-mm/ (Accessed 20.05.16).

[11] FJ Composite Co. Ltd., Japan, Available at. https://www.fj-composite.com/en/products/heat-sink.html (Accessed 20.05.16).

[12] Denka Cop. Ltd., Japan, Available at. https://www.denka.co.jp/product/detail_00045/ (Accessed 20.05.16).

[13] A.L.M.T. Corp., Japan, Available at. https://www.allied-material.co.jp/research-development/heatspreader.html (Accessed 20.05.16).

[14] JFE Precision Co., Japan, Available at. http://www.jfe-seimitsu.co.jp/pm/material-product/cr-cu.html (Accessed 20.5.20).

[15] L. Japan Fine Ceramics CO., Available at. https://www.japan-fc.co.jp/).

[16] Edgetech Industries LLC, USA, Available at. https://www.edge-techind.com/Products/Refractory-Metals/Tungsten/Tungsten-Composites/Heat-Sink-102-1.html (Accessed 20.05.16).

[17] S-Bond Technologies, USA, Available at. https://www.s-bond.com/solutions-and-service/s-bond-joined-components/thermal-management-devices/ (Accessed 20.05.16).

[18] Material innovations Inc., USA, Available at. http://www.matinnovations.com/index_files/Heatsinks.html (Accessed 20.05.16).

[19] CPS Technologies Corp., USA, Available at. https://www.alsic.com/ (Accessed 20.05.16).

[20] M. A. Afromowitz: J. Appl. Phys. **44** (1973) 1292-1294.

[21] S. Jin: JOM. **50** (1998) 46.

[22] J. Barcena, J. Maudes, M. Vellvehi, X. Jorda, I. Obieta, C. Guraya, L. Bilbao, C. Jimenez, C. Merveille and J. Coleto: Acta Astronaut. **62** (2008) 422-430.

[23] C. H. Stoessel, J. C. Withers, C. Pan, D. Wallace and R. O. Loutfy: Surf. Coat. Technol. **76-77** (1995) 640-644.

[24] ioffe, Russia, Available at. http://www.ioffe.ru/SVA/NSM/Semicond/Ge/thermal.html (Accessed 20.5.20).

[25] I. Kudman and E. Steigmeier: Phys. Rev. **133** (1964) A1665.

[26] C. Zweben: Journal of the Minerals, Metals and Materials Society. **50** (1998) 47-51.

[27] M. E. Levinshtein, S. L. Rumyantsev and M. S. Shur: Properties of Advanced Semiconductor Materials: GaN, AIN, InN, BN, SiC, SiGe, (John Wiley & Sons, 2001).

[28] N. C. Gallego and J. W. Klett: Carbon. **41** (2003) 1461-1466.

[29] A. Kabadi, G. Brady, F. Deweese and H. Hampton, Google Patents, 2005.

[30] K. Shirvanimoghaddam, S. U. Hamim, M. K. Akbari, S. M. Fakhrhoseini, H. Khayyam, A. H. Pakseresht, E. Ghasali, M. Zabet, K. S. Munir and S. Jia: Composites Part A. **92** (2017) 70-96.

[31] S. Bakshi, D. Lahiri and A. Agarwal: Int. Mater. Rev. **55** (2010) 41-64.

[32] C. Zweben: Journal of the Minerals, Metals and Materials Society. **44** (1992) 15-23.

[33] A. Sommers, Q. Wang, X. Han, C. T'Joen, Y. Park and A. Jacobi: Appl. Therm. Eng. **30** (2010) 1277-1291.

[34] X. Chen, Y. Su, D. Reay and S. Riffat: Renew. Sust. Energ. Rev. **60** (2016) 1367-1386.

[35] K. Mizuuchi, K. Inoue, Y. Agari, Y. Morisada, M. Sugioka, M. Tanaka, T. Takeuchi, J.-i. Tani, M. Kawahara and Y. Makino: Composites Part B. **42** (2011) 825-831.

[36] K. Yoshida and H. Morigami: Microelectron. Reliab. **44** (2004) 303-308.

[37] R. Prieto, J. Molina, J. Narciso and E. Louis: Scripta Mater. **59** (2008) 11-14.

[38] C. Zhou, G. Ji, Z. Chen, M. Wang, A. Addad, D. Schryvers and H. Wang: Mater. Des. **63** (2014) 719-728.

[39] H. Kurita, T. Miyazaki, A. Kawasaki, Y. Lu and J.-F. Silvain: Composites Part A. **73** (2015) 125-131.

[40] S. C. Tjong: Mat. Sci. Eng. R. **74** (2013) 281-350.

[41] E. Mayhew and V. Prakash: J. Appl. Phys. **115** (2014) 174306.

[42] Z.-F. Xu, Y.-B. Choi, K. Matsugi, D.-C. Li and G. Sasaki: Mater. Trans. **51** (2010) 510-515.

[43] J. Che, T. Cagin and W. A. Goddard III: Nanotechnology. **11** (2000) 65.

[44] S. Ren, X. He, X. Qu and Y. Li: J. Alloys Compd. **455** (2008) 424-431.

[45] B. Dun, X. Jia, C. Jia and K. Chu: Rare Metals. **30** (2011) 189-194.

[46] Y. Do Kim, N. L. Oh, S.-T. Oh and I.-H. Moon: Mater. Lett. **51** (2001) 420-424.

[47] H. Feng, J. Yu and W. Tan: Mater. Chem. Phys. **124** (2010) 851-855.

[48] K. Chu, X.-h. Wang, F. Wang, Y.-b. Li, D.-j. Huang, H. Liu, W.-l. Ma, F.-x. Liu and H. Zhang: Carbon. **127** (2018) 102-112.

[49] J. Wu, H. Zhang, Y. Zhang and X. Wang: Mater. Des. **41** (2012) 344-348.

[50] P. Hemant and V. Sharma: T. Nonferr. Metal. Soc. **25** (2015) 154-161.

[51] K. Chu, Q. Wu, C. Jia, X. Liang, J. Nie, W. Tian, G. Gai and H. Guo: Compos. Sci. Technol. **70** (2010) 298-304.

[52] M. Lee, Y. Choi, K. Sugio, K. Matsugi and G. Sasaki: Compos. Sci. Technol. **97** (2014) 1-5.

[53] J.-F. Silvain, C. Vincent, J.-M. Heintz and N. Chandra: Compos. Sci. Technol. **69** (2009) 2474-2484.

[54] K. Zhang, Z. Shi, H. Xia, K. Wang, G. Liu, G. Qiao and J. Yang: Ceram. Int. **42** (2016) 996-1001.

[55] A. Kalemtas, G. Topates, O. Bahadir, K. Pinar and H. Mandal: T. Nonferr. Metal. Soc. **23** (2013) 1304-1313.

[56] K.-M. Lee, D.-K. Oh, W.-S. Choi, T. Weissgärber and B. Kieback: J. Alloys Compd. **434** (2007) 375-377.

[57] B. L. Whatley, U.S. Patents, 2005.

[58] I. Sauciuc, R. Prasher, J.-Y. Chang, H. Erturk, G. Chrysler, C.-P. Chiu and R. Mahajan.

[59] Y. B. Choi, K. Matsugi, G. Sasaki and S. Kondoh: Mater. Trans. **49** (2008) 390-392.

[60] X.-H. Han, Q. Wang, Y.-G. Park, C. T'joen, A. Sommers and A. Jacobi: Heat Transfer Eng. **33** (2012) 991-1009.

[61] O. Lee, M. Lee, Y. Choi, K. Sugio, K. Matsugi and G. Sasaki: Mater. Trans. **55** (2014) 827-830.

[62] M. Endo, Y. Kim, T. Hayashi, K. Nishimura, T. Matusita, K. Miyashita and M. Dresselhaus: Carbon. **39** (2001) 1287-1297.

[63] E. T. Thostenson, Z. Ren and T.-W. Chou: Compos. Sci. Technol. **61** (2001) 1899-1912.

[64] W. Chen, J. Tu, L. Wang, H. Gan, Z. Xu and X. Zhang: Carbon. **41** (2003) 215-222.

[65] H. H. Kim, J. S. S. Babu and C. G. Kang: Mater. Sci. Eng., A. **573** (2013) 92-99.

Chapter 2

Development and characterization of porous VGCF/MP by spacer method

Contents

Contents 27

2.1 Introduction 28

2.2 Manufacturing process of porous VGCF/MP and characterization 30

- *2.2.1 Raw material* 30
- *2.2.2 Manufacturing process and carbonization of porous VGCF/MP* 32
- *2.2.3 Observation of microstructure of porous VGCF/MP* 35
- *2.2.4 Porosity of porous VGCF/MP* 36
- *2.2.5 Test of compressive property and TC of porous VGCF/MP* 37

2.3 Result and Discussion 40

- *2.3.1 Effect of volume fraction of NaCl Particles on Microstructure and porosity of porous VGCF/MP* 40
- *2.3.2 Effect of carbonization on porous VGCF/MP* 45
- *2.3.3 Effect of Mixing method on closed pores of porous VGCF/MP* 48
- *2.3.4 Compressive strength of porous VGCF/MP* 50
- *2.3.5 TC of porous VGCF/MP* 53

2.4 Summary 55

Reference 56

2.1 Introduction

Materials are the basis for improving human production and living standards. They provide milestones in human progress. Humans have been accessing and using materials for several thousand years. As the rapid development of modern science and technology, there are harsher special requirements for materials. Especially, with the development of electric and electronic devices in daily life and industrial production, the materials for the heat sink, which have a high thermal conductivity (TC) and a coefficient of thermal expansion (CTE) matching to the heat generation components, are required [1, 2]. But the conventional materials for heat sink, such as aluminum and copper, cannot simultaneously meet both of them. Therefore, the MMCs fabricated by low pressure infiltration (LPI) method are focused in recently years [3-7]. By this method, a preheated porous material is utilized as the preform and following infiltrated with molten metal to fabricate the MMCs. For the reason that a low pressure is utilized in fabrication process, the advantages of this method are able to produce MMCs with a complex shape and low cost. Thus, this method is thought to be a promising method to the attribution of MMCs' commercialization.

Carbon fibers reinforced aluminum (CFs/Al) composites can offer significant gains in terms of TC and have been identified as potential candidate materials in future. The previous research utilized long carbon fibers to manufacture CFs/Al composites by LPI method [8]. The TC is improved by long carbon fibers with anisotropy. However, there was report that a pin type heat sink, which was fabricated with an anisotropic composite, decreased the efficient of thermal dispersion [9]. In contrast, short carbon fibers facilitate dispersion in matrix with random direction can achieve the isotropy of composites. For further improvement of TC, high volume fraction of CFs is also required. Therefore, it's hoping that fabricate CFs/Al composites owing high TC with isotropic by a network structure of short fibers.

The porous material as preform is a key factor which can affect the property of final fabricated MMCs. Thus, the porous material as preform are required different properties with different applications. Generally, a porous material is a material containing a large number of pores, and the pores are not defect but designed to obtain new function. There are different types of porous material, such as parallel and prismatic type [10, 11], continuous pores type [12] and discontinuous type [13], for different applications. Therefore, the porous material with continuous pores, which are the routes for infiltration of motel metal, are suitable for the fabrication of MMCs.

On the other hand, the manufacturing methods of porous material is able to be classified in three main classes: solid state method, liquid metal solidification method, and deposition method. Particularly, during the whole process of solid state method, raw material keeping in solid state through sintering or other solid state method to manufacture porous material. Moreover, the spacer method is a solid state method utilizing spacer material to form continuous pores. Thus, the size of pore and porosity of porous material can be controlled by the size of spacer material and volume fraction of spacer material, respectively.

Vapor grown carbon fiber (VGCF) as short fiber owning excellent TC and low price. And mesophase pitch was reported that can be utilized as binder to sinter VGCFs. Thus, the aim of this study is manufacturing porous VGCF/MP with various volume fraction, and investigate their microstructures, porosity, mechanical property and thermal property.

2.2 Manufacturing process of porous VGCF/MP and characterization

2.2.1 Raw materials

The raw material used to fabricate the porous VGCF/MP is as following.

a) Reinforcement

VGCF with diameter of 150nm, length of 10~20μm (Showa Denko Co., Japan) was used as reinforcement for owns excellent mechanical properties (a strength of 2.92 GPa and a tensile modulus of 240 GPa), thermal conductivity (1200$W \cdot m^{-1} \cdot K^{-1}$) and low price(10JPY/g).

b) Binder material

Mesophase pitch (MP) of diameter of 2μm (JFE Chemical Co., Japan) were used as binder material for low density (2.1 g/cm^3) and transformation into a liquid crystalline material when heated in the range 623~773K.

c) Spacer material

NaCl particles with size of 180~300 μm, were used as the spacer material to control area of pores as the reason of simple to remove.

The images of raw material are shown in Fig. 2.1.

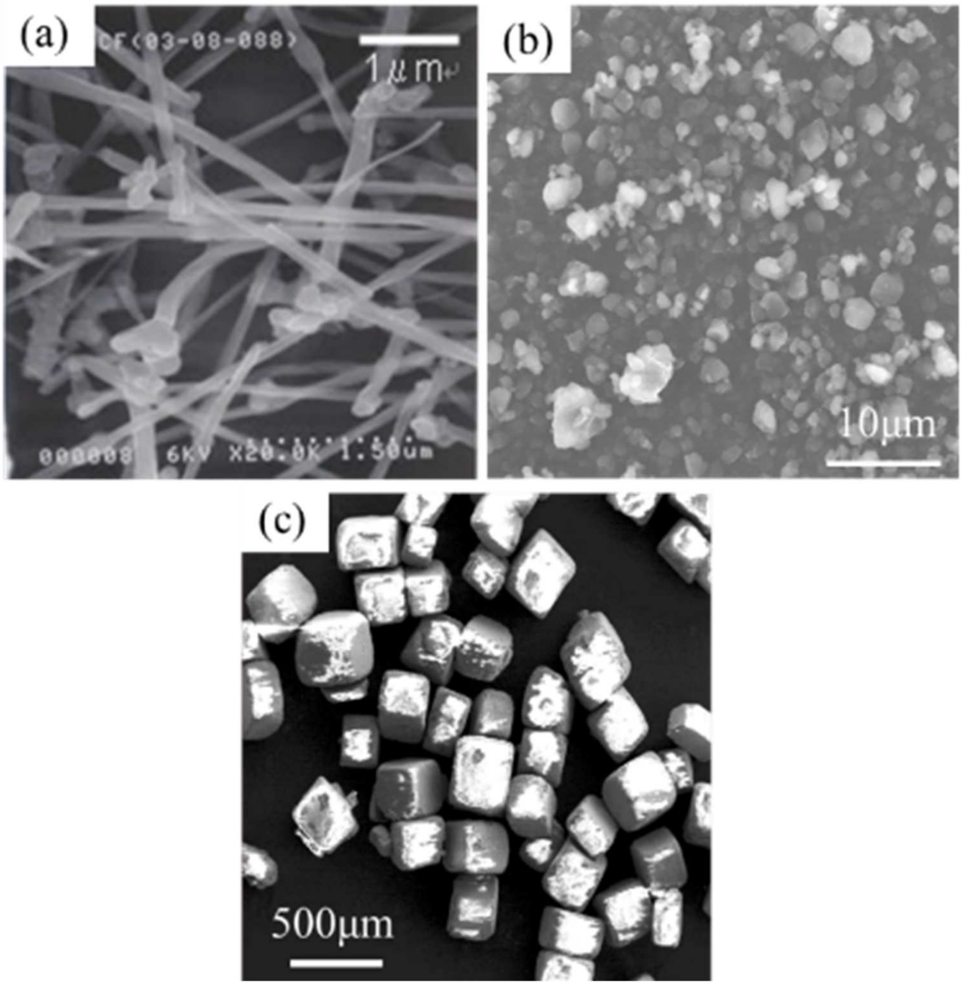

Fig. 2.1 Images of raw material: (a) VGCFs; (b) MP; and (c) NaCl particles.

2.2.2 Manufacturing process and carbonization of porous VGCF/MP

As introduced above, there are many ways to manufacture porous material. Not all are suitable to manufacture porous material. The advantage of spacer method is able to control the morphology and size of pores and form continues open pores by spacer material. In this study, spacer method was utilized to manufacture porous VGCF/MP for the further fabrication of MMCs.

Firstly, the VGCFs, MP and NaCl particles were mechanically mixed at horizontal position or tilt of 45° for 600 s using a glass rod. Secondly, mixture was put into a graphite mold and pressed at 60 MPa. The molded mixture was sintered for 5400 s in resistance furnace at atmosphere of air. For the reason that carbon fiber will react with

$$\text{Reaction above 873K:}\quad C(s) + O_2\,(g) \rightarrow CO_2(g) \qquad (2.1)$$

$$\text{Reaction below 873K:}\quad C(s) + 0.5O_2\,(g) \rightarrow CO(g) \qquad (2.2)$$

oxygen as flowing equations:

In order to prevent the reaction between carbon fiber and oxygen and ensure MP be softened, the sintering temperature was set at 823K. Then sintered compact was immersed into distilled water to dissolve NaCl at room temperature for 48h. Final sample was dried at 323K to remove distilled water. The schematic diagram of manufacturing process of porous VGCF/MP material is shown by Fig. 2.2. To investigate the effect of volume fraction VGCFs and mixing method, fabricated samples are listed as table 2.1.

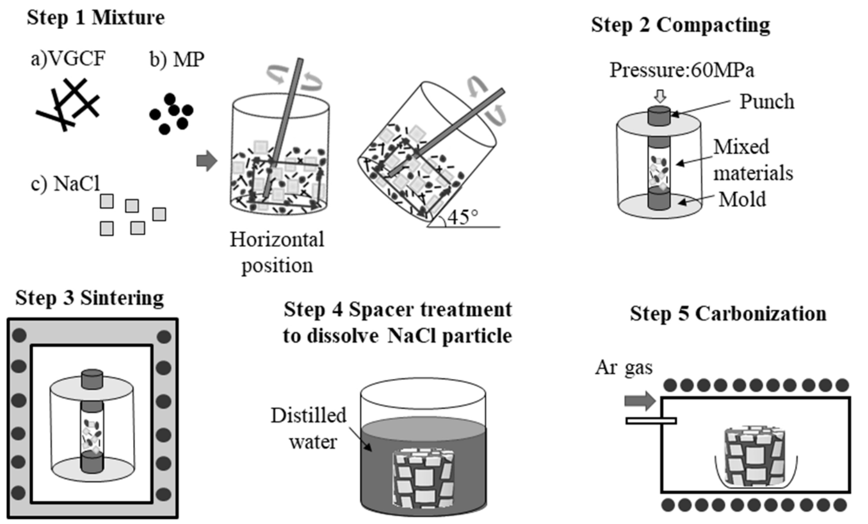

Fig. 2.2 Schematic diagram of fabrication process of porous VGCF/MP.

Table 2.1 Volume fraction of raw material and mixing method to fabricated porous VGCF/MP.

Sample	Volume fraction (vol.%)			Mixing method
	NaCl	MP	VGCFs	
1	70	7	3	Horizontal
2	80	7	3	
3	90	7	3	
4	90	7	3	Tilt of 45°

MP as amorphous has a low TC. To improve the TC of porous VGCF/MP, fabricated samples were carbonized at 1773K in Ar for 3.6 ks. In order to reduce the effect of oxygen, carbonization furnace is utilized to carry on carbonization. Fig. 2.3 is the photo of the carbonization furnace.

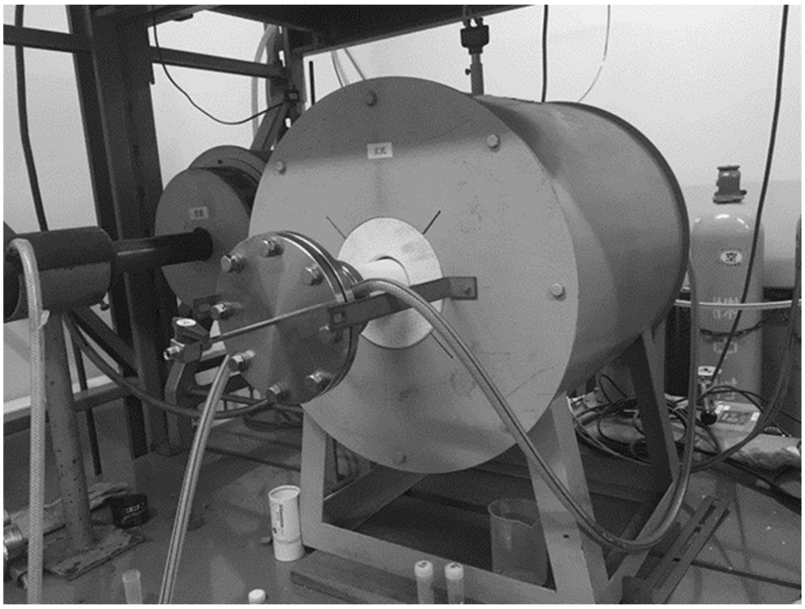

Fig. 2.3 Photo of carbonization furnace.

2.2.3 Observation of microstructure of porous VGCF/MP

A scanning electron microscope, (SEM; JEOL JXA8900; 15kV) was used for microstructure observation of raw material and the porous VGCF/MP. The lattice spacing of the as-received MP and VGCF (002) planes were investigated using X-ray diffraction (XRD; JEOL JDX-11RA, Cu-Kα, 40.0 kV 40mA). The MP was subsequently heated at 793K for 1 h under vacuum below 40 Pa to determine how heating affected MP crystallization. The (002)-plane lattice spacing of the heated MP was then investigated using XRD. A 1: 9 mixture of VGCFs and MP was then blended for 1800 s in ethanol, which was subsequently evaporated. The mixture was put into an 11-mm-diameter, 10-mm-high copper mold. The molded mixture was then heated at 793K for 1h under vacuum below 40 Pa to fabricate the porous VGCF/MP composite preform containing 35%. The structures of the VGCF surface and the interface between the VGCFs and MP were observed using a transmission electron microscopy (TEM; JEOL JEM-2010, 200 kV). The nanostructures of the VGCF surface were analyzed using an inverse fast flourier transform (IFFT) by digital micrograph software.

2.2.4 Porosity of porous VGCF/MP

Archimedes method is applied to measure the porosity of porous VGCF/MP. The Archimedes method is a method of obtaining the density of a sample by using a buoyant force of a solid in a liquid as much as the weight of a liquid having the same volume (Archimedes principle). This method is one of the most widely used density measurement methods because it is simple to measure the density of a sample with a liquid, such as the density of pure water or alcohol etc. and a balance can measure accurate mass easily. First, the sample was dried at 323k for 5 h to remove water, then measure the dry weight W_1. Next, sample was putted in a beaker. And the beaker was set in a vacuum container and filled with distilled water at room temperature. To ensure the sample was fully saturated with distilled water whose density, ρ_w, is accurately known, evacuate the vacuum container by a pump at pressure of -0.8 MPa. The water at surface of saturated sample was removed by a wetted paper, then weighed suspended the distilled water in room temperature, W_2, and again while suspended in under a balance in air, W_3. Then calculate the density by following equations:

$$\text{Apparent density (g/cm}^3\text{):}\quad \rho_a=\frac{W_1}{W_1-W_2}\times\rho_w \qquad (2.3)$$

$$\text{Bulk density (g/cm}^3\text{):}\quad \rho_b=\frac{W_1}{W_3-W_2}\times\rho_w \qquad (2.4)$$

$$\text{Open porosity (\%):}\quad P_{open}=\frac{W_3-W_1}{W_3-W_2}\times 100\% \qquad (2.5)$$

As the theoretical density of raw material is known, theoretical density, ρ_t, is able be calculated by volume fraction of each material. Then the relative density, ρ_r, total porosity, P_{total}, and closed porosity, P_{total}, is able be calculated by following equation.

$$\text{Relative density (\%):}\quad \rho_r=\frac{\rho_b}{\rho_t}\times 100\% \qquad (2.6)$$

$$\text{Total porosity (\%):}\quad P_{total}=1-\rho_t \qquad (2.7)$$

$$\text{Closed porosity (\%):}\quad P_{closed}=P_{total}-P_{open} \qquad (2.8)$$

2.2.5 Test of compressive property and TC of porous VGCF/MP

The porous VGCF/MP will endure pressure while used in low pressure infiltration. Therefore, the sufficient compressive strength is required to prevent the pressure. To investigate the compressive strength of porous VGCF/MP, compressive test was carried on at room temperature. The standard of compressive test was JIS H7902-2008. The size of compressive test sample is 10 × ø10 mm^3. Load of test was 2450 N. And cross speed was 0.5 mm/min. As for the test apparatus, a compression test jig was attached to the tensile tester. And the dislocation was collected by a digital linear gauge (OZAKI MFG.CO.LTD., D-100s), the appearance of the device is shown in Fig. 2.4.

The compressive strength (N/mm^2) and compressive strain (%) was calculated by following equations:

$$\text{Compressive strength:}\quad \sigma=\frac{F}{A(1\text{-}P)} \tag{2.9}$$

$$\text{Compressive strain:}\quad \varepsilon=\frac{h\text{-}h_1}{h_0} \tag{2.10}$$

where F is the testing force (N) A is cross area of surface (mm^2) P is total porosity, and h, h_1, and h_0 is the height (mm) at the zero deformation point of the sample in the compression stress-compression strain curve, the height of the sample corresponding to the loaded compression test force and the height of sample, respectively.

Steady state method is a method measuring the TC by giving a steady temperature gradient to the sample [14]. A schematic diagram of the thermal conductivity measuring device is shown in Fig. 2.5. In order to reduce the contact thermal resistance of the contact portion between each bar and the sample, silver grease (Arctic Silver Co., Ltd.) is applied. The thermal conductivity of copper used for bar is 386 W/m·K. The shape of the measurement sample is 10 × ø10 mm^3. In order to make it steady state, the temperature of the heating plate and cooling plate was set 30 and 20 °C, respectively. The whole was cover device with an acrylic box to prevent heat dissipation. After the

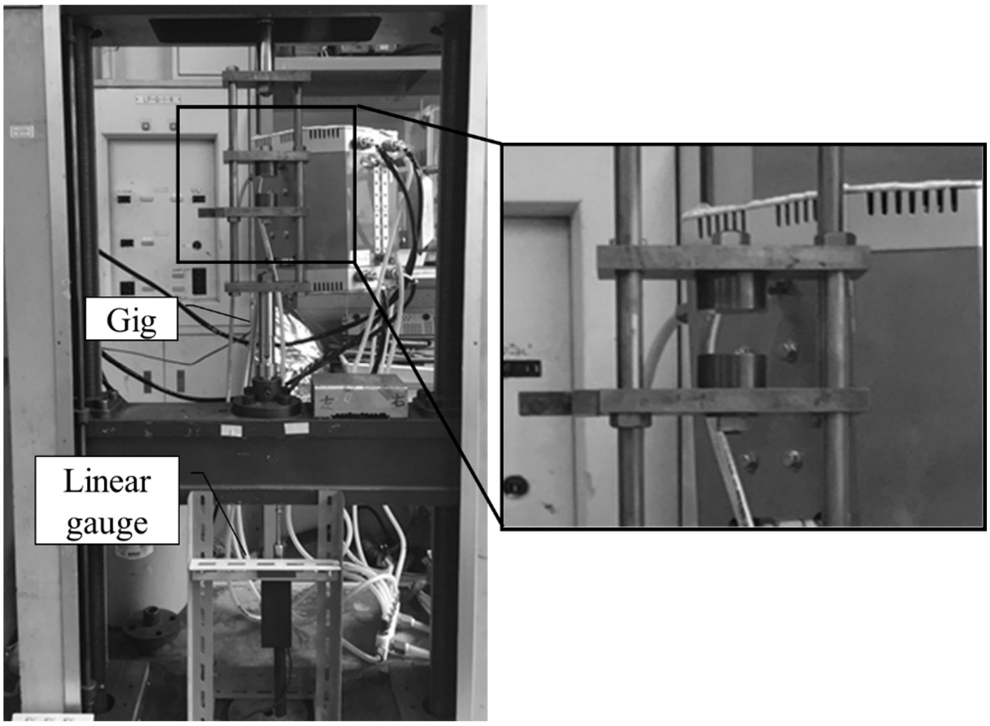

Fig. 2.4 Device of compressive strength test.

measuring device reaches a steady state, measure the temperature with a thermal couple for 1 second every 300 seconds. Assuming that the temperature gradients of hot bar, sample, and cold bar are a_h, a_s, a_c, they are expressed by the following equations.

$$a_h = \sum_{i=1}^{3}(z_i - \bar{z}_h)(T_i - \bar{T}_h) \Big/ \sum_{i=1}^{3}(z_i - \bar{z}_h)^2, \quad \bar{z}_h = \frac{1}{3}\sum_{i=1}^{3} z_i, \quad \bar{T}_h = \frac{1}{3}\sum_{i=1}^{3} T_i \tag{2.11}$$

$$a_h = \sum_{i=1}^{3}(z_i - \bar{z}_h)(T_i - \bar{T}_h) \Big/ \sum_{i=1}^{3}(z_i - \bar{z}_h)^2, \quad \bar{z}_h = \frac{1}{3}\sum_{i=1}^{3} z_i, \quad \bar{T}_h = \frac{1}{3}\sum_{i=1}^{3} T_i \tag{2.12}$$

$$a_c = \sum_{i=6}^{8}(z_i - \bar{z}_c)(T_i - \bar{T}_c) \Big/ \sum_{i=6}^{8}(z_i - \bar{z}_c)^2, \quad \bar{z}_c = \frac{1}{3}\sum_{i=6}^{8} z_i, \quad \bar{T}_c = \frac{1}{3}\sum_{i=8}^{8} T_i \tag{2.13}$$

z_i and T_i are the distance and temperature of the number i thermal couple from heating plate. Effective thermal conductivity λ_x is calculated by the following equation:

$$\lambda_x = \frac{\lambda_R (a_h + a_s)}{a_c} \tag{2.14}$$

λ_R is the thermal conductivity of the reference material. Pure copper (386 W/m·K) was used as reference material. To investigate the effect of porosity, volume fraction, samples of porous VGCF/MP with MP before carbonized were carried on with TC test. Then samples of porous VGCF/MP with MP after carbonized were carried on with TC test. In addition, samples of porous VGCF/MP with Cu were also carried on with TC test.

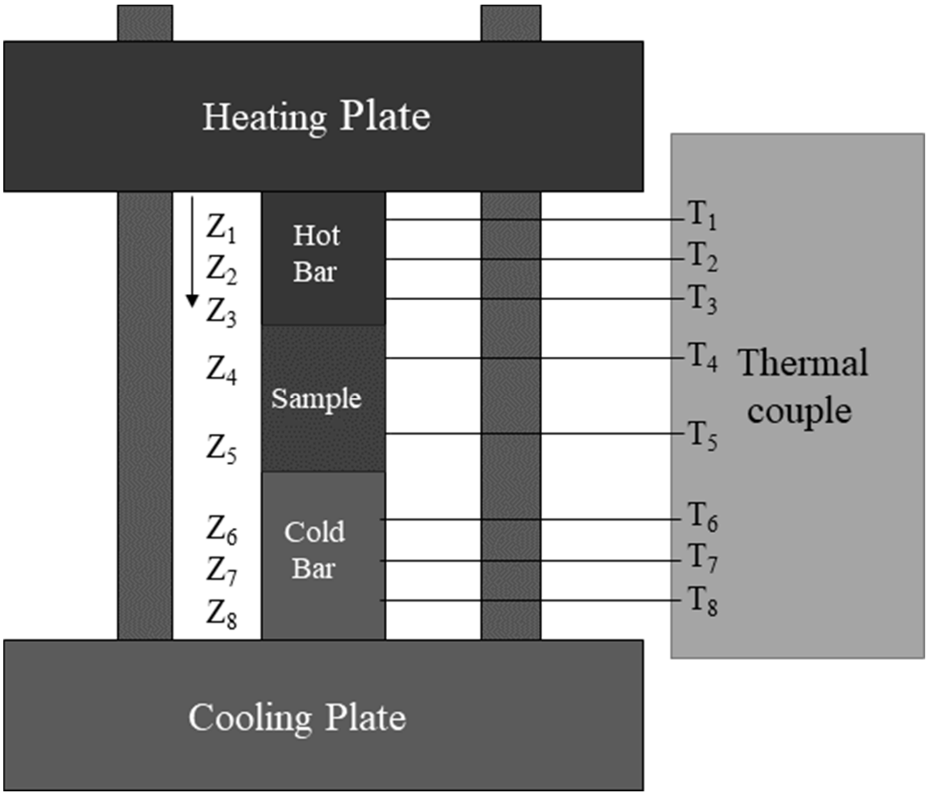

Fig. 2.5 Schematic view of a thermal conductivity measuring device.

2.3 Result and Discussion

2.3.1 Effect of volume fraction of NaCl Particles on microstructure and porosity of porous VGCF/MP

The fabricated porous VGCF/MP is shown as Fig. 2.6. It can be found that there many pores in porous VGCF/MP body. The porosity of porous VGCF/MP fabricated with different volume fractions were measured by Archimedes method and its result is shown in Fig. 2.7. It shows that the open pores and closed pores simultaneously exist in the porous VGCF/MP. Total porosity and open porosity increased with volume fraction of NaCl particles, and closed porosity decreases with volume fraction of NaCl particles. The different of P_{open} and P_{closed} is also decreasing with volume fraction of NaCl particles, which means under the condition of 70vol.%, there may undissolved NaCl particles remain in porous VGCF/MP with MP. And higher volume fraction of NaCl particles contributes to lesser remained NaCl particles by distilled water simple to reach every NaCl particles.

In order to fabricate composites by low pressure infiltration, molten metal will be infiltrated into open pores. Therefore, less closed pores are required to reduce defects.

As a result of comparing the porosities of three kinds of samples to which 70 vol.%, 80 vol.%, and 90 vol.% of NaCl particles were added, as shown in the approximate curve of Fig. 2.6, it was confirmed that there was some linearity between the porosity and the addition amount. Considering this there is a possibility that the porosity can be controlled by adjusting the addition amount of the NaCl particles, and the linear equation is obtained to be the formula (2.15).

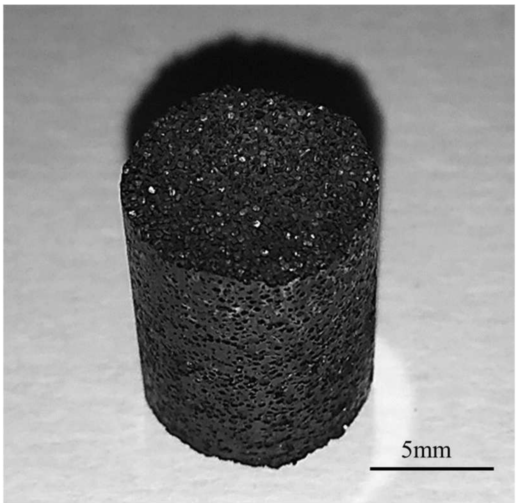

Fig. 2.6 images of porous VGCF/MP (sample No. 1).

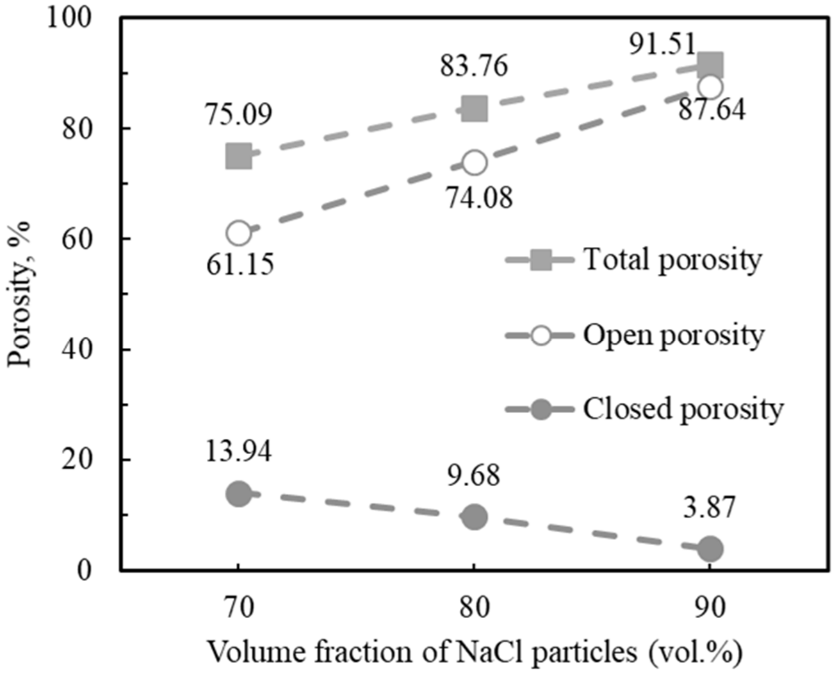

Fig. 2.7 Porosity of porous VGCF/MP with different volume fractions of NaCl particles.

Equation of total porosity and amount (vol.%) of NaCl particles:

$$P_{total} = 8.21_{\mathrm{NaCl\ volume}} + 67.00 \tag{2.15}$$

It was revealed that the added amount of NaCl particles and the porosity are proportional to each other like a straight line. In other words, it was confirmed that the method of preparing porous VGCF/MP by spacer method in this research can control the porosity easily by only adjusting the amount of NaCl particles added.

The microstructure of porous VGCF/MP fabricated with different porosity NaCl particles are shown in Fig. 2.8. From Fig. 2.8, pores have same size and shape with NaCl particles which means pores were formed by NaCl particles. In addition, the area of pores was increasing with porosity. From Fig. 2.8(d), in the condition of 75.09% total porosity, some pores were isolated which form closed pores. But in the condition of 91.51% total porosity, most of pores were connected with other pores which form continues pores. This images also proved that open porosity increases with volume fraction of NaCl particles.

Fig. 2.9 shows the SEM images of the cell wall of porous VGCF/MP. By Fig. 2.9, it can find that VGCFs are straight rather than wined with each other. And most of the MP powders are agglomerated to large bulks including VGCFs, whereas very little MP was attached to the VGCF surface. The VGCF edges were well attached at the MP as indicated by the circle in Fig. 2.9(b), and the VGCFs were randomly oriented.

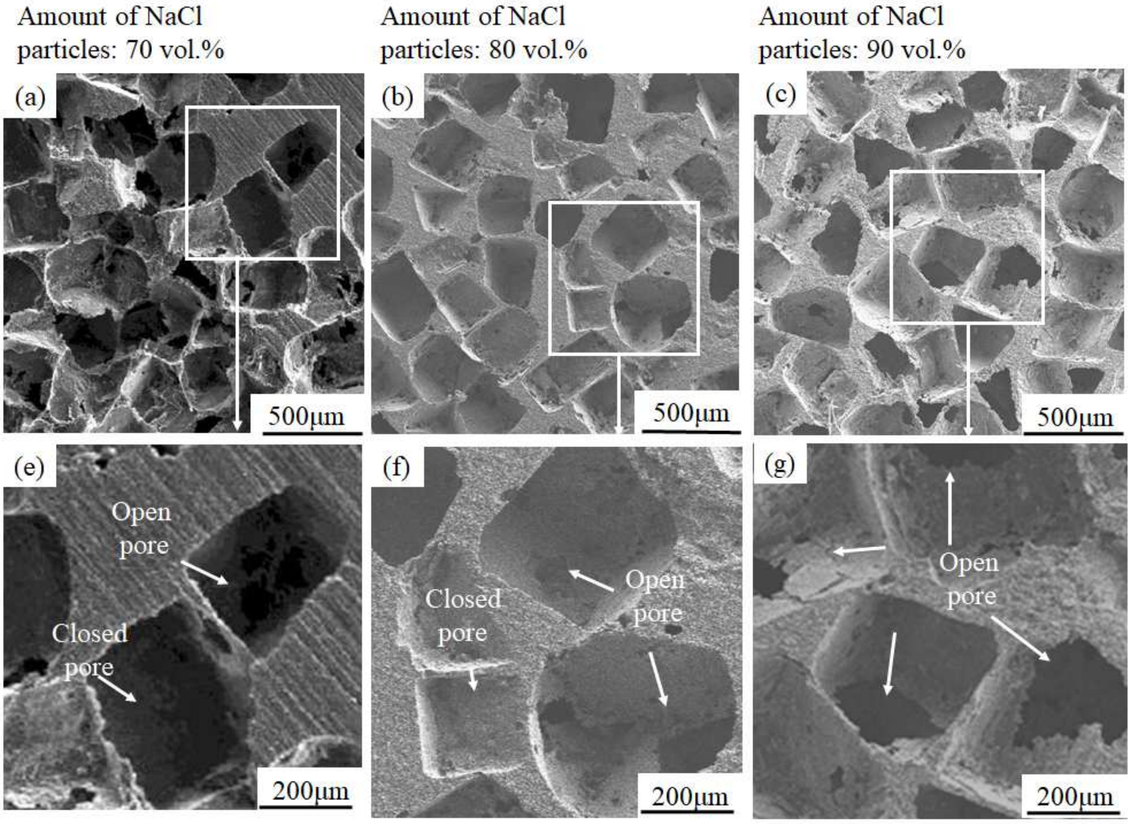

Fig. 2.8 SEM images of the porous VGCF/MP: (a), (b), and (c) porous VGCF/MP with total porosity is 75.09%, 83.76%, and 91.51%, respectively; (d), (e), and (f) higher magnification images of each porous VGCF/MP, respectively.

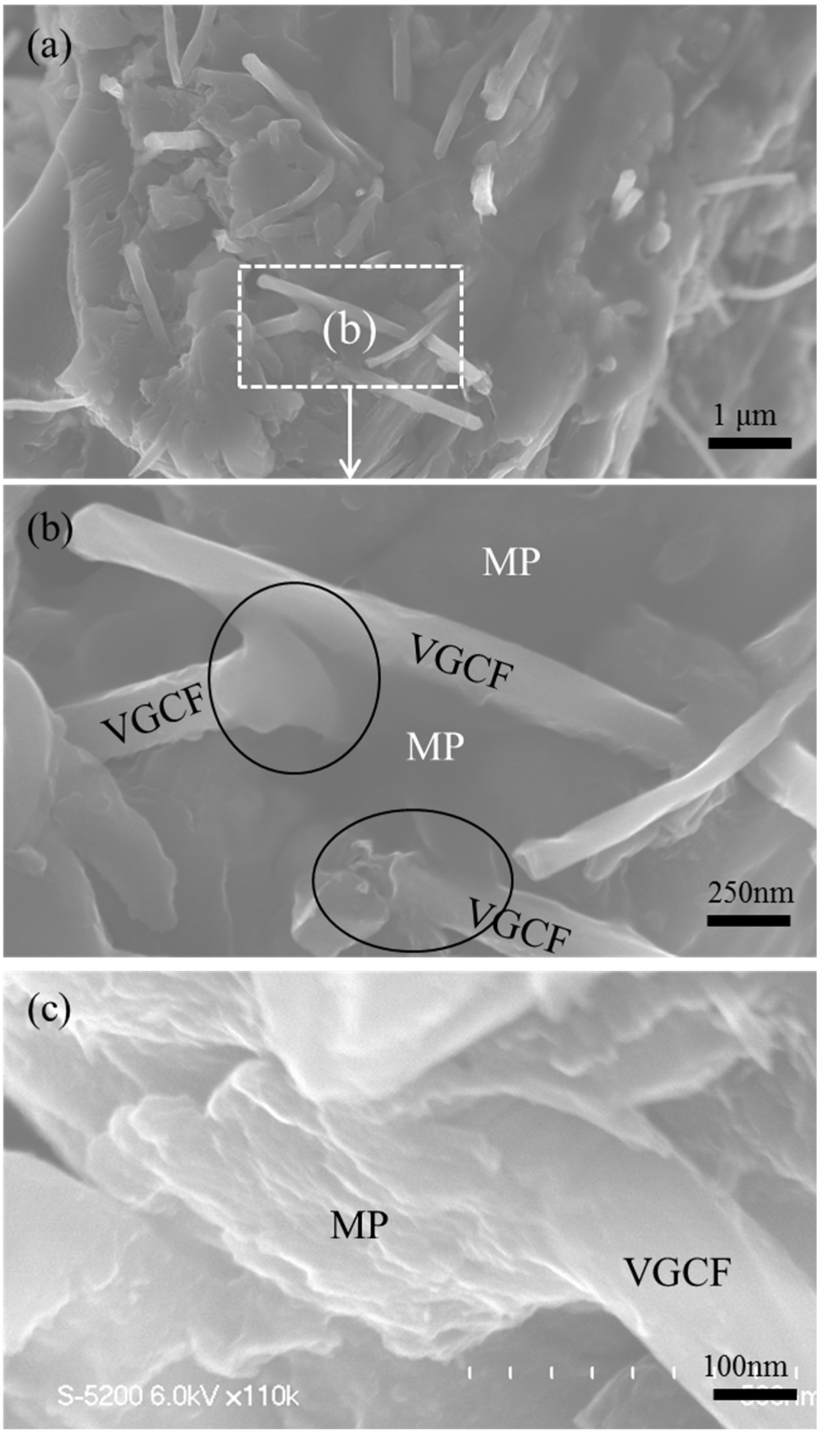

Fig. 2.9 SEM images of the cell wall of porous VGCF/MP:
(a) low magnification, (b) and (c)high magnification.

2.3.2 Effect of carbonization on porous VGCF/MP

Fig. 2.10 is TEM images of porous VGCF/MP before and after carbonization. Fig. 2.10(a) shows that the VGCFs were crosslinked by the bridging MP before carbonization. Moreover, the VGCF surfaces were covered with a thin MP layer, which formed the bridging MP. Fig. 2.10(b) shows the VGCF-MP interface before carbonization, which consisting of linear and wavy carbon structures in the porous VGCF/MP. VGCF as multiwall carbon nano fiber owns a linear carbon structure on the VGCF surface. The wavy structure showed dislocation near the VGCF-MP interface. MP is believed to bridge the VGCFs at the VGCF dislocation edges. In the Fig. 2.10(b), the interface of VGCF- MP shows not only linear but also wavy carbon structures

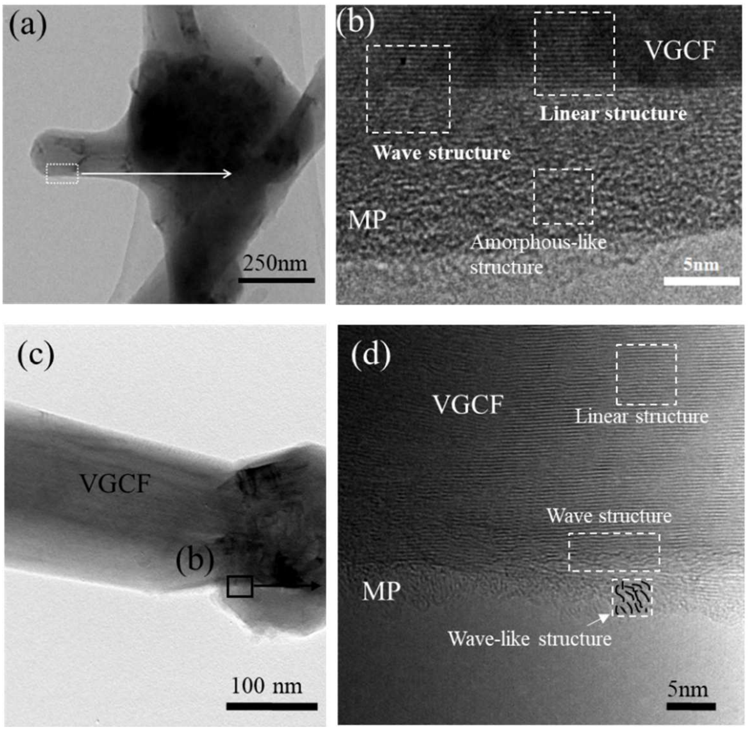

Fig. 2.10 TEM images of porous VGCF/MP: (a) before carbonization, and (c) after carbonization; (b) and (d)high magnification TME images of locations of (a) and (c), respectively.

between MP shows not only linear but also wavy carbon structures between the VGCFs and MP. Fig. 2.10(c) and 2.10(d) shows the VGCF-MP interface after carbonization. As shown in Fig. 2.10(c), after carbonization, the VGCF surfaces were also covered with a thin MP layer. And as shown in Fig. 2.10(d), the area of wave in enlarged, which indicated that the carbonization promoted the crystallization of MP [15]. As the carbonization promoted the crystallization of MP, a further analysis was conducted on with the MP of before and after carbonization. Fig. 2.11 shows the TEM images of MP before and after carbonization. Comparing Figs. 2.11(a) and 2.11(b), the structure of MP was switched from disorder structure to layer structure by carbonization. And comparing the FTT images of Figs. 2.11(a) and 2.11(b), halos became clear rings, which indicated MP were crystallized by carbonization [16]. The XRD patterns of MP before and after carbonization are shown in Fig. 2.12. And as shown in Fig. 2.12, the full width at half maximum (FWHM) of (002) were deceased from 5.280° to 1.528°. After carbonization, the peak of XRD pattern became especially sharp. It also indicated the MP had a high crystallinity due to the carbonization [17].

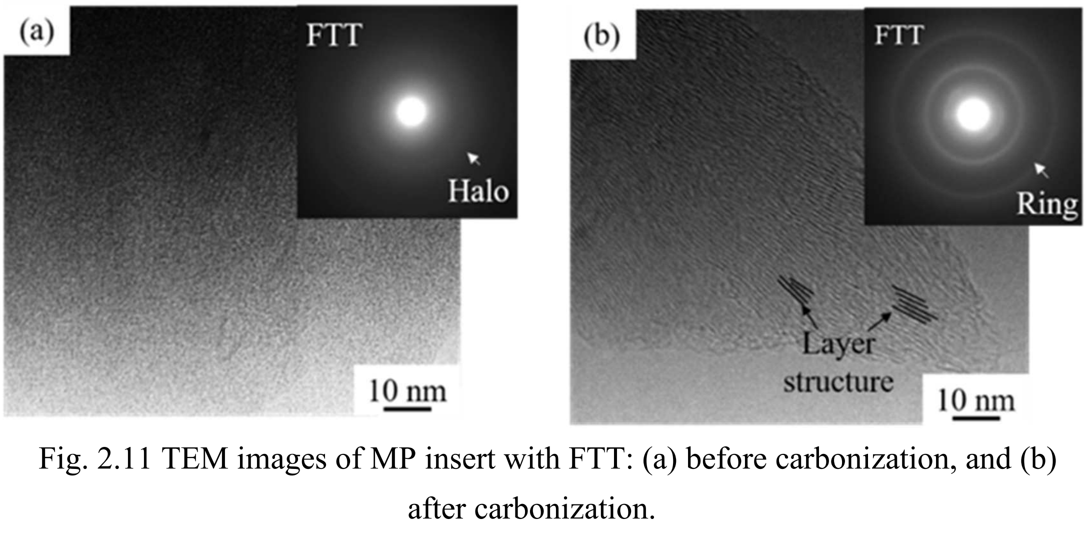

Fig. 2.11 TEM images of MP insert with FTT: (a) before carbonization, and (b) after carbonization.

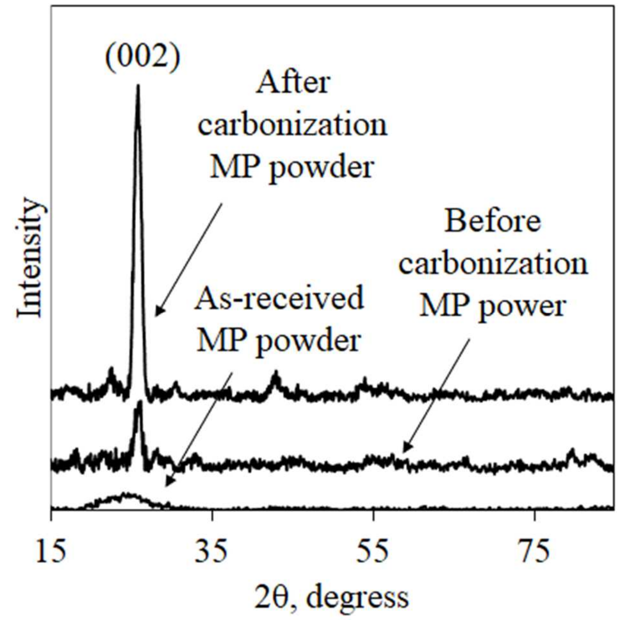

	*FWHM (°)
As-received MP powder	5.280
Before carbonization MP power	2.502
After carbonization MP powder	1.582

Fig. 2.12 XRD patterns of as-received, before and after carbonization MP, and *FWHM of (002) corresponding pattern. (*FWHM: full width at half maximum).

2.3.3 Effect of Mixing method on closed pores of porous VGCF/MP

As there were closed pores in the porous VGCF/MP, the effect of mixing method on closed pores of porous VGCF/MP (fabricated with 90 vol.% NaCl particles) was investigated. Fig. 2.13. shows the microstructures of porous VGCF/MP fabricated by different mixing method. In Fig. 2.13, as the dashed lines surrounding parts, VGCF and MP were agglomerated. As shown in images of Figs. 2.13(a), 2.13(c) and 2.13(d), the cell walls of porous VGCF/MP fabricated by horizontal mixing were showing unevenly thickness. Especially, the VGCF and MP were agglomerated with size about 200~400 μm at middle and bottom part of the preform. The reason was the insufficient motion between upper and lower layers of VGCF, MP and NaCl particles mixture by horizontal mixing. As shown in Figs. 2.13(b), 2.13(c) and (d), the VGCF and MP were agglomerated with size lower than 200 μm. In tilt mixing process, the mixture was moved up and down repeatedly by gravity and mechanical force of glass rod. Therefore, tilt mixing was selected for further steps as the evenly mixed mixture. And continuous pores were formed by connected NaCl particles. But as shown in Figs. 2.13(a) and 2.13(b), some noncontinuous macro-pores were observed. The reason was shown as in Fig. 2.13(c) and 2.13(d), some surfaces of pores were nearly parallel, which were not connected, then leaded to noncontinuous macro-pores. Thus, the tilt mixing was contributed to prevent the aggregation of VGCF and MP.

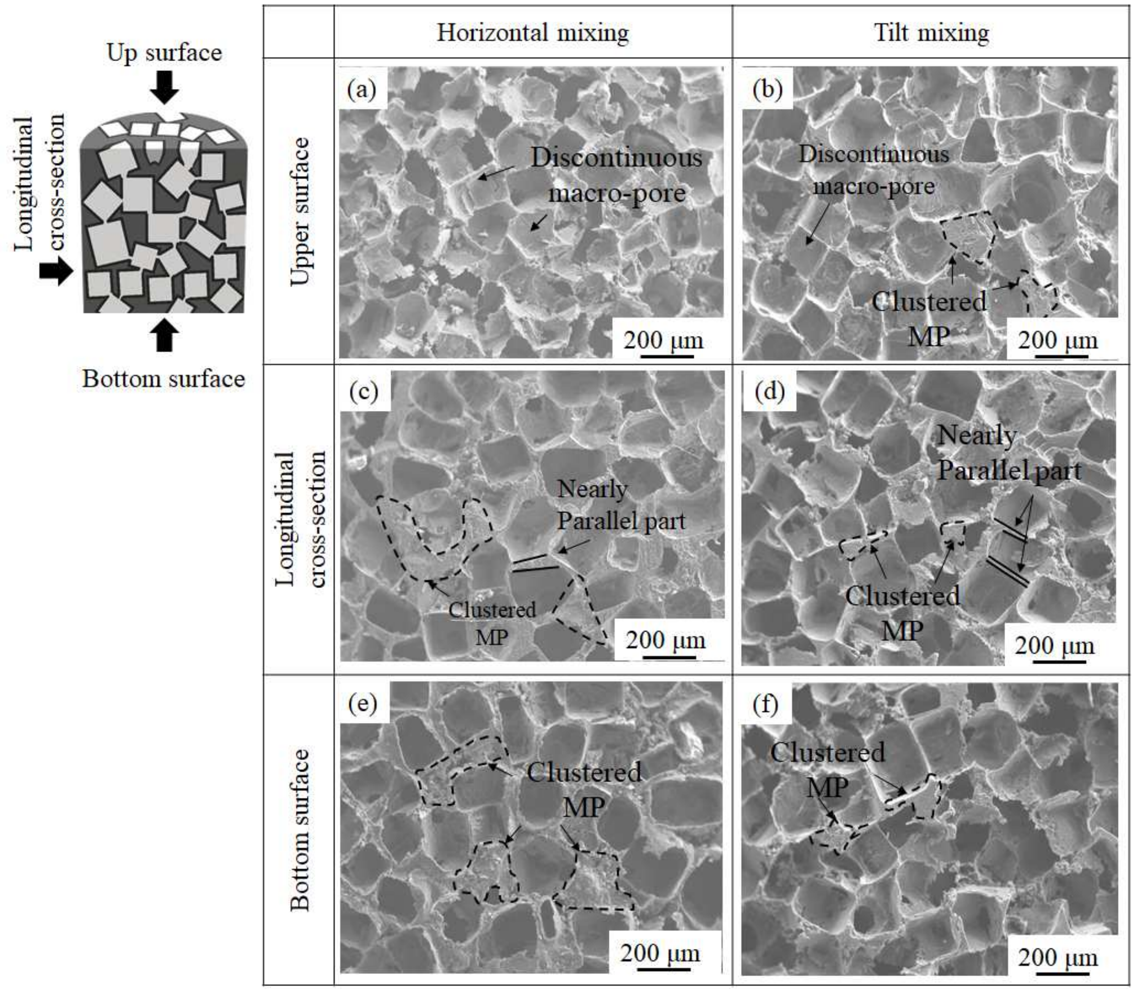

Fig. 2.13 Microstructures of porous VGCF/MP fabricated (fabricated with 90 vol.% NaCl particles) fabricated by different mixing method.

2.3.4 Compressive strength of porous VGCF/MP

Different porosity and volume fraction of porous VGCF/MP before carbonization were carried on compressive test. Fig. 2.14 shows the result of compressive test. From the Fig. 2.14, compressive test of total porosity, 91.51 % was failure for the high porosity. The yield strength of porous VGCF with 83.76 % total porosity and porous VGCF with 75.09 % total porosity are 12.07 MPa and 7.41 MPa respectively. Normally, the compressive strength is decreasing with the increasing porosity [10, 12, 18]. But when porosity is 75.09 %, the undissolved NaCl particles may lead to the stress concentrate and result in lower yield strength. And compressive test of VGCFs fractions with 30 vol.%, 50 vol.% and 70 vol.% are 4.2 MPa, 5.2 MPa and 1.12 MPa respectively. It also can be found that increasing fraction of VGCFs from 30 vol.% to 50 vol.% can improve the yield strength, but the poor compressive properties of 70 vol.% due to small amount of MP between VGCF fibers.

The schematic compressive stress-strain curves of 83.76% total porosity porous VGCF/MP is shown in Fig. 2.15 and schematic diagram cracks in each region is shown in Fig. 2.16. The curve exhibits the three regions [10, 19]: (I) elastic region characterized by elastic modulus; (II) stress plateau region characterized by a shallow slope corresponding to the plastic yielding and crack of pores frame; and (III) densification region characterized by a relatively steep slope. And the jitter of the curve is owning to the poor ductility of MP, which lead to crack occurred with low strain. Photograph of porous VGCF/MP with MP after compressive strength test is shown in Fig. 3.13. In Fig. 3.13, through cracks happened with low compressive strain.

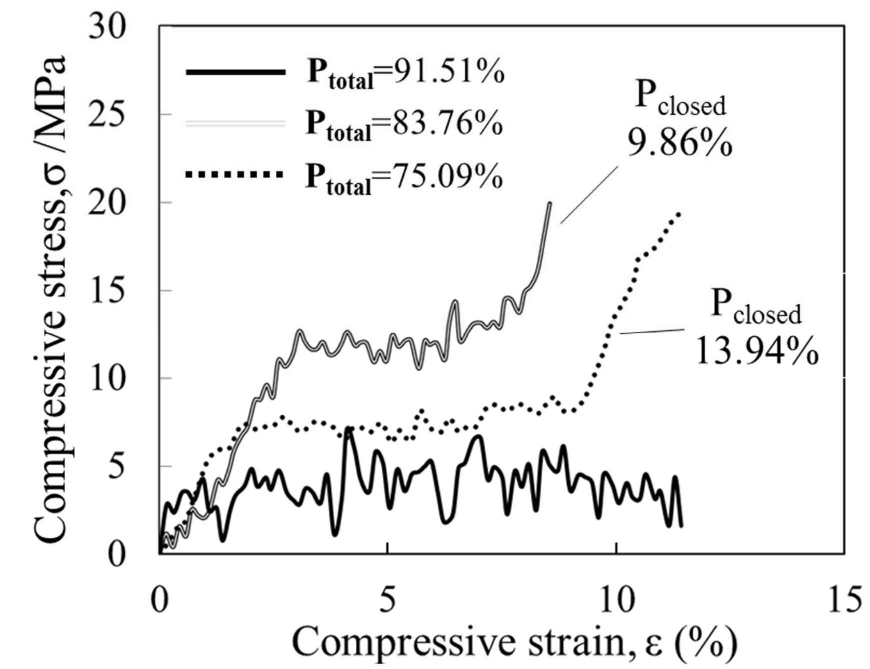

Fig. 2.14 Compressive stress–strain curve of porous VGCF/MP with different porosity and same fraction of raw materials (VGCF: MP= 3:7) before carbonization.

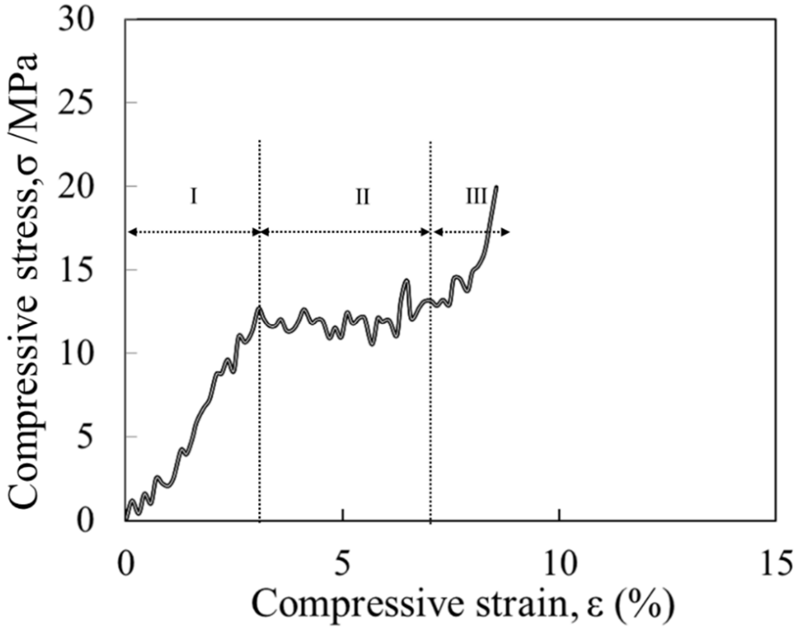

Fig. 2.15 Compressive stress-strain curves of 83.76 % total porosity porous VGCF/MP (VGCF: MP= 3:7) before carbonization.

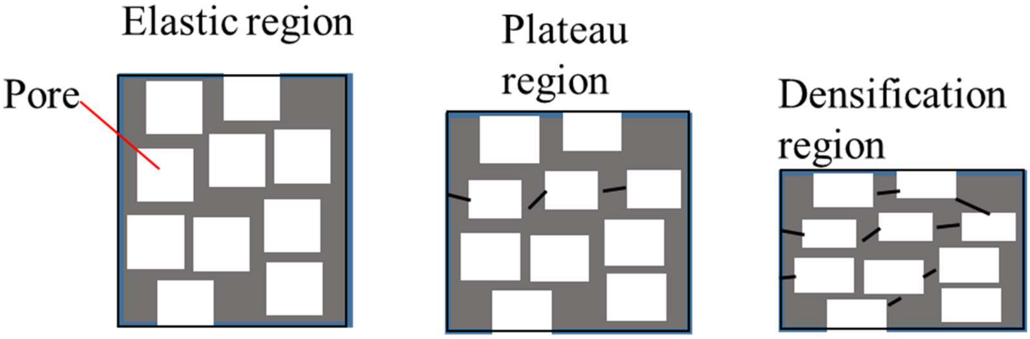

Fig. 2.16 Schematic diagram cracks in each region.

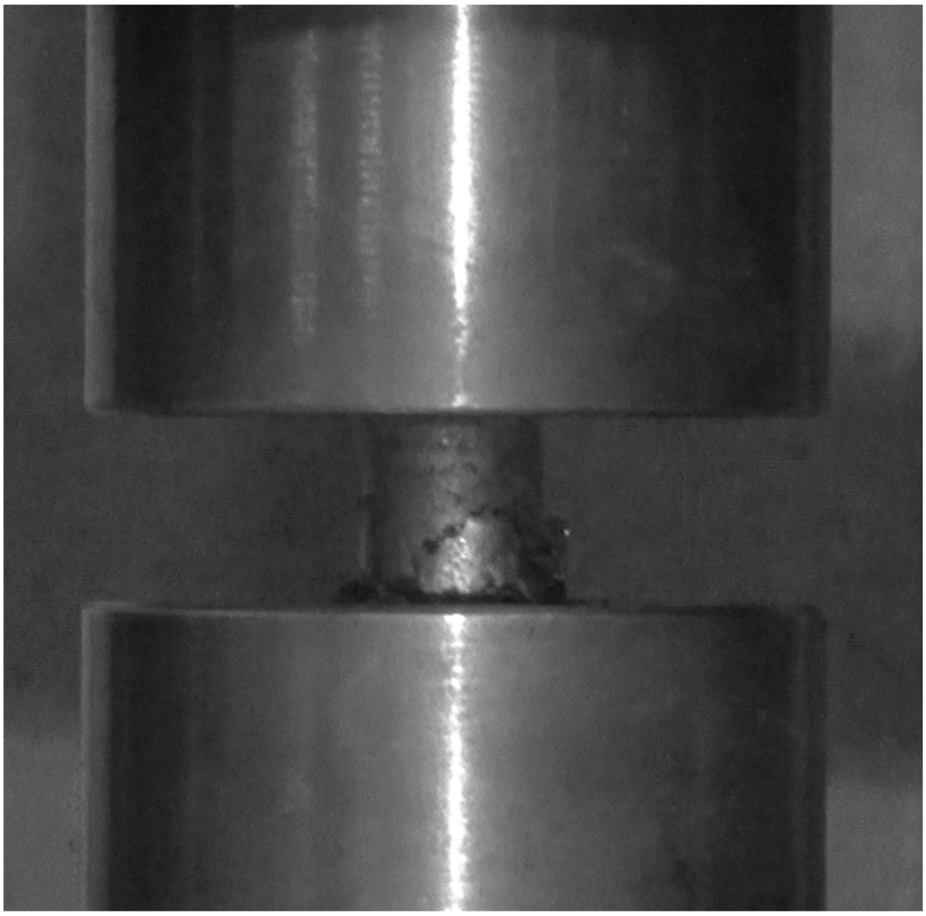

Fig. 2.17 Photograph of porous VGCF/MP after compressive strength test.

As discussed above, the first crack of porous VGCF/MP was happened at the time of first peak of compressive stress–strain curve. As to the porous VGCF/MP with porosity of 91.51 %, the first crack appeared with about 3 MPa (see Fig. 2.14). Thus, with infiltration pressure lower than 3 MPa, the porous VGCF/MP with porosity of 91.51 % is still thought can be able to be utilized for the fabrication of MMCs.

2.3.5 TC of porous VGCF/MP

TC of porous VGCF/MP before carbonization with different porosity is shown in Fig. 2.18. The lower porosity means more pathway for heat quantity to transfer, than led to the TC is decreasing with increasing porosity [20, 21]. The TC of porous VGCF/MP is higher than which of porous aluminum 6011 alloy. This result indicated that porous VGCF/MP is a promising reinforcement to fabricated composites.

To investigate the effect of carbonization on porous VGCF/MP. The TC of porous VGCF/MP before and after carbonization is shown in Fig. 2.19. As shown in Fig. 2.19, the TC were improved by carbonization for crystallization of MP [16, 17].

In total, the TC of the porous VGCF/MP with porosity of 91.51 % was lower than other samples with lower porosity. But, the TC of porous VGCF/MP in proved that can be improved by carbonization. Therefore, the porous VGCF/MP after carbonization with porosity of 91.51 % is still can be utilized to fabricate MMCs.

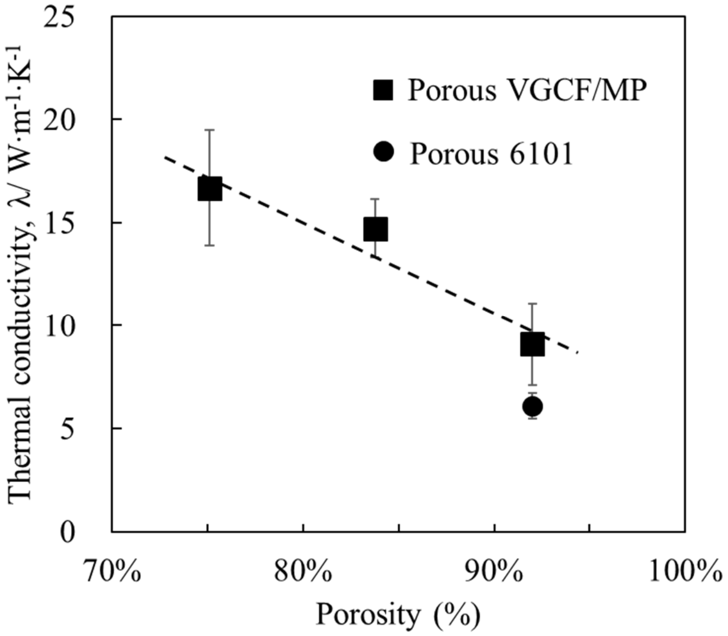

Fig. 2.18 TC of porous VGCF/MP with different porosity before carbonization and porous aluminum alloy 6011 [7].

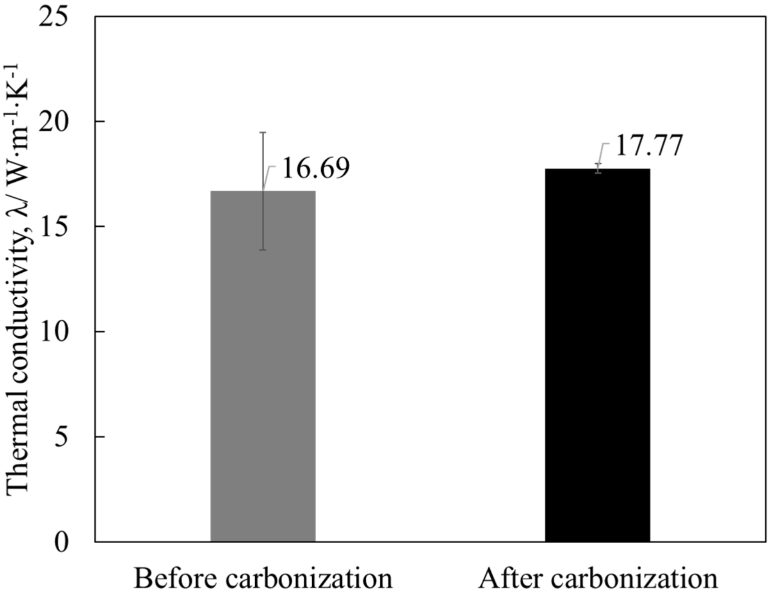

Fig. 2.19 TC of porous VGCF/MP (total porosity:75.09%, VGCF:MP=3:7) before and after carbonization.

2.4 Summary

Porous VGCF/MP were fabricated. The main conclusions are summarized as below:

(1) Pores are formed by NaCl. The open pores and closed pores simultaneously appear in the porous VGCF/MP. And open porosity increased with volume fraction of NaCl particles. The porosity is able be controlled by amount of NaCl particles addition.

(2) MP powders were sintered by heat-treatment but aggregated. VGCFs are connected by sintered MP.

(3) The (002)-plane lattice spacing of the MP heated at 793K was remarkably decreased. The preform showed narrow (002)-plane lattice spacing comparable to that of the VGCFs. The MP achieved crystallization by carbonation.

(4) Undissolved NaCl in closed pores cause the stress concentration then to decrease the compressive yield stress. With infiltration pressure lower than 3 MPa, the porous VGCF/MP with porosity of 91.51 % is still thought can be able to be utilized for the fabrication of MMCs.

(5) The TC of porous VGCF/MP is decreasing with increasing porosity. And the TC of porous VGCF/MP can be improved by carbonation.

(6) The porous VGCF/MP after carbonization with porosity of 91.51 % is still can be utilized to fabricate MMCs for less closed pores.

Reference

[1] X. H. Qu, L. Zhang, M. Wu and S. B. Ren: Progress in Natural Science-Materials International. **21** (2011) 189-197.

[2] S. Mallik, N. Ekere, C. Best and R. Bhatti: Appl. Therm. Eng. **31** (2011) 355-362.

[3] M. Lee, Y. Choi, K. Sugio, K. Matsugi and G. Sasaki: Compos. Sci. Technol. **97** (2014) 1-5.

[4] S. Ren, X. He, X. Qu and Y. Li: J. Alloys Compd. **455** (2008) 424-431.

[5] A. Kalemtas, G. Topates, O. Bahadir, K. Pinar and H. Mandal: T. Nonferr. Metal. Soc. **23** (2013) 1304-1313.

[6] Y. B. Choi, K. Matsugi, G. Sasaki and S. Kondoh: Mater. Trans. **49** (2008) 390-392.

[7] X.-H. Han, Q. Wang, Y.-G. Park, C. T'joen, A. Sommers and A. Jacobi: Heat Transfer Eng. **33** (2012) 991-1009.

[8] M. Lee, Y. Choi, K. Sugio, K. Matsugi and G. Sasaki: Sc.i Eng. Compos. Mater. **18** (2011) 167-171.

[9] H. Zhang, J. Hu, X. Yang and Y. Li: JTST. **1** (2015) 25.

[10] S. Hyun and H. Nakajima: Mater. Sci. Eng., A. **340** (2003) 258-264.

[11] H. Nakajima, S. Hyun, K. Ohashi, K. Ota and K. Murakami: Colloids Surf., A. **179** (2001) 209-214.

[12] W. Zhou, Y. Tang, B. Liu, R. Song, L. Jiang, K. S. Hui, K. N. Hui and H. Yao: Mater. Des. **35** (2012) 414-418.

[13] M. A. El-Hadek and S. Kaytbay: Int. J. Mech. Mater. Des. **4** (2008) 63-69.

[14] M. Reiter and H. Hartman: Journal of Geophysical Research. **76** (1971) 7047-7051.

[15] O. Lee, M. Lee, Y. Choi, K. Sugio, K. Matsugi and G. Sasaki: Mater. Trans. **55** (2014) 827-830.

[16] Y. Arai: Nippon Steel Technical Report. **59** (1993.

[17] F. R. Feret: Analyst. **123** (1998) 595-600.

[18] Y. J. Yang, F. S. Han, D. K. Yang, J. Wu, G. L. Hao and Q. Z. Wang: Powder Metall. **50** (2013) 50-53.

[19] S. Yu, J. Liu, Y. Luo and Y. Liu: Materials Science and Engineering: A. **457** (2007) 325-328.

[20] N. C. Gallego and J. W. Klett: Carbon. **41** (2003) 1461-1466.

[21] J. W. Paek, B. H. Kang, S. Y. Kim and J. M. Hyun: Int. J. Thermophys. **21** (2000) 453-464.

Chapter 3

Development of VGCF/MP Reinforced Al Matrix Composite by Low Pressure Infiltration Method and Their Thermal Property

Contents

Contents 58

3.1 Introduction 59

3.2 Experimental 60

3.2.1 Raw materials and preparation of the porous VGCF/MP 60

3.2.2 Fabrication of VGCF/MP/Al composites by LPI method 61

3.2.3 Characterization of microstructure, porosity, and thermal conductivity 66

3.3 Results and Discussion 67

3.3.1 Effect of volume fraction ratio of VGCF and MP on the Microstructure and porosity of the porous VGCF/MP 67

3.3.2 Microstructure of the VGCF/MP/Al composites 70

3.3.3 TC of porous VGCF/MP and VGCF/MP/Al composites 75

3.4 Summary 77

Reference 79

3.1 Introduction

With development of modern electronic devices, the requirement of heat sink materials is thermal conductivity (TC) equaling to or higher than 200 $W \cdot m^{-1} \cdot K^{-1}$ and coefficients of thermal expansion (CTE) around 6~7 ppm/K [1, 2]. Metal matrix composites (MMCs) with outstanding TC, CTE and low density are considered as promising candidate to replace traditional heat sink material in recent years [3]. On the other hand, carbon fibers reinforced metal matrix composites (MMCs) for heat sink material were focused because of their high thermal conductivity (TC), and ultra-low thermal expansion [1-3]. Especially, the TC of vapor grown carbon fibers (VGCF), a kind of nano carbon fiber, is 1200 $W \cdot m^{-1} \cdot K^{-1}$ [4], which is higher than that of other carbon fibers (~800 $W \cdot m^{-1} \cdot K^{-1}$), about 5 times higher than those of Al (237 $W \cdot m^{-1} \cdot K^{-1}$) and about 3 times higher than those of Cu (386 $W \cdot m^{-1} \cdot K^{-1}$).

As application in the electronic devices, plane fin heat sink as the most common type of heat sink, spreads heat by the surface of fins. According to Newton's law of cooling, a martials with isotropy of heat direction is suitable as fin heat sink material for efficient heat transfer surface area [5]. To achieve MMC with isotropy, continuous phase of reinforcement inside MMCs is necessary. However, carbon fibers have anisotropy. To solve this problem, a network structure of carbon fiber is necessary. Also, the Low-pressure infiltration (LPI) method for fabrication of MMCs with high volume fractions of reinforcements is focused in recent years [6, 7]. In previous study, VGCFs and mesophase pitch powder (MP) were sintered at 823 K to fabricate a porous VGCF/MP as the preform with the network structure, then the porous VGCF/MP was utilized to fabricate MMCs with isotropy by LPI method [8]. However, VGCFs as nanofiber have the problem of easy aggerating and tangling together owing to van der Waals forces and high aspect ratios. Moreover, MP as amorphous has a low TC. These problems are critical factors to the TC of the fabricated MMCs. There are studies about Al or Cu were utilized as matrix of composite for application of heat sink materials [9-18]. Even

Cu have a higher TC than Al, the Al, which has a low density than Cu, is a competitive matrix of MMCs for light weight requirement of automobile and Portable electronic devices. To achieve the TC of VGCF/MP reinforce Al matrix (VGCF/MP/Al) composites, the ideal porous VGCF/MP requires less micro-pores in the cell wall of the preform, good wettability with the Al matrix, and high TC [6-8].

In this study, porous VGCF/MP as preform were fabricated, and the microstructure and the porosity of its were investigated. To improve the wettability of porous VGCF/MP with the Al matrix, the porous VGCF/MP was carried out with electroless Ni plating. Moreover, the porous VGCF/MP were carbonization at high temperature to improve the TC [19]. The effect of carbonization on the TC of porous VGCF/MP was investigated. The VGCF/MP/Al composites were fabricated using the LPI process, and the microstructure and the TC of its were examined.

3.2 Experimental

3.2.1 Raw materials and preparation of the porous VGCF/MP

VGCFs (density: 2.1 kg/m^3, Showa Denko Co., Japan), and MP (density: 2.1 kg/m^3, JFE Chemical Co., Japan), and NaCl particles (density: 2.1 kg/m^3, size: 180~360 μm) as reinforcement were used to fabricate of the porous VGCF/MP. The porous VGCF/MP were fabricated by spacer method and as following steps. First, the VGCFs, MP and NaCl particles were mechanically mixed (tilt of 45°) for 600 s using a glass rod. The NaCl particles were used as the spacer to obtain continuous pores in the porous VGCF/MP. In the Chapter 2, the porous VGCF/MP fabricated with 90 vol.% NaCl particles was proved suitable to the fabrication of VGCF/MP/Al composite. Also, to maintain the infiltration conditions constant, volume fraction of NaCl particles was fixed at 90 vol.%. The resulting mixture was then placed in a graphite mold and compacted under a pressure of 60 MPa. Subsequently, the compacted mixture was sintered in Ar. The sintering process was carried out at 823 K for 3.6 ks. Finally, the sintered samples were immersed in distilled water for 48 h to dissolve NaCl particles followed by drying. The size of the porous VGCF/MP was 10 × ø10 mm^3. To obtain highly crystallized MP, porous VGCF/MP was carried out with the carbonized at 1773 K for 3.6 ks in Ar. Electroless Ni plating is a commonly used surface treatment method to improve wettability between Al and carbon materials, and to prevent the formation of Al_4C_3 [20]. Thus, porous VGCF/MP were carried out with electroless Ni plating. The electroless Ni plating process involved steps of sensitization, activation, and plating [21]. The condition of electroless Ni plating process was for 300 s, pH 6.5 and 293 K. Particularly, to obtain plating layer at the surface of the cell wall in the porous VGCF/MP, the electroless Ni plating process was carried out in a vacuum box with a pressure of -0.8 MPa to fill porous VGCF/MP with bathes in each step.

3.2.2 Fabrication of VGCF/MP/Al composites by LPI method

There are reports that alloys have a better fluidity, which is attribute to the infiltration in fabrication process of MMCs [6, 7, 9, 22-24], than the pure metal. But pure Al has a higher TC than Al alloys. As the porous VGCF/MP was conducted on electroless Ni plating to solve the problem of wettability, the pure Al (purity ≥ 99.7%) was used as the matrix. A pure Al ingot and the porous VGCF/MP were placed into a cylindrical graphite die and then heated to 1023 K in Ar. Subsequently, a pressure lower than 1 MPa was applied to infiltrating molten Al into porous VGCF/MP with a holding time of 3.6 ks.

To optimize the infiltrating pressure, the theoretical infiltrating pressure was calculated. The infiltration of liquid metal into the porous material in infiltrating process depended on several physical factors [25]. In this study, the infiltrating route was simplified to the molten metal infiltrates in the capillary tube between reinforcements. The infiltration types, in particular, are divided into two systems by wettability between the liquid metal and capillary tube. The contact angle θ of molten Al and porous material is defined with the two surface tensions and porous material-liquid interfacial energy σ_{fl} by Young's equation as follows [20, 25, 26]

$$\sigma_{lv}\cdot\cos\theta=\sigma_{pl}-\sigma_{pv} \tag{3.1}$$

where σ_{pv} and σ_{pl} are porous material-vapor surface tension and porous material-liquid interfacial energy. According the contact angle, the wetting system is classified to non-wetting system and spontaneous wetting system, whose contact angle is more than 90° or less than 90°, respectively. As the electroless Ni plating was conducted on with porous VGCF/MP, the porous VGCF/MP-Al interface can be considered as the spontaneous wetting system.

Besides, the curved liquid front in a capillary tube generally called a meniscus. In case of the porous VGCF/MP-Al system electroless Ni plating in a capillary tube, the externally applied infiltration pressure is required because of its spontaneous wetting system between Al and Ni plating with the contact angle of about 4° [20] [27]. However, the infiltration initiation pressure was not determined by only capillary pressure. The schematic diagram of flowing liquid in a capillary tube by exert forces was considered, as shown in Fig. 3.1 [25]. There is a stress field consisted of the capillary resistance P_{cap}, internal viscous friction f, gravity G, back pressure P_{back} and externally applied pressure P_{ram}. And the infiltration starts on with following condition:

$$P_{ram}\geq P_{cap}+P_{back} \tag{3.2}$$

and the P_{cap} is calculated by following equation:

$$P_{cap}=\sigma_{lv}\cdot\Sigma \tag{3.3}$$

where Σ is particle surface area per unit volume for matrix. The Σ is calculated by following equation:

$$\Sigma=\frac{1-V_p}{V_p}S_p \tag{3.4}$$

where S_p is particle surface area per unit volume for preform and V_p volume fraction of particles. The S_p is calculated by following equation:

$$S_p=(1-x_c)S_{fp}+x_cS_{cp} \tag{3.5}$$

where S_{fp} is surface area of fine particles per unit volume, S_{cp} surface area of coarse particles per unit volume and x_c ratio of coarse particles. In this study, each parameter is listed in Table 3.1. By using these parameters, the calculated result of P_{cap} was 1.86 Pa. As the P_{back} is mainly caused by the resistance of air, the P_{back} approximately equals to the atmosphere pressure, which is about 0.1 MPa. Therefore, considering the equation (3.2), the infiltration can start on the condition of infiltration pressure of 0.1 MPa. Thus, the infiltration pressure in this study was decided as 0.1 MPa.

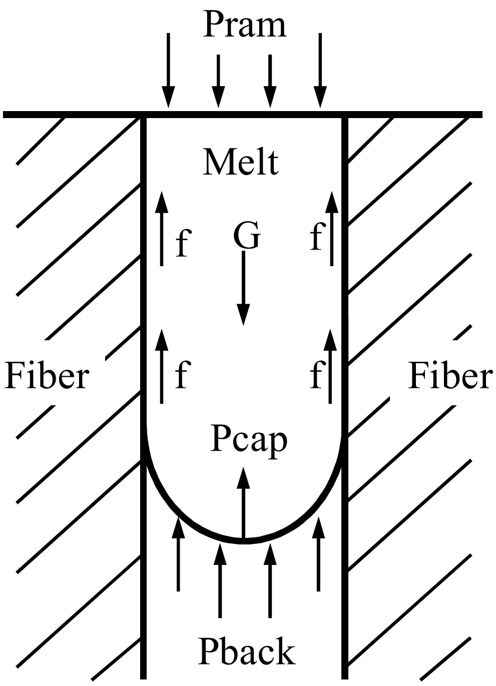

Fig. 3.1 Schematic description of the forces exerted on the flowing melt in a capillary tube, where P_{ram}, P_{cap}, P_{back}, f and G are externally applied pressure, capillary resistance pressure, back pressure, internal viscous friction of the melt and gravity, respectively [25].

Table 3.1 Parameters of molten Al infiltrate to porous VGCF/MP.

Parameter	Value
Liquid-vapor interfacial energy, σ_{lv} [mJ/m^2]	837
Contact angle, θ [deg]	4
V_p	0.9
x_c	1
S_{fp} [m$^{-1]}$	0
S_{fp} [m^{-1}]	19.99

The schematic of the fabrication process for the VGCF/MP/Al composite is shown in Fig. 3.2. And the fabrication of conditions of VGCF/MP/Al are shown in Table 3.2.

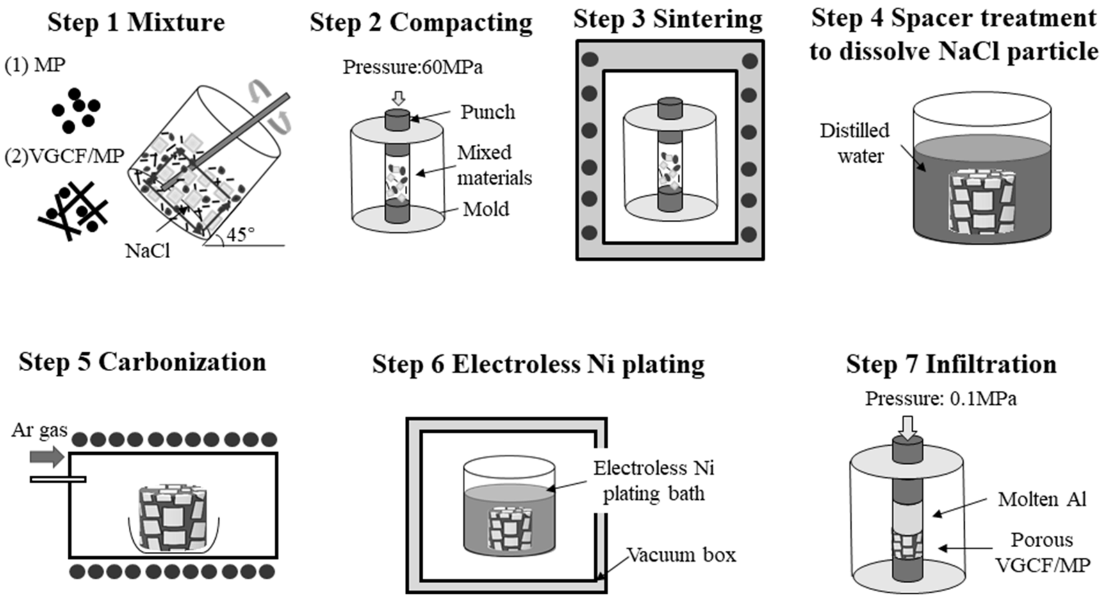

Fig. 3.2 Schematic of the fabrication process for preparing the VGCF/MP/Al composites.

Table 3.2 Fabricated conditions of porous VGCF/MP.

Sample	Volume fraction (vol.%)			Carbonization
	NaCl	MP	VGCFs	
1	90	10	0	Untreated
2	90	10	0	Treated
3	90	9.5	0.5	
4	90	7	3	

3.2.3 Characterization of microstructure, porosity, and thermal conductivity

The microstructure was examined using scanning electron microscopy (SEM; JEOL, JXA-8900). In order to examine the effect of carbonization on MP, the MP before and after carbonization were analyzed by transmission electron microscope (TEM; JEOL, JEM-2010). X-ray diffraction (XRD; D/max-2500/PC, Japan) analysis was also carried out using Cu Kα radiation ($\lambda = 1.54056$ Å) at a scanning speed of 1 °/min over the 2θ range of 20°–90°. The elemental distribution of the composites was determined using an electron probe micro-analyzer (EPMA, JXA8900RL).

By spacer method, the theoretical porosity equals volume fraction of NaCl particles. However, porous VGCF/MP have pores in cell wall and noncontinuous pores. Thus, effective porosity of porous VGCF/MP was calculated by Archimedes method [28], to calculate the open porosity (P_{open}), total porosity (P_{total}) and closed porosity (P_{closed}), following equations were used:

$$\rho_a=\frac{W_1}{W_1-W_2}\times\rho_w \tag{3.6}$$

$$\rho_b=\frac{W_1}{W_3-W_2}\times\rho_w \tag{3.7}$$

$$P_{open}=\frac{W_3-W_1}{W_3-W_2}\times 100\% \tag{3.8}$$

$$P_{closed}=P_{total}-P_{open} \tag{3.9}$$

where W_1, W_2 and W_3 refer to weight of dry preform, impregnated preform in the distilled water and impregnated preform, respectively; ρ_a, ρ_t and ρ_w refer to apparent density of preform, theoretical density of preform and density of distilled water (997.05 kg/m^3, 898 K). The TC of specimens (ø10 × 10 mm^3) was characterized by the steady-state method [29].

3.3 Results and Discussion

3.3.1 Effect of volume fraction ratio of VGCF and MP on the microstructure and porosity of the porous VGCF/MP

Fig. 3.3 shows the SEM images of the porous VGCF/MP and its cell wall. As shown in Figs. 3.3(a)–(d), pores with size of 180~360 μm were formed by dissolved NaCl particles. And continuous pores were formed by connected NaCl particles. But closed pores were also observed formed by isolated NaCl particles. As shown in Figs. 3.3(a) and 3.3(b), the cell walls were consisted by sintered MP. As shown in Fig. 3.3(b) and 3.3(c), micro-pore with size of 1~2 μm was observed in the cell wall for the removement

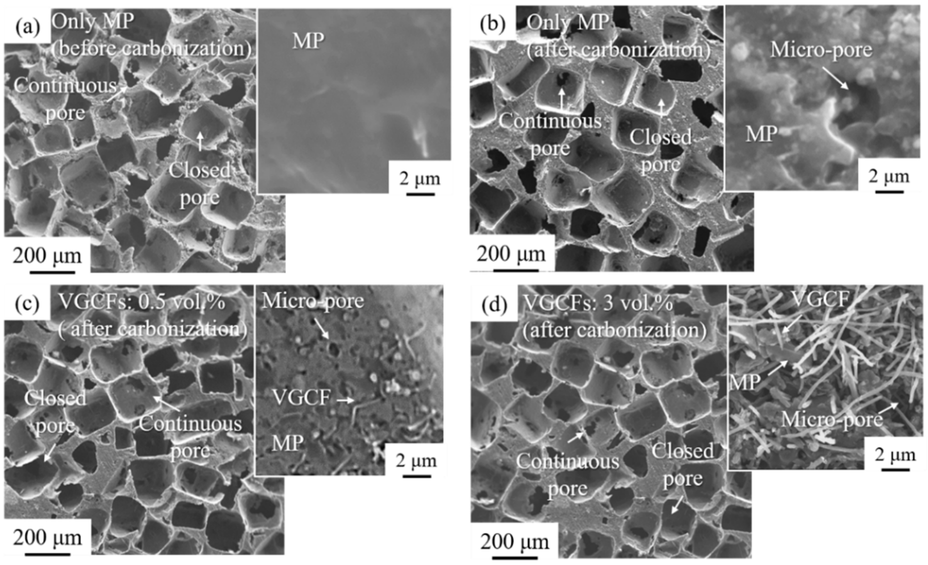

Fig. 3.3 SEM images of porous VGCF/MP: (a) only MP and before carbonization, (b) only MP and after carbonization, (c) MP & 0.5 vol.% VGCFs and after carbonization, and (d) MP & 3 vol.% VGCFs and after carbonization (the inserts are higher magnification images of each porous VGCF/MP's cell wall).

of the impurities by the carbonization. As shown in Figs. 3.3(c) and 3.3(d), the cell walls were consisted by sintered MP and VGCFs. But with addition of VGCFs at 3 vol.%, numerous micro-pores with a random shape and size of 1~8 μm were observed in the cell wall, as shown in Fig. 3.3(d). This is because the addition of VGCFs at 3 vol.% leaded the aggeation of VGCFs. Fig. 3.4 illustrates the porosities of porous VGCF/MP with different fabrication conditions. As shown in Fig. 3.4, the range of P_{total} of porous VGCF/MP was 91.0~91.9% except the porous VGCF/MP fabricated with 3 vol.% VGCFs and after carbonization, which's porosity was 95.1%. The range of P_{open}

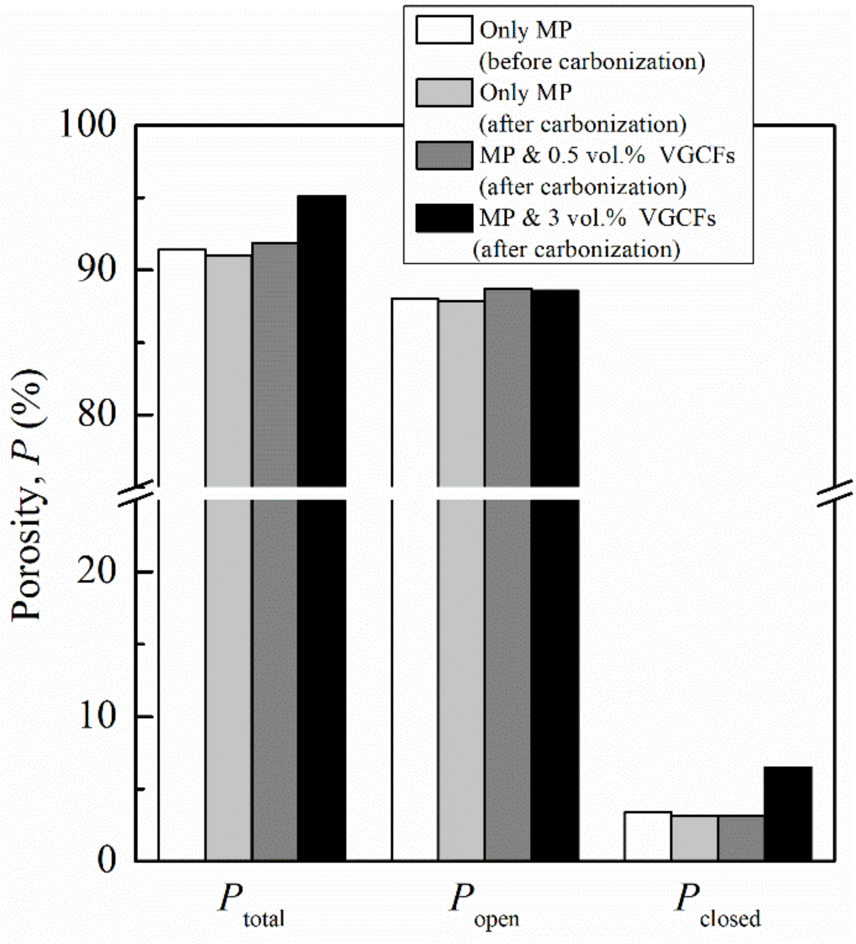

Fig. 3.4 Porosity of porous VGCF/MP with different fabricated conditions.

of porous VGCF/MP was 87.9~88.72%, which indicated fabrication of porous VGCF/MP were achieved. And the porous VGCF/MP fabricated with addition of 0~0.5 vol% VGCFs, which's range of P_{closed} was 3.1~3.4%. The P_{closed} was caused by the closed pores in porous VGCF/MP corresponding with Figs. 3.3(a)–(c). However, owning to closed pores and micro-pores in the cell wall of porous VGCF/MP with the addition of 3 vol.% VGCFs (see Fig. 3.3(d)), the P_{closed} was increased to 6.5%.

To examine the thickness of Ni plating applied on porous VGCF/MP, the Ni plated porous VGCF/MP (only MP and before carbonization) were buried by resin and its BSE image is shown in Fig. 5. In Fig. 5, the resin filled the pore which formed by dissolved NaCl particle. The white region between resin and VGCF/MP represents the Ni plating. The thickness of Ni plating is approximately 1μm.

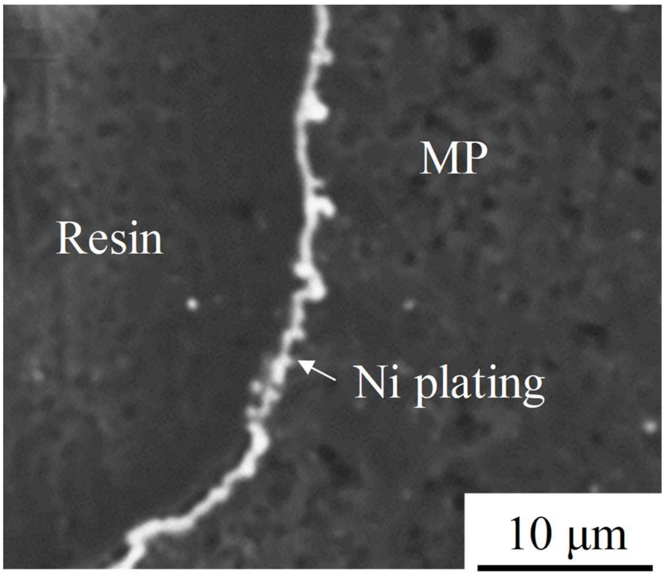

Fig. 3.5 BSE image of electroless Ni plated porous VGCF/MP (only MP and before carbonization) buried by resin.

3.3.2 Microstructure of the VGCF/MP/Al composites

Figs. 3.6(a)–(d) shows the microstructures of the VGCF/MP/Al fabricated with different conditions. The dark and gray regions represent the VGCF/MP and the Al matrix, respectively. As shown in Figs. 3.6(a)–(d), the VGCF/MP is a continuous phase in the Al matrix. This result indicated fabrication of VGCF/MP/Al composites with anisotropy were achieved. However, voids observed in Figs. 3.6(a)–(d). As the high-magnification SEM image insert in Fig. 3.6(a), the void was surrounded by the

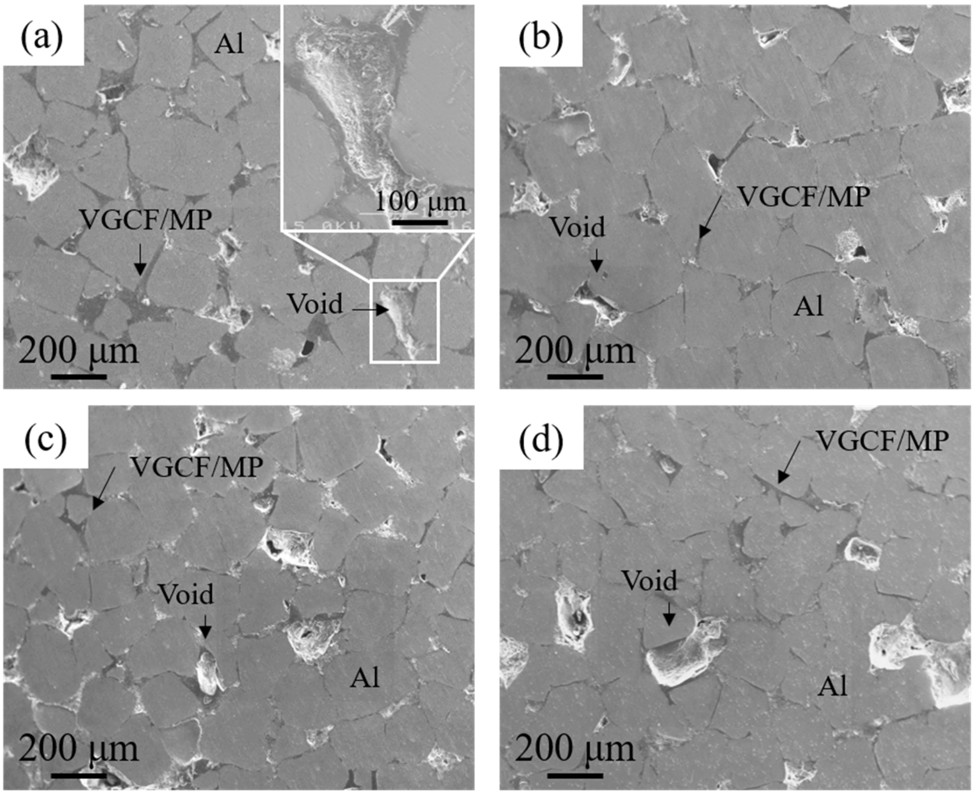

Fig. 3.6 SEM images of VGCF/MP/Al composites: (a) with only MP and before carbonization, (b) with only MP and after carbonization, (c) with MP & 0.5 vol.% VGCFs and after carbonization, and (d) with MP & 3 vol.% VGCFs and after carbonization.

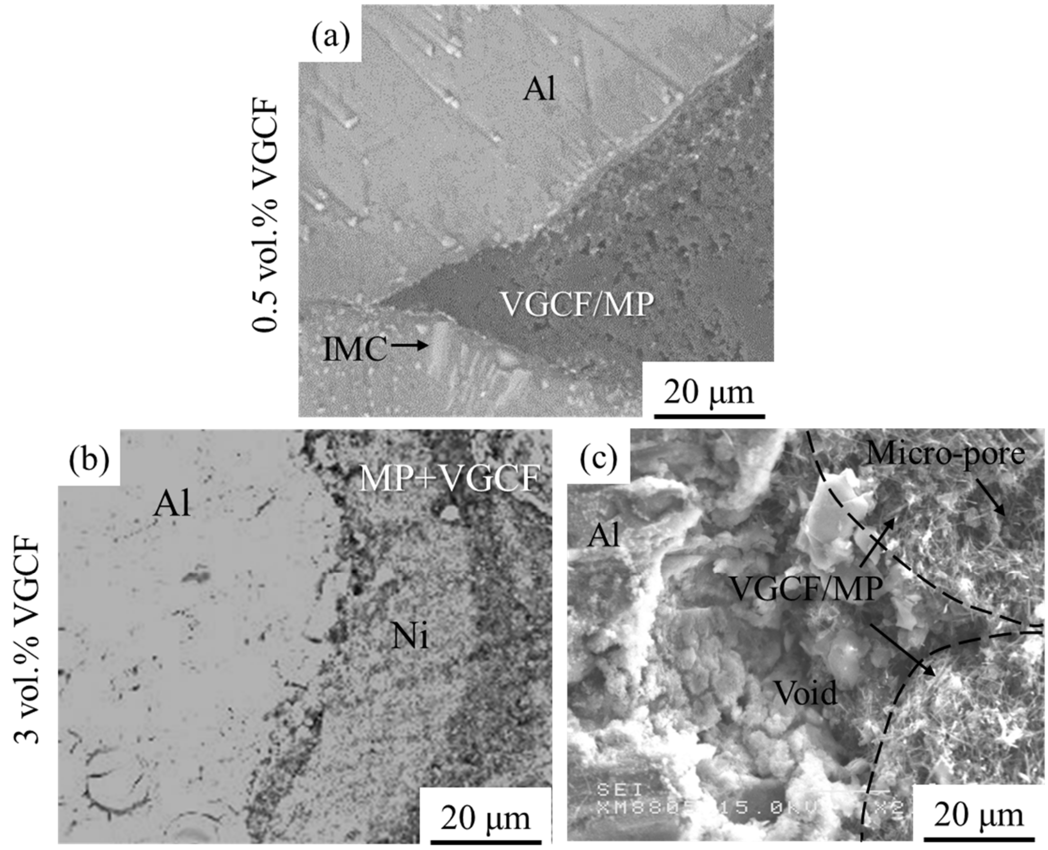

Fig. 3.7 SEM images of interface between VGCF/MP and Al matrix:
(a) with MP & 0.5 vol.% VGCFs and after carbonization;
(b), and (c) with MP & 3 vol.% VGCFs and after carbonization.

VGCF/MP and had the same shape of the closed pore in Fig. 3.3. The reason was that closed pores isolated with other pores in porous VGCF/MP, than molten Al not infiltrated this part of the VGCF/MP/Al composites in LPI processing. Moreover, the interface between the VGCF/MP and Al matrix, which was affected by volume fraction of VGCFs, is a critical fact to affect the TC of fabricated VGCF/MP/Al composites. Thus, the interfaces between the VGCF/MP and Al matrix with addition of 0.5 and 3 vol.% were observed, and the results is shown in Figs. 3.7(a) and 3.7(b), respectively. As shown in Fig. 3.7(a), in the VGCF/MP/Al composite with addition of 0.5 vol%

VGCFs, the interface between the VGCF/MP and the Al matrix is intimate. The intimated interface was attributed to the improved wettability between VGCF/MP and Al matrix by Ni plating, also indicated the good bonding between VGCF/MP and Al matrix. And a light-gray phase was observed in the Al matrix, it is inferred to be metallic compounds (IMCs) formed by the reaction of the Ni plating and the molten Al. As shown in Fig. 3.7(b), in the VGCF/MP/Al composite with the addition of 3 vol.% VGCFs, a void was observed the interface between the VGCF/MP and the Al matrix, and a gap at the side of VGCF/MP were also observed. Because of the addition of 3 vol.% VGCFs, the VGCF/MP was aggerated, which resulted the VGCF/MP became discontinuous rather than a continuous structure (see Fig. 3.7(a)). Moreover, the Ni plating was not observed at the side of the VGCF/MP, it is indicted that the gap caused by the aggregation of VGCF/MP hindered formation of Ni plating. Specifically, the gap had an acute angle, which caused the bathes utilized in the electroless Ni plating process

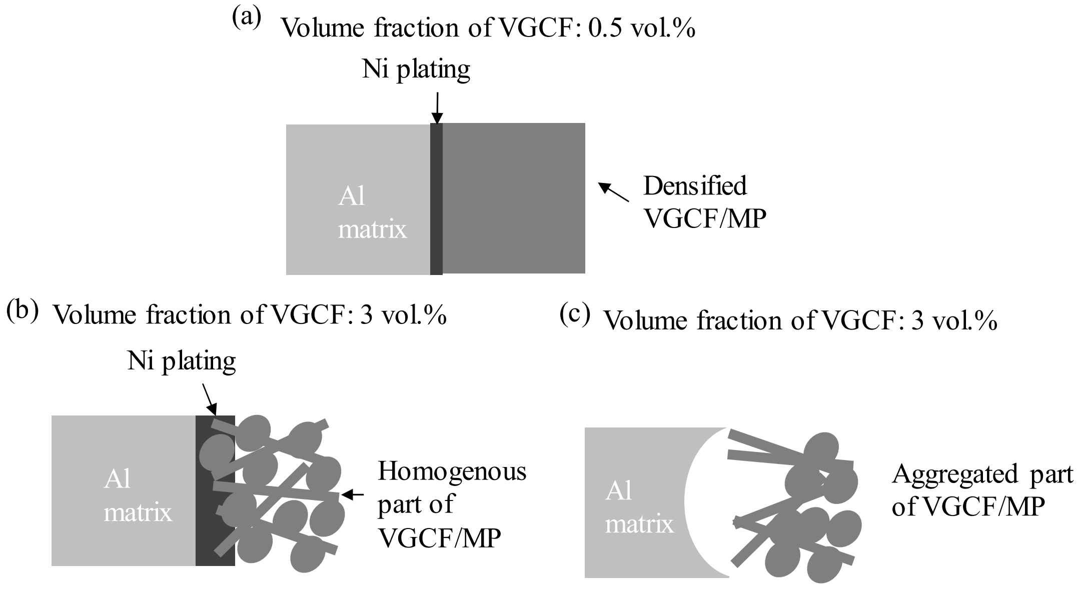

Fig. 3.8 Schematic of of interface between VGCF/MP and Al matrix:

(a) with MP & 0.5 vol.% VGCFs and after carbonization;

(b), and (c) with MP & 3 vol.% VGCFs and after carbonization.

does not infiltrate this part. As the poor wettability between Al and carbon materials [20], without Ni plating, the void at the interface between the VGCF/MP and the Al matrix was formed.

To investigate the elemental distribution of VGCF/MP/Al composite (MP and 0.5 vol.% VGCFs, after carbonization), EMPA was carried out at same area of Fig. 3.7(a), and this result is shown in Fig. 3.8. Furthermore, point analysis of IMC was carried out on the region marked with a cross in Fig. 3.8(a). The Al:Ni atomic ratio of the IMC region was found to be approximately 3:1. As shown in Figs. 3.8(b) and 3.8(d), the Al and Ni overlapped at the IMC regions, indicating the formation of Al-Ni IMCs. Thus, the IMC was identified to be Al_3Ni. The reaction at interface between VGCF/MP and Al matrix was shown in equation (3.10).

$$3Al+Ni=Al_3Ni \qquad (3.10)$$

Moreover, there were no overlapped region of Al element and C element (see Figs. 3.8(b) and 3.8(c)), this result indicates Ni plating prevented the reaction between of the molten Al and the VGCF/MP. Therefore, the formation of Al_4C_3 at the infiltrating temperature of 1037 K was avoided.

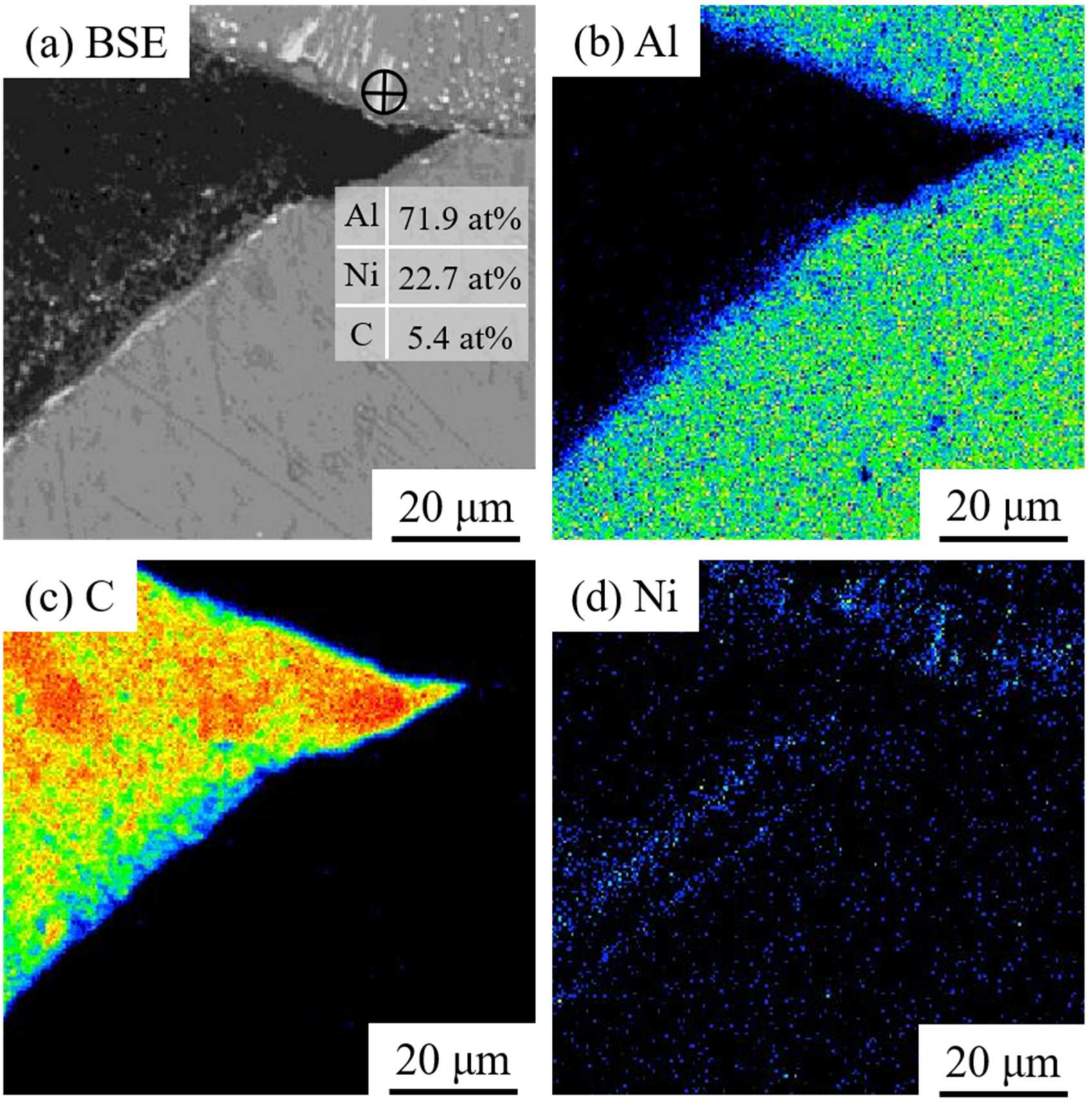

Fig. 3.8 Element distribution of VGCF/MP/Al composites fabricated with condition of MP & 0.5 vol.% VGCFs and after carbonization: (a) BSE image (inset for location and result of point analysis), (b) Al element, (c) C element, and (d) Ni element.

3.3.3 TC of porous VGCF/MP and VGCF/MP/Al composites

The TCs of fabricated porous VGCF/MP and VGCF/MP/Al composite with different fabricated conditions are shown in Figs. 3.9(a) and 3.9(b), respectively. As shown in Fig. 3.9(a), the TC of porous VGCF/MP was increased for the crystallization of MP and the addition of 0.5 vol.% VGCFs. Considering heat in nonmetal is transferred by phonon, the MP with higher crystallization had a higher phonon velocity then amorphous [22]. And the VGCF have a TC of 1200 W·m^{-1}·K^{-1}. Therefore, the TC of porous VGCF/MP was improved by the carbonization and the addition of 0.5 vol.% VGCFs. However, with increased volume fraction of VGCFs to 3 vol.%, the TC of porous VGCF/MP decreased. As the porosity is a critical factor to the TC of the porous materials [30], this decrease in the TC can be attributed to micro-pores which caused by the aggregation of the VGCF/MP in cell wall. As shown in Fig. 3.9(b), the TC of the VGCF/MP/Al composite is consistent with the TC of porous VGCF/MP (see Fig. 3.9(a)). Moreover, with the addition of VGCFs increased from 0.5 to 3 vol.%, the TCs

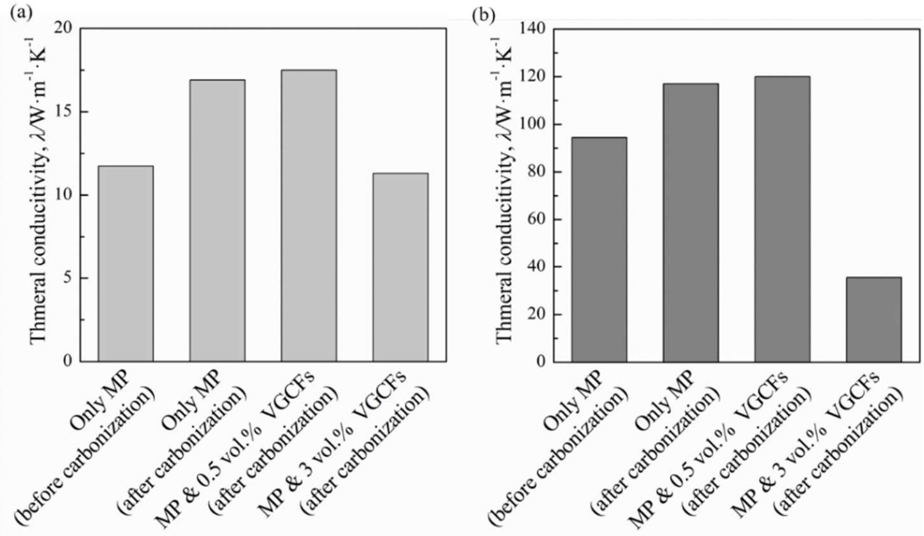

Fig. 3.9 TC of (a) porous VGCF/MP and (b) VGCF/MP/Al composites with different fabricated conditions.

of the VGCF/MP/Al composites dramatically decreased from 120.1 W·m^{-1}·K^{-1} to 35.5 W·m^{-1}·K^{-1}. This is because the 3 vol.% VGCFs caused micro-pores in cell wall not be infiltrated, and the voids at interface between VGCF/MP and Al matrix. However, the TC of these composite with 0.5 vol.% VGCFs and carbonization were lower than the TC of Al (237 W·m^{-1}·K^{-1}). This is because the thermal resistance at the interface and the formation of the Al_3Ni whose TC is approximately 35 W·m^{-1}·K^{-1} [31]. But in the Al-Ni system, the formation of Al_3Ni can be suppressed by the addition of Ni to the Al matrix. Also, a higher crystallized MP than present study can be achieved by temperature higher than 1037 K [19, 32], which can improve the TC of porous VGCF/MP. It has also been reported that the carbon nanofiber reinforced Al matrix composites with TC over 200 W·m-1·K-1 can be fabricated via powder metallurgy 21). However, unlike the powder metallurgy method, a low infiltration pressure of 0.1 MPa was utilized in this paper for the fabrication of the VGCF/MP/Al composites. The low pressure infiltration method allows for the fabrication of composites necessary for heat sinks with a large size and complex shape 22). The data presented in this study does indicate the viability of these composites for industrial use and the commercialization of the final product. Thus, while still needing further study, VGCF/MP/Al composites, are potential materials for heatsinks in the future.

3.4 Summary

Porous VGCF/MP with high porosities were prepared by spacer method. The VGCF/MP/Al composites were successfully fabricated using the LPI method at 0.1 MPa. The main conclusions of the study are as follows:

(1) In the porous VGCF/MP, pores with size of 180-360 μm were formed by dissolved NaCl particles. And the cell walls of porous VGCF/MP were sintered by MP. With volume fraction of 0–0.5 vol.%, the cell walls of porous VGCF/MP had a continuous structure. But with addition of VGCF at 3 vol.%, numerous micro-pores were caused by aggregation of VGCFs in the cell wall, which resulted the P_{closed} was increased to 6.5%. By carbonization, the structure of MP is switched from disorder structure to layer structure by carbonization. And the MP had a high crystallinity due to the carbonization.

(2) VGCF/MP/Al composites with anisotropy were achieved by the VGCF/MP as a continuous phase in the Al matrix. But the voids with same shape of NaCl particle were observed in the VGCF/MP/Al composites for the closed pores. The VGCF/MP/Al composites with the addition of 0–0.5 vol.% VGCFs had an intimated interface between VGCF/MP and Al matrix. While with the addition of 3 vol.% VGCFs, void was formed for the aggregation of VGCF/MP. The Ni plating improved the wettability between VGCF/MP, and Al3Ni was formed by the reaction of the Ni plating and Al matrix in infiltration process.

(3) With the carbonization and addition of 0.5 vol.% VGCFs, the TCs of the VGCF/MP/Al composites increased because of the crystallization of the MP and the high TC of the VGCF. However, with addition of 3 vol.% VGCFs, the TC of the VGCF/MP/Al composite decreased because of the aggregation of VGCFs. And

the Al3Ni in Al matrix was also an unfavorable factor to the TC of VGCF/MP/Al composites.

Reference

[1] P. K. Schelling, L. Shi and K. E. Goodson: Mater. Today. **8** (2005) 30-35.

[2] S. Mallik, N. Ekere, C. Best and R. Bhatti: Appl. Therm. Eng. **31** (2011) 355-362.

[3] G. Lalet, H. Kurita, J. M. Heintz, G. Lacombe, A. Kawasaki and J. F. Silvain: Journal of Materials Science. **49** (2014) 397-402.

[4] Y.-M. Chen and J.-M. Ting: Carbon. **40** (2002) 359-362.

[5] B. L. Whatley, U.S. Patents, 2005.

[6] S. Ren, X. He, X. Qu and Y. Li: J. Alloys Compd. **455** (2008) 424-431.

[7] B. S. Rao and V. Jayaram: Acta Mater. **49** (2001) 2373-2385.

[8] F. Gao, Y. Choi, K. Matsugi, Z. Xu, K. Sugio and G. Sasaki: Conference name.ed. by, (Conference location, Year.

[9] T. Schubert, A. Brendel, K. Schmid, T. Koeck, W. Zieliński, T. Weißgärber and B. Kieback: Composites Part A. **38** (2007) 2398-2403.

[10] X.-H. Han, Q. Wang, Y.-G. Park, C. T'joen, A. Sommers and A. Jacobi: Heat Transfer Eng. **33** (2012) 991-1009.

[11] J. Liao and M.-J. Tan: Powder Technol. **208** (2011) 42-48.

[12] E. T. Thostenson, Z. Ren and T.-W. Chou: Compos. Sci. Technol. **61** (2001) 1899-1912.

[13] K. Shirvanimoghaddam, S. U. Hamim, M. K. Akbari, S. M. Fakhrhoseini, H. Khayyam, A. H. Pakseresht, E. Ghasali, M. Zabet, K. S. Munir and S. Jia: Composites Part A. **92** (2017) 70-96.

[14] M. Lee, Y. Choi, K. Sugio, K. Matsugi and G. Sasaki: Compos. Sci. Technol. **97** (2014) 1-5.

[15] K. Sugio, Y.-B. Choi and G. Sasaki: Mater. Trans. **57** (2016) 582-589.

[16] R. Prieto, J. Molina, J. Narciso and E. Louis: Scripta Mater. **59** (2008) 11-14.

[17] J.-F. Silvain, C. Vincent, J.-M. Heintz and N. Chandra: Compos. Sci. Technol. **69** (2009) 2474-2484.

[18] X. H. Qu, L. Zhang, M. Wu and S. B. Ren: Progress in Natural Science-Materials International. **21** (2011) 189-197.

[19] Y. Arai: Nippon Steel Technical Report. **59** (1993.

[20] S. Ip, R. Sridhar, J. Toguri, T. Stephenson and A. Warner: Materials Science and Engineering: A. **244** (1998) 31-38.

[21] Y. Choi, Z. Zu, K. Matsugi, K. Sugio and G. Sasaki: Mater. Trans. **58** (2017) 834-837.

[22] S. I. Oh, J. Y. Lim, Y. C. Kim, J. Yoon, G. H. Kim, J. Lee, Y. M. Sung and J. H. Han: Journal of Alloys & Compounds. **542** (2012) 111-117.

[23] F. Stadler, H. Antrekowitsch, W. Fragner, H. Kaufmann and P. J. Uggowitzer, in *ICAA13 Pittsburgh*, Springer, 2012, pp. 137-142.

[24] M. Pech-Canul, R. Katz and M. Makhlouf: Metallurgical and Materials Transactions A. **31** (2000) 565-573.

[25] S. Long, Z. Zhang and H. Flower: Acta metallurgica et materialia. **42** (1994) 1389-1397.

[26] B. B. Singh and M. Balasubramanian: J. Mater. Process. Technol. **209** (2009) 2104-2110.

[27] K. Landry, S. Kalogeropoulou, N. Eustathopoulos, Y. Naidich and V. Krasovsky: Scripta Mater. **34** (1996）.

[28] J. Locs, V. Zalite, L. Berzina-Cimdina and M. Sokolova: J. Eur. Ceram. Soc. **33** (2013) 3437-3443.

[29] F. R. Feret: Analyst. **123** (1998) 595-600.

[30] J. W. Paek, B. H. Kang, S. Y. Kim and J. M. Hyun: Int. J. Thermophys. **21** (2000) 453-464.

[31] Y. Terada, K. Ohkubo, T. Mohri and T. Suzuki: Mater. Trans. **43** (2002) 3167-3176.

[32] V. Gergely and B. Clyne: Adv. Eng. Mater. **2** (2000) 175-178.

Chapter 4

Microstructure and Thermal Conductivity of Carbon Nanotube Block Reinforced Aluminum Matrix Composite

Contents

Contents *82*

4.1 Introduction.. *83*

4.2 Experimental *84*

  4.2.1 Raw materials and electroless Cu plating on CNT block *84*

  4.2.2 Fabrication of CNT block/Al composite and characterization *88*

4.3 Results and Discussion *89*

  4.3.1 Effect of plating time on the thickness of the Cu layer.. *89*

  4.3.2 Microstructure of the CNT block/Al composites.. *93*

  4.3.3 Thermal stress at the interface between CNT block and Al matrix.. *98*

  4.3.4 TC of the CNT block/Al composites *102*

4.4 Summary *104*

Reference.. *105*

4.1 Introduction

Carbon nanotubes (CNTs) are considered to be ideal reinforcements for high-performance metal matrix composites (MMCs) because of their outstanding mechanical and thermal properties such as high tensile strength, high elastic modulus, high thermal conductivity (TC), and ultra-low thermal expansion [1-3]. The TC of CNTs is 3000~6000 $W \cdot m^{-1} \cdot K^{-1}$ [4], which is higher than that of carbon fibers (~800 $W \cdot m^{-1} \cdot K^{-1}$) [5] and about 10 times higher than those of Al (237 $W \cdot m^{-1} \cdot K^{-1}$) and Cu (386 $W \cdot m^{-1} \cdot K^{-1}$). However, dispersed CNTs always agglomerate and tangle together owing to their very strong van der Waals forces and high aspect ratios, and hence lead to the formation of numerous pores in CNT-reinforced composites [6-8]. This limits the application of CNTs for the fabrication of MMCs [9-14]. Accordingly, MMCs with dispersed CNTs cannot be effectively used as heat sink materials [15, 16]. CNTs can be easily aligned in a single direction (by van der Waals forces). Aligned CNTs (CNT blocks) show particle structures. Therefore, the fabrication of CNT block-reinforced MMCs can be simplified by using CNT blocks instead of CNTs (dispersion step can be avoided). The use of CNT blocks yields MMCs with fewer pores. Such CNT block-reinforced MMCs are considered to be potential candidates for heat sink applications.

The low-pressure infiltration (LPI) method has been used to fabricate MMCs with high volume fractions of reinforcements [17]. In this method, a molten metal is infiltrated into a porous preform at a low pressure. To improve the wettability of CNT blocks and the molten metal, electroless plating is often carried out as a surface treatment [15, 18]. In addition, it is reported that SiO_2 was utilized as binder to fabricate the SiC preform of SiC reinforced Al matrix composites [19]. Thus, the electroless plating layer can used as binder to fabricate the CNT block preforms, which is contribute to simple the fabrication process of MMCs. As the binder, the electroless plating layer must be sufficiently thick to provide sufficient bonding strength. However, the electroless plating layer and molten Al decrease the TC of the resulting intermetallic compound (IMC) [20]. Therefore, the electroless layer significantly affects the microstructure and TC, and hence the performance of the MMC.

In this study, the CNT block-reinforced Al matrix (CNT block/Al) composites were fabricated using the LPI process, and the effects of the Cu layer on its microstructure and TC were investigated. The microstructures of the fabricated electroless Cu-plated CNT blocks and CNT block/Al composites were examined. Moreover, the effects of defects and IMCs on the TC of the CNT block/Al composites were investigated.

4.2 Experimental

4.2.1 Raw materials and electroless Cu plating on CNT block

High-porosity preforms were fabricated using CNT blocks (density: 2.0 g·cm^{-3}, Zeon Nano Technology Co. Ltd., Japan, Fig. 4.1) Especially, the CNT blocks showed a width of 100–200 μm and a thickness of 100–200 μm. Each CNT block consisted of uniformly and unidirectionally aligned CNTs. NaCl particles with sizes in the range of 180~360 μm. The NaCl particles were used as the spacer to obtain continuous pores in the preform.

Prior to the perform fabrication, the as-received CNT blocks were subjected to electroless Cu plating. To improve the wettability of CNT blocks and the molten metal, electroless Cu or Ni plating is often carried out as a surface treatment [18, 21-23]. In this

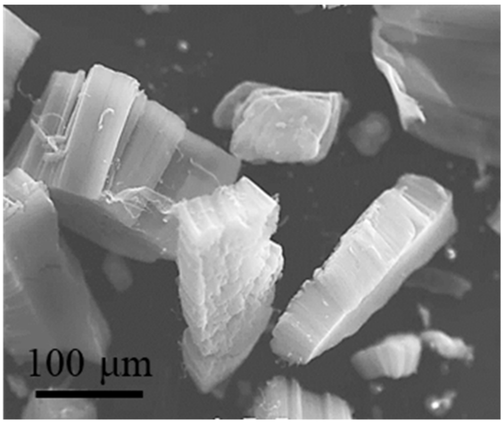

Fig. 4.1 SEM image of as received CNT blocks.

Table 4.1 Properties of Cu and Ni.

	Melting point [K]	Sintering temperature [K]	Contact angle with molten Al at 1073K as electroless plating [°]
Ni	1728 [27]	1173~1364 [24]	4 [18]
Cu	1358 [28]	989~1086 [29]	12.6~26 [21]

Table 4.2 Bathes used in electroless Cu plating of each step.

	Slat	Concentration	Carry out conditions
Sensitizing	$SnCl_2 \cdot H_2O$ HCl	40 g/L 20 ml/L	300s and room temperature
Activation	$PdCl_2 \cdot 2H_2O$ HCl	0.4 g/L 50 ml/L	300s and room temperature
Plating	$CuSO_4 \cdot 5H_2O$ EDTA NaCOOH HCHO (36%)	10 g/L 45 g/L 20 g/L 16 ml/L	Various time, pH 12 and 313 K

study, the properties of electroless plating are key factors to fabricate CNT block/Al composite. Thus, the properties of Cu and Ni are summarized in Table. 4.1. Comparing the contact angle with molten Al at 1073K, the electroless Ni has a lower contact angle than its of Cu, which indicated a better wettability. However, the sintering temperature of Ni (>1173 K [24]) is higher than the melting point of NaCl (1074 K). A sintering temperature higher than the melting point of NaCl may destroy the structure of CNT block preform. Also, as calculated in Chapter 3 of this thesis, capillary pressure in the preform is about a few of PASCAL of a spontaneous wetting system, which is much lower than the atmosphere pressure. Thus, electroless Cu plating was used in this study and the infiltration pressure was set 0.1 MPa in the following step.

The electroless Cu plating process involved sensitization, activation, and plating [25, 26]. The bathes used in each step are listed as Table 4.2 and the schematic of each step is shown as Fig. 4.2. To vary the thickness of the Cu layer, different plating times were used: 15, 30, 60, and 180 s (pH 12, 313 K). The electroless Cu-plated CNT blocks were buried in a resin and were then polished mechanically. The thicknesses of the Cu layers were measured using an image analysis software (Image Pro Plus 5.0). The preforms were fabricated as follows. First, the Cu-plated CNT blocks and NaCl particles were mechanically mixed (tilt of 45°) for 600 s using a glass rod. To maintain the infiltration conditions constant, the preform porosity was fixed at 90%. The electroless Cu-plated CNT block:NaCl particle volume ratio was fixed at 1:9. The resulting mixture was then placed in a graphite mold and compacted under a pressure of 60 MPa. Subsequently, the compacted mixture was sintered in Ar. The sintering process was carried out at 973 K for 1.8 ks. Finally, the sintered samples were immersed in distilled water for 48 h to dissolve NaCl particles followed by drying. The size of the preform was 10 × ø10 mm^3.

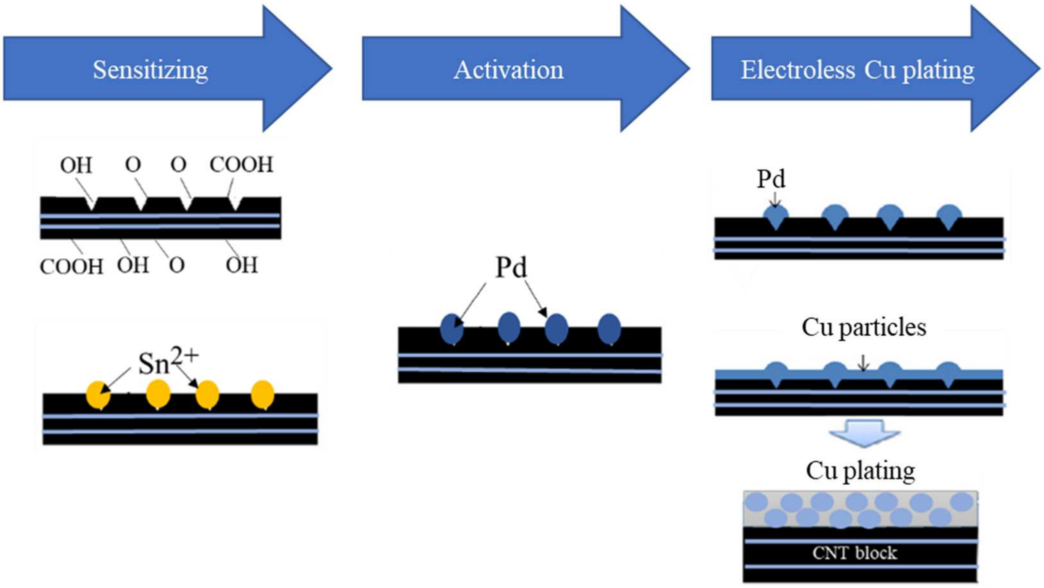

Fig. 4.2 Schematic diagram of electroless Cu plating on CNT blocks.

4.2.2 Fabrication of CNT block/Al composite and characterization

Pure Al (purity ≥ 99.7%) was used as the matrix. A pure Al ingot and the fabricated CNT block preform were placed into a cylindrical graphite die and then heated to 1037 K in Ar. The applied pressure and holding time were 0.1 MPa and 3.6 ks, respectively. The schematic of the fabrication process for the CNT block/Al composite is shown in Fig. 4.3. The microstructures of the CNT block/Al composites were observed using scanning electron microscopy (SEM; JEOL JXA8900; 15 kV). The elemental distribution of the composites was determined using an electron probe micro-analyzer (EPMA, JXA8900RL). X-ray diffraction (XRD; D/max-2500/PC, Japan) analysis was carried out using Cu Kα radiation ($\lambda = 1.54056$ Å) at a scanning speed of 1 °/min over the 2θ range of 20°~90°. The TCs of the fabricated CNT block/Al composites were measured using the steady-state method [30].

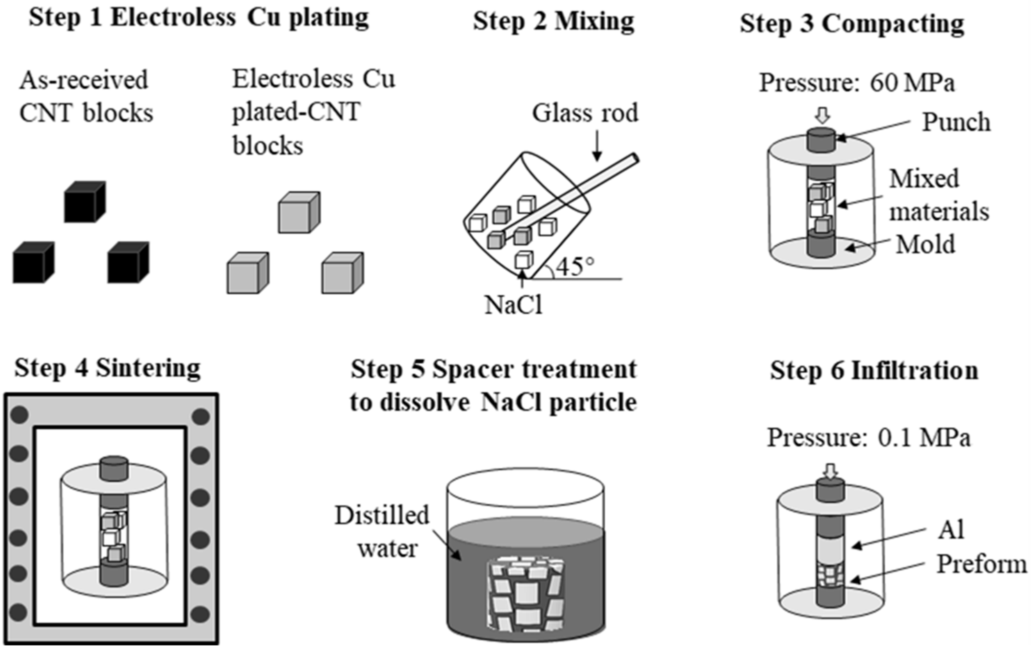

Fig. 4.3 Schematic image of fabrication process of CNT block/Al composites.

4.3 Results and Discussion

4.3.1 Effect of plating time on the thickness of the Cu layer

Fig. 4.4 shows the morphologies of the electroless Cu-plated CNT blocks with different plating times. As can be observed from Figs. 2(a), 2(c), 2(e) and high magnification images of each sample, the electroless Cu-plated CNT blocks (plating times of 15~60 s) showed a smooth and uniform Cu layer. However, at the plating time of 180 s, dendritic growth occurred, making the surface of the Cu layer rough, as shown in Fig. 4.4(g) and 4.4(h).

The thickness of the Cu layer was measured since it played an important role in the infiltration process. Fig. 4.5 shows the cross-section of the electroless Cu-plated CNT blocks obtained at different plating times (15~180 s). The white regions represent the Cu layers. The CNT blocks showed unbonded parts. The thicknesses of the Cu layers formed at the plating times of 15, 30, 60, and 180 s were 2.6, 3.6, 5.2, and 9.3 μm, respectively (Figs. 3 (a), (b), (c), and (d), respectively). The relation between the thickness of the Cu layer and the plating time is shown in Fig. 4.6. According to Fig. 4.6, this can be expressed as follows:

$$d=0.63t^{0.52} \tag{4.1}$$

where d and t are the thickness of the Cu layer and plating time, respectively. The thickness of the Cu layer increased with an increase in the plating time (15~180 s). The CNT block:Cu volume ratio was calculated using the density of Cu (8.96 $g\cdot cm^{-3}$). The Cu layer thicknesses and CNT block:Cu volume ratios for the composites are listed in Table 4.3.

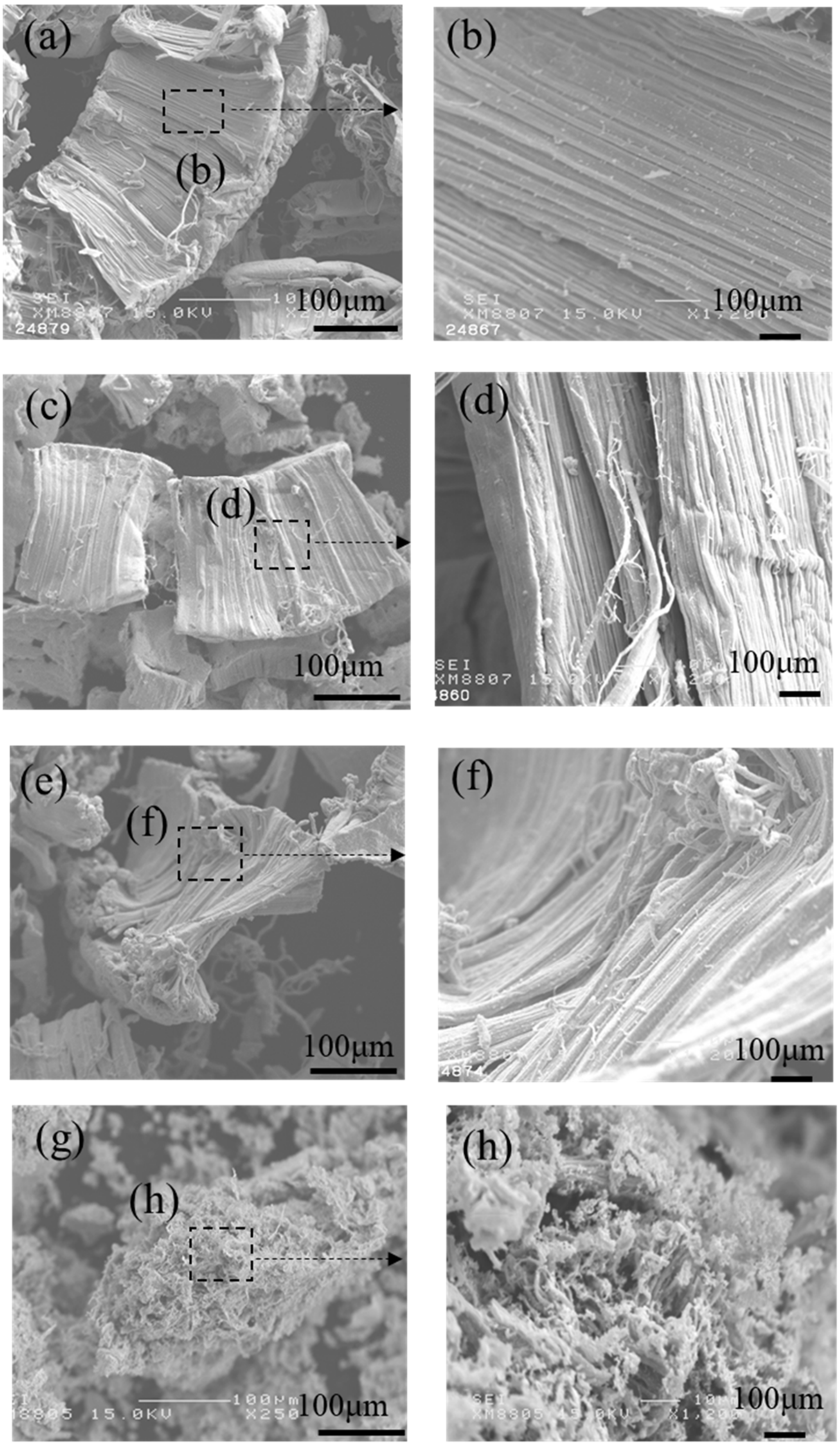

Fig. 4.4 SEM images of (a), (c), (e), and (g) electroless Cu-plated CNT blocks of 15, 30, 60, and 180 s and (b), (d), (f), and (g) higher magnification of electroless Cu-plated layer of each sample, respectively.

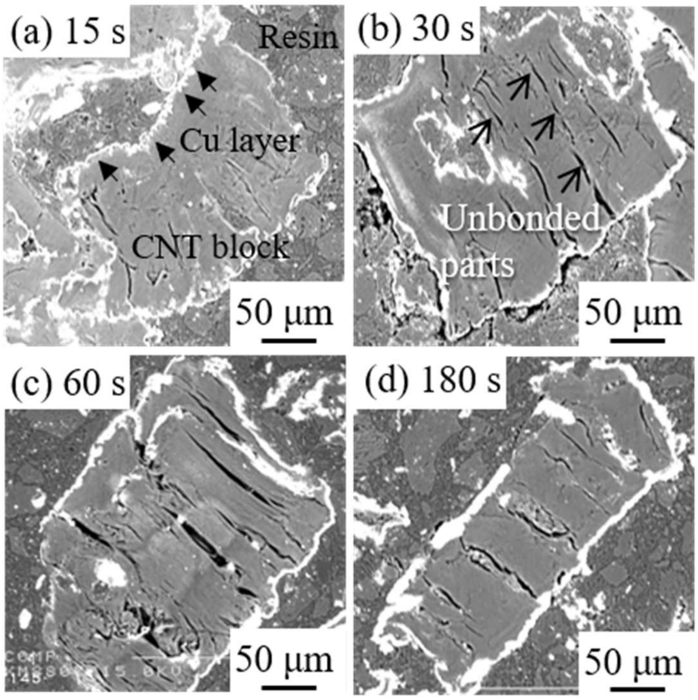

Fig. 4.5 BSE images of cross section of electroless Cu-plated CNT blocks with different plating times: (a) 15 s, (b) 30 s, (c) 60s, and (d) 180s.

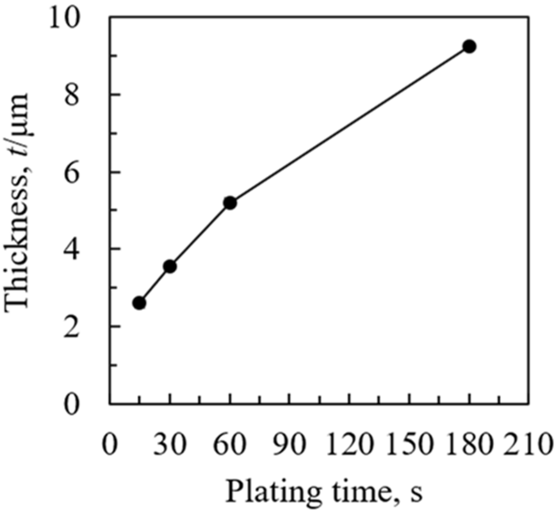

Fig. 4.6 Relation of thicknesses of Cu layers on electroless Cu-plated CNT blocks with different plating times.

Table 4.3 Thicknesses of Cu layer and CNT block:Cu volume ratios with different plating times.

Sample	Plating time [s]	Thickness [*t*/μm]	CNT block:Cu volume ratio, (Fixed 10 vol.%)
1	15	2.6	8.8:1.2
2	30	3.6	7.9:2.1
3	60	5.2	6.8:3.2
4	120	9.3	3.7:6.3

4.3.2 Microstructure of the CNT block/Al composites

Figs. 4.7(a), 4.7(c), 4.7(e), and 4.7(g) show the microstructures of the CNT block/Al composites fabricated with different CNT block:Cu volume ratios, and Figs. 4.7(b), 4.7(d), 4.7(f), and 4.7(h) show the corresponding high-magnification SEM images. The dark and gray regions represent the CNT blocks and the Al matrix, respectively. The composites showed no pores. This indicates that the fabricated CNT block/Al composites showed high relative densities. At the interface between the CNT blocks and the Al matrix, light regions corresponding to the Cu layers were observed (Figs. 4.7(b), 4.7(d), and 4.7(f)). The composites shown in Figs. 4.7(b) and 4.7(d) showed cracks at the interface between the CNT blocks and the Al matrix. However, no cracks were observed at the CNT block/Al interface in the case of the composites shown in Figs. 4.7(f) and 4.7(h). During the infiltration process, the Cu layer reacted with molten Al. An amorphous layer is formed at the graphite/Al interface at 1033 K even in the absence of electroless plating [31]. Moreover, thermal stress was generated in solidification process [32, 33]. As the amorphous layer have a weak strength, the interface between CNT block and Al matrix might be teared by the thermal stress [33]. The generated thermal tress is discussed in following part. Figs. 4.7(b) and 4.7(h) reveal the presence of unbonded parts in the CNT blocks. These unbonded parts were the same as those observed in Fig. 4.5. As can be observed from Figs. 4.7(g) and 4.7(h), the Al matrix of the composite with the CNT block:Cu volume ratio of 3.7:6.3 showed IMCs (light-gray regions). The elemental distribution of this sample is shown in Fig. 4.8. To identify the IMCs, EPMA was carried out on the region marked with a cross in Fig. 4.8(a). The Al:C atomic ratio of the IMC region was found to be approximately 2:1. As shown in Figs. 4.8 (b)–4.8(d), the Al and Cu overlapped at the IMC regions, indicating the formation of Al-Cu IMCs. Thus, the IMC was identified to be Al_2Cu. The XRD patterns of the CNT block/Al composites are shown in Fig. 4.9. Only the composite with the CNT block:Cu ratio of 3.7:6.3 exhibited the Al_2Cu peak. The formation of Al_2Cu can be attributed to the rough surface of the Cu layer, which facilitated the reaction between Cu and molten Al. According to the phase diagram of the Al-Cu system, Al_2Cu was formed by crystallizing out of the liquid phase near the CNT blocks during the solidification process. In this sample, the fraction of Cu reacting with Al was higher than that in the other samples [31].

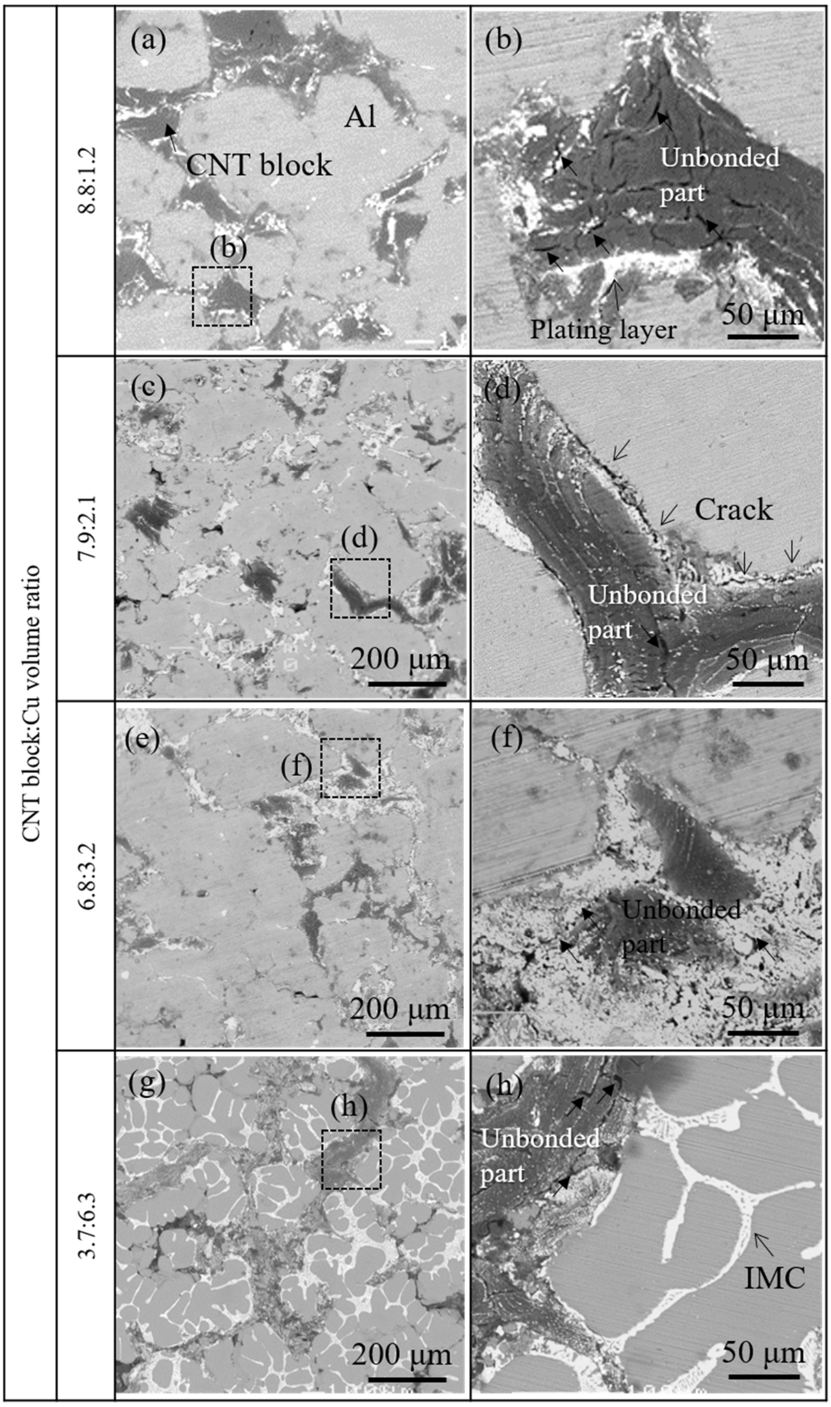

Fig. 4.7 SEM images of microstructures fabricated CNT block/Al composites with different CNT block:Cu volume ratios: (a) 8.8:1.2, (c) 7.9:2.1, (e) 6.8:3.2, and (g) 3.7:6.3; (b), (d), (f), and (h) high-magnification images of (a), (c), (e), and (g), respectively.

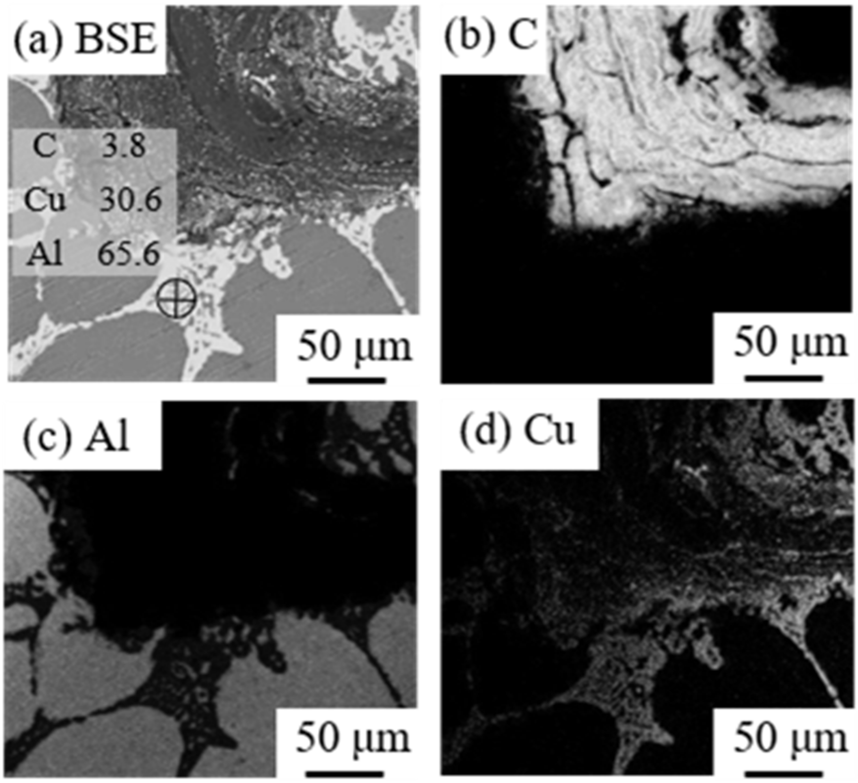

Fig. 4.8 Element distribution of fabricated CNT block/Al composite fabricated with condition of CNT block:Cu volume ratio of 3.7:6.3: (a) BSE image (inset for location and result of EPMA), (b) C element, (c) Al element, and (d) Cu element.

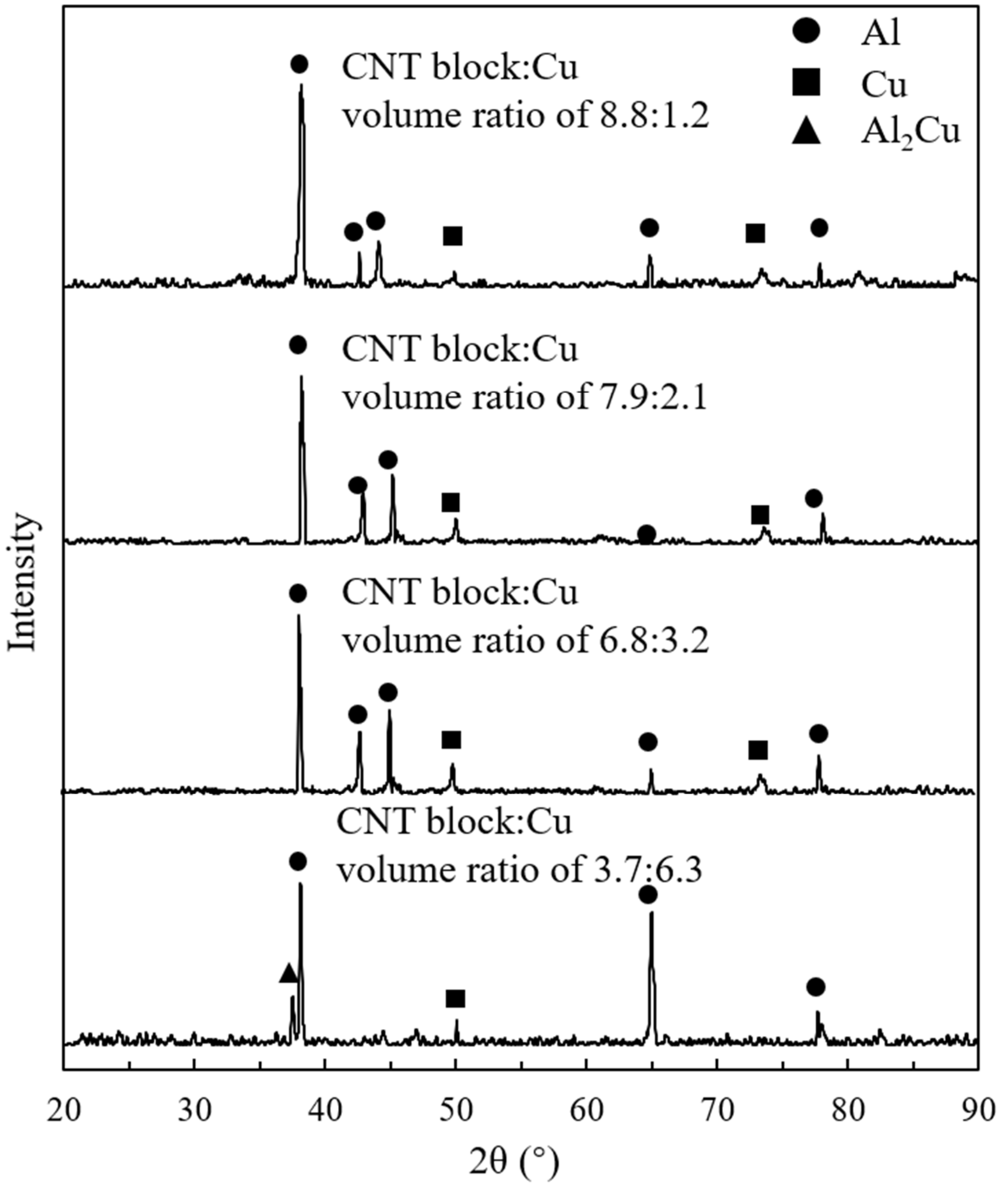

Fig. 4.9 XRD patterns of fabricated CNT block/Al composites with different CNT block:Cu volume ratios.

4.3.3 Thermal stress at the interface between CNT block and Al matrix

As the CNT and Al have different CTEs, there are thermal stress generated in the solidification process of fabrication of CNT block/Al composite. Therefore, the thermal stress at the interface between CNT block and Al matrix is studied. The schematic diagram of shrinkage of CNT block/Al composite is shown as 4.10. As shown in Fig. 4.10(a), at infiltration temperature, the CNT block and Al matrix were intimated bond. In this situation, which call initial state, the CNT block and Al matrix had a same length l. As shown in Fig. 4.10(b), supposing the interface strength between CNT block and Al matrix is zero, the CNT block and Al have a free shrinkage. The shrinkage of the CNT block and Al is different for different CTE. While supposing the interface strength between CNT block and Al matrix is efficient, as shown in Fig, 4.10(c), the thermal tress generated then effected the shrinkage of the CNT block and Al matrix. According this model, the thermal tress generated in the solidification can be calculated as following equations [32].

$$\alpha_t\phi_t=\alpha_m\phi_m \tag{4.2}$$

$$\varepsilon_l=\varepsilon_t=\varepsilon_m \tag{4.3}$$

$$\varepsilon_l=\alpha_l(T-T_0) \tag{4.4}$$

$$\varepsilon_t=\alpha_t(T-T_0)+\frac{\alpha_t}{E_t} \tag{4.5}$$

$$\varepsilon_m=\alpha_m(T-T_0)+\frac{\alpha_m}{E_m} \tag{4.6}$$

$$\sigma_t=E_tE_m\phi_m\frac{\alpha_m-\alpha_t}{E_t\phi_t+E_m\phi_m}\Delta T \tag{4.7}$$

$$\sigma_m=E_tE_m\phi_t\frac{\alpha_t-\alpha_m}{E_t\phi_t+E_m\phi_m}\Delta T \tag{4.8}$$

$$\varepsilon_m=\varepsilon_t=\frac{\alpha_tE_t\phi_t+\alpha_mE_m\phi_m}{E_t\phi_t+E_m\phi_m}\Delta T \tag{4.9}$$

where α is longitudinal CTE, Φ volume fraction, ε thermal expansion strain, σ thermal stress and E elastic modulus. And the l, t and m represent the total unit, CNT block and matrix, respectively. T0 and T are temperature at initial and a point in time. The parameters of CNT block and Al matrix is listed in Table 4.4.

Table. 4.4 CTE and elastic modulus of CNT and Al.

	α [×10^{-6}/K]	E [GPa]
CNT	−6	900
Al	22.3	69

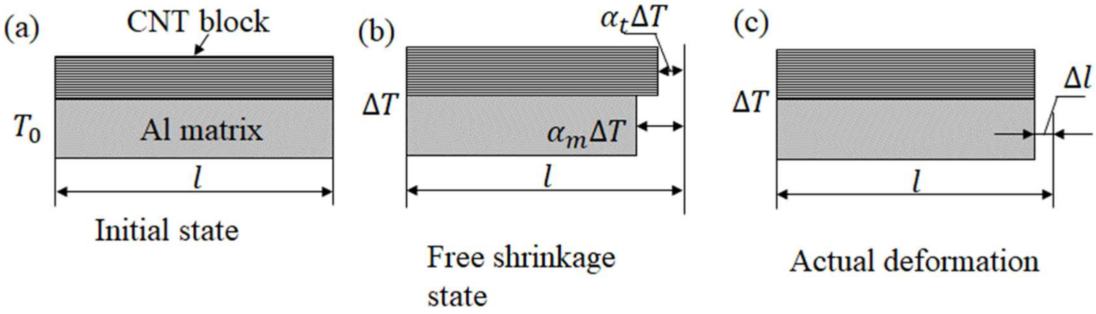

Fig. 4.10 The schematic diagram of shrinkage of CNT block/Al composite.

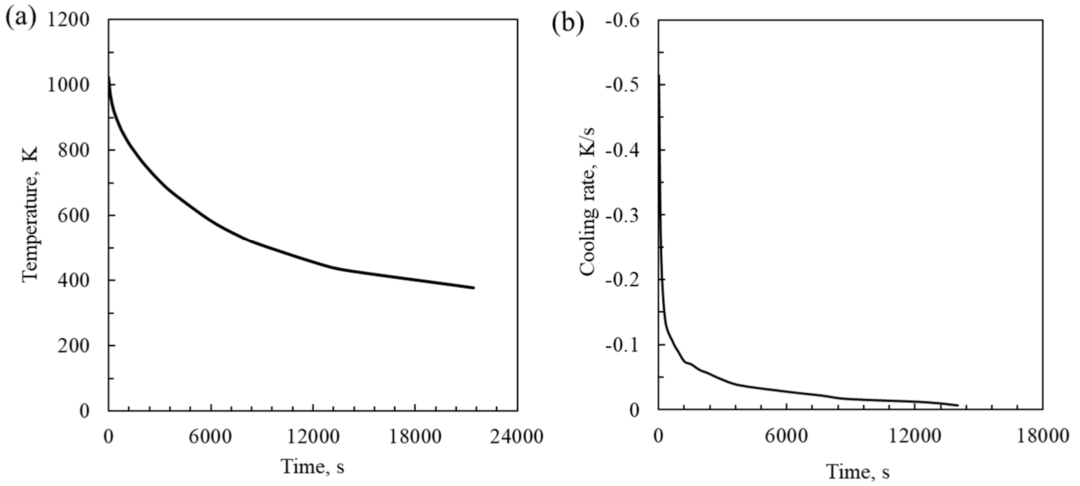

Fig. 4.11 (a) Temperature and (b) cooling rate of sample on condition of furnace cooling.

Fig. 4.11 shows the temperature and cooling rate of the CNT block/Al composite. The thermal stress of CNT block/Al composite, whose volume fraction of CNT block and Al matrix is 3.2% and 96.8%, is calculated, and the result is shown as 4.12. As shown in the Fig. 4.12, the thermal stress of this sample was increased to 13 MPa in solidification process. The amorphous layer is known to be very brittle and can sustain little compressive deformation [34, 35]. Thus, the thermal stress damaged the interface between CNT block and Al matrix without electroless Cu plating. Therefore, the damaged structure of the CNT blocks and thermal stress resulted in the formation of cracks at the CNT block/Al interface. Therefore, for the formation of the CNT block/Al interface, the Cu layer must have a sufficient thickness. Therefore, in this study, the insufficient Cu layer thickness resulted in the reaction of the CNT blocks and molten Al at the CNT block/Al interface, which was contribute to the intimate interface.

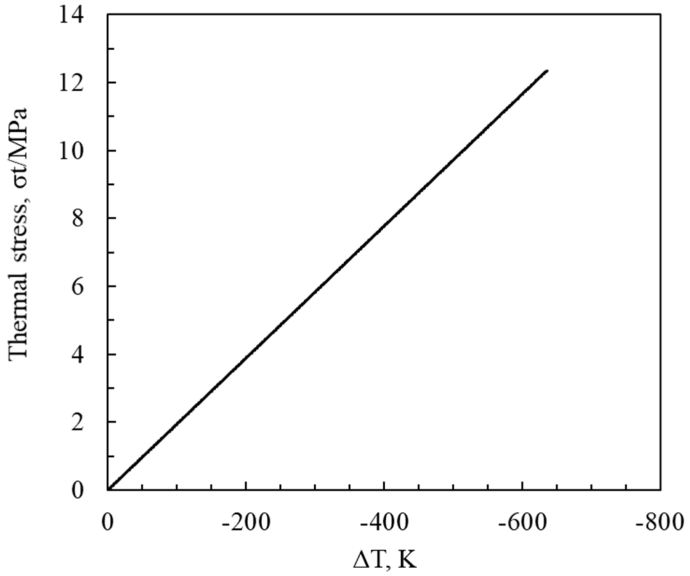

Fig. 4.12 Thermal stress on the interface between CNT block and Al matrix.

4.3.4 TC of the CNT block/Al composites

The TCs of the CNT block/Al composites fabricated with different CNT block:Cu volume ratios are shown in Fig. 4.13. As can be observed from Fig. 4.13, with an increase in volume fraction of Cu, the TCs of the composites increased because of the improvement in the CNT block/Al interface structure. However, with an increase in the CNT block:Cu ratio to 3.7:6.3, the TC of the CNT block/Al composite decreased. This decrease in the TC can be attributed to the formation of Al_2Cu, whose TC is approximately 60 $W \cdot m^{-1} \cdot K^{-1}$ [20]. This indicates that both the interfacial cracks and IMCs contributed to the decrease in the TC of the CNT block/Al composites. The TC of the CNT block/Al composite with the CNT block:Cu ratio of 6.8:3.2 was found to be 117 $W \cdot m^{-1} \cdot K^{-1}$, which is remarkably higher than that of a previously reported 10 vol.% dispersed carbon nanofiber-reinforced Al matrix composite (35.5 $W \cdot m^{-1} \cdot K^{-1}$, in Chapter 3). This is because the CNT blocks used in our composite did not aggregate. However, the TC of this composite was lower than those of Al (237 $W \cdot m^{-1} \cdot K^{-1}$) and Cu (385 $W \cdot m^{-1} \cdot K^{-1}$). This is because the thermal resistance at the CNT block/Al interface and the low real TC of the CNT blocks (compared to that of a single CNT). In the CNT blocks, the unbonded parts and thermal resistance at the CNT/CNT interface inhibited heat transfer, which resulted in a decrease in the real TC of the CNT blocks [36]. Hence, CNT blocks were found to be a potential reinforcement for MMCs. However, the thermal resistance of the CNT block/Al interface and the unbonded parts of the CNT blocks in CNT block/Al composites should be improved.

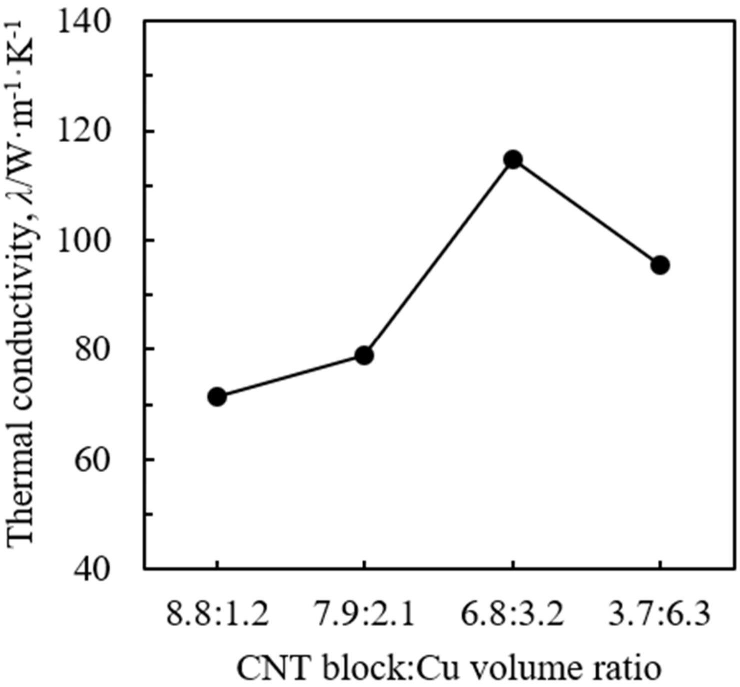

Fig. 4.13 TCs of fabricated CNT block/Al composites with different CNT block:Cu volume ratios.

4.4 Summary

CNT block preforms with high porosities were prepared by electroless Cu plating of CNT blocks for different plating times. CNT block/Al composites were successfully fabricated using the LPI method at 0.1 MPa. The main conclusions of the study are as follows:

(1) At the plating times of 15~60 s, the Cu layer wrapped the CNT blocks smoothly and uniformly. However, at the plating time of 180 s, dendritic growth occurred, making the surface of the Cu layer rough. The plating times used for the CNT block:Cu layer volume ratios of 8.8:1.2, 7.9:2.1, 6.8:3.2, and 3.7:6.3 were 15, 30, 60, and 180 s, respectively.

(2) No pores were observed in the CNT block/Al composites. The CNT block:Cu ratio of ≤ 6.8:3.2 improved the structure of the CNT block/Al matrix interface. The CNT block/Al composite with the CNT:Cu ratio of 3.7:6.3 showed IMCs, which were identified to be Al_2Cu and were formed by the reaction of Cu with Al. The formation of Al_2Cu can be attributed to the rough surface of the Cu layer, which facilitated the reaction between Cu and molten Al.

(3) At the area of insufficient thickness of electroless Cu plating, the cracks were happened at the interface between CNT block and Al matrix. The crack was a combination of the damaged structure of CNT block and thermal stress.

(4) With an increase in the volume fraction of Cu, the TCs of the fabricated CNT block/Al composites increased because of improvement in the structure of the CNT block/Al interface. However, at the CNT block:Cu ratio of 3.7:6.3, the TC of the CNT block/Al composite decreased because of the presence of Al_2Cu.

Reference

[1] S. Bakshi, D. Lahiri and A. Agarwal: Int. Mater. Rev. **55** (2010) 41-64.

[2] J. Liao and M.-J. Tan: Powder Technol. **208** (2011) 42-48.

[3] Q. Liu, L. Ke, F. Liu, C. Huang and L. Xing: Mater. Des. **45** (2013) 343-348.

[4] J. Che, T. Cagin and W. A. Goddard III: Nanotechnology. **11** (2000) 65.

[5] M. Lee, Y. Choi, K. Sugio, K. Matsugi and G. Sasaki: Compos. Sci. Technol. **97** (2014) 1-5.

[6] A. Nasiri, M. Shariaty-Niasar, A. Rashidi, A. Amrollahi and R. Khodafarin: Exp. Therm Fluid Sci. **35** (2011) 717-723.

[7] S. Jamali, M. C. Paiva and J. A. Covas: Polym. Test. **32** (2013) 701-707.

[8] P.-C. Ma, N. A. Siddiqui, G. Marom and J.-K. Kim: Composites Part A. **41** (2010) 1345-1367.

[9] H. H. Kim, J. S. S. Babu and C. G. Kang: Mater. Sci. Eng., A. **573** (2013) 92-99.

[10] D. H. Nam, S. I. Cha, B. K. Lim, H. M. Park, D. S. Han and S. H. Hong: Carbon. **50** (2012) 2417-2423.

[11] S. I. Oh, J. Y. Lim, Y. C. Kim, J. Yoon, G. H. Kim, J. Lee, Y. M. Sung and J. H. Han: Journal of Alloys & Compounds. **542** (2012) 111-117.

[12] C. R. Bradbury, J.-K. Gomon, L. Kollo, H. Kwon and M. Leparoux: J. Alloys Compd. **585** (2014) 362-367.

[13] A. Najimi and H. Shahverdi: Materials Science and Engineering: A. **702** (2017) 87-95.

[14] R. Pérez-Bustamante, F. Pérez-Bustamante, I. Estrada-Guel, L. Licea-Jiménez, M. Miki-Yoshida and R. Martínez-Sánchez: Mater. Charact. **75** (2013) 13-19.

[15] J.-F. Silvain, C. Vincent, J.-M. Heintz and N. Chandra: Compos. Sci. Technol. **69** (2009) 2474-2484.

[16] K. Chu, Q. Wu, C. Jia, X. Liang, J. Nie, W. Tian, G. Gai and H. Guo: Compos. Sci. Technol. **70** (2010) 298-304.

[17] Y. B. Choi, K. Matsugi, G. Sasaki and S. Kondoh: Mater. Trans. **49** (2008) 390-392.

[18] S. Ip, R. Sridhar, J. Toguri, T. Stephenson and A. Warner: Materials Science and Engineering: A. **244** (1998) 31-38.

[19] S. Ren, X. He, X. Qu, I. S. Humail and Y. Li: Materials Science and Engineering: A. **444** (2007) 112-119.

[20] Y. Terada, K. Ohkubo, T. Mohri and T. Suzuki: Mater. Trans. **43** (2002) 3167-3176.

[21] C. Leon, G. Mendoza-Suarez and R. A. Drew: Journal of materials science. **41** (2006) 5081-5087.

[22] L.-M. Ang, T. A. Hor, G.-Q. Xu, C.-h. Tung, S. Zhao and J. L. Wang: Chem. Mater. **11** (1999) 2115-2118.

[23] S.-Y. Chang, J.-H. Lin, S.-J. Lin and T. Z. Kattamis: Metallurgical and Materials Transactions A. **30** (1999) 1119-1136.

[24] H.-t. Kim, M. Kawahara and M. Tokita: Journal of the Japan Society of Powder and Powder Metallurgy. **47** (2000) 887-891.

[25] J.-F. Silvain, J.-L. Bobet and J.-M. Heintz: Composites Part A. **33** (2002) 1387-1390.

[26] F. Wang, S. Arai and M. Endo: Electrochem. Commun. **6** (2004) 1042-1044.

[27] H. Yang, Y. Lü, M. Chen and Z. Guo: Science in China Series G: Physics, Mechanics and Astronomy. **50** (2007) 407-413.

[28] F. Delogu: Physical Review B. **72** (2005) 205418.

[29] G. C. Efe, T. Yener, I. Altinsoy, M. İpek, S. Zeytin and C. Bindal: J. Alloys Compd. **509** (2011) 6036-6042.

[30] M. Reiter and H. Hartman: Journal of Geophysical Research. **76** (1971) 7047-7051.

[31] C. Zhou, G. Ji, Z. Chen, M. Wang, A. Addad, D. Schryvers and H. Wang: Mater. Des. **63** (2014) 719-728.

[32] T. Mishurova, S. Cabeza, G. Bruno and I. Sevostianov: International Journal of Engineering Science. **106** (2016) 245-261.

[33] H. Kurita, T. Miyazaki, A. Kawasaki, Y. Lu and J.-F. Silvain: Composites Part A. **73** (2015) 125-131.

[34] M. G. Fyta, I. N. Remediakis, P. C. Kelires and D. A. Papaconstantopoulos: Phys. Rev. Lett. **96** (2006) 185503.

[35] W. Yang, S. Mao, J. Yang, T. Shang, H. Song, J. Mabon, W. Swiech, J. R. Vance, Z. Yue and S. J. Dillon: Scientific reports. **6** (2016) 24187.

[36] E. Mayhew and V. Prakash: J. Appl. Phys. **115** (2014) 174306.

Chapter 5

Development of Graphene Reinforced Aluminum Matrix Composite by Spark Plasma Sintering

Contents

Contents 108

5.1 Introduction...109

5.2 Experimental 110

5.3 Results and Discussion 113

  5.3.1 Observation of composite powders...113

  3.3.2 Microstructures and phase analysis of Graphene/Al composites...............114

  3.3.3 TC of Graphene/Al composites 119

5.4 Summary 121

Reference..122

5.1 Introduction

Due to the increased market of intelligent car, the semiconductor component is widely used. Under working condition, semiconductor component generates heat, which may lead to overheat and thermal stress [1, 2]. To improve the satiability and save energy semiconductor component, the requirement of electronic packing material for semiconductor component is as high as thermal conductivity (TC), low coefficient of thermal expansion (CTE) and low density [1, 3, 4]. And workability of the heat sink material is also required to be processed into the desired shape [3]. The graphene has outstanding thermal property and ease of machining [5-8]. And aluminum has a low density, which has an advantage for application in intelligent car. Therefore, the graphene dispersed aluminum (Graphene/Al) composite is a promising candidate for electronic packing material.

There are certain key requirements to be fulfilled as a uniform dispersion of the graphene in the Al matrix in order to achieve an optimum thermal performance and good interfacial bonding between the reinforcement and the Al metal matrix. Because of this, mechanical alloying (MA) method is a technique frequently used to integrate a very fine distribution of particles into the metal matrix by solid-state powder processing without surface treatment [9-11], which is difficult to be obtained in the traditional way of liquid- solid method. In this study, MA method was utilized to fabricate composite power. Then the composite powder was sintered by Spark plasma sintering (SPS) method [12, 13] to fabricate Graphene/Al composite for the advantage of simple fabrication process.

As composite properties are affected by the dispersibility and volume fraction of the graphene particles, the effect of volume fraction of graphene and mixing method on the dispersibility was investigated in this study. Also, the microstructures and interface of Graphene/Al composites were observed. And the TC and mechanical properties of Graphene/Al composite were investigated.

5.2 Experimental

The graphene powder with diameter of 0.6 μm, thickness of 9.5 nm and carbon purity of >95% (Graphene Platform Co., Fig. 5.1(a)) was used as reinforcement. And pure aluminum powders with diameter of 3 μm (purity ≥ 99.9%, Fig. 5.1(b)), were used as matrix. The key steps of Graphene/Al composite powders were: (1) sonication and dry of aluminum powder and graphene; (2) mixing aluminum powder and graphene for mechanical alloying and (3) SPS sintering by SPS method. The schematic of the fabrication process for preparing the Graphene/Al composites is shown in Fig. 5.2. The samples were sintered at different temperatures. In particular, aluminum powders were added 10 vol.%, 20 vol.% and 30 vol.% of graphene, then were conducted with sonication (4.2 kHz) for 3.6 ks. Next, the zirconia balls to mixture ratio of 10:1 were mixed by V-type mixing with 45 RPM for 43.2 ks or by planetary ball milling with 150 RPM for 3.6 ks. The mixtures were pre-sintered with condition of pressure 15 MPa, pulse current 100 A, pulse voltage 50 V, pulse width 100 ms for 600 s. Then the mixtures were sintered at 813 K and a pressure of 80 MPa by SPS method. The fabrication conditions is listed in Table 5.1. The microstructures and interfaces of Graphene/Al composite were observed by scanning electron microscope (SEM; JEOL JXA8900; 15 kV) and field emission scanning electron microscope (FE-SEM; S-5200; 15 kV). Electron probe micro-analyzer (EPMA; JEOL JXA8900; 15 kV) was conducted for analyzing element distribution. The densities of Graphene/Al composite were tested by Archimedes method. X-Ray Diffraction (XRD JEOL JDX-11RA, Cu-Kα, 40.0 kV 40mA) was carried out using Cu Kα radiation (λ = 1.54056 Å) at a scanning speed of 1 °/min over the 2θ range of 20°~90°. And the TC and mechanical properties of Graphene/Al composites were investigated by steady state method [14].

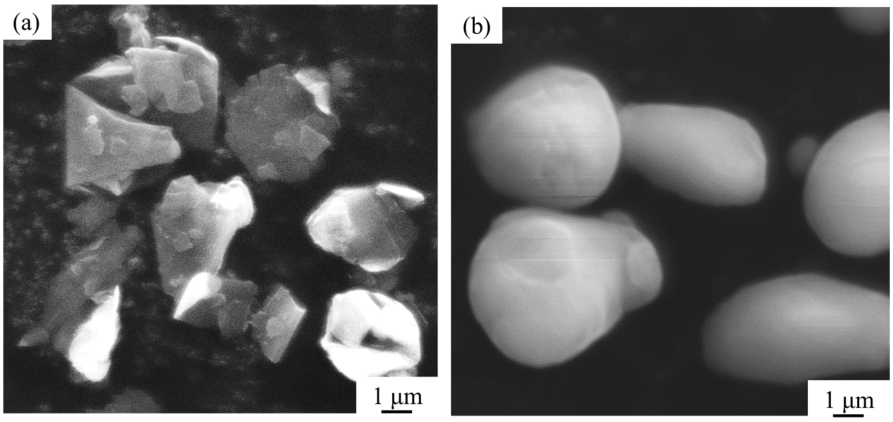

Fig. 5.1 SEM image of as received (a) graphene particles and (b) aluminum powders.

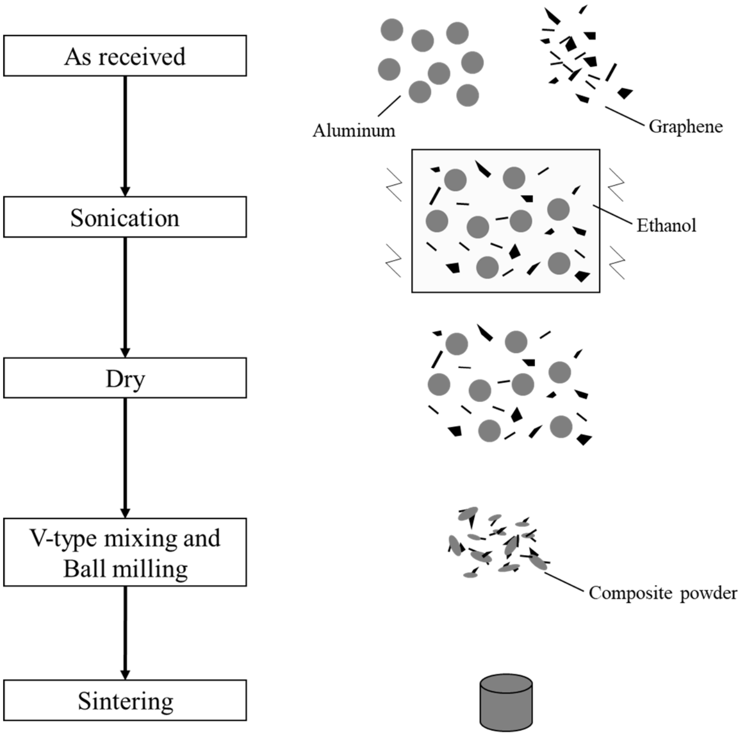

Fig. 5.2 The schematic of the fabrication process for preparing the Graphene/Al composites.

Table 5.1 Fabrication conditions of Graphene/Al composites.

No.	Volume fraction of reinforcement (%)	Sintering conditions	
		Temperature [K]	Pressure [MPa]
1	10	773	80
2		793	
3		813	
4		863	
5	20	813	
6	30		
7	40		

5.3 Results and Discussion

5.3.1 Observation of composite powders

SEM images of composite powders mixed by V-type mixing and planetary ball milling are shown as Fig. 5.3. As shown in Fig. 5.3(a), the powders were squashed with almost no combination. While comparing with composite powders in Fig. 5.3(a), the powders fabricated by planetary ball milling were agglomerated in complex shapes (see Fig. 5.3(b)). The reason was planetary ball milling proved more energy, then leading repeated shear fracture of the powders. By the impaction of balls, the graphene powers were inserted into aluminum powders. Therefore, the aluminum powders and graphene powders, as composite powders, were mechanical alloyed planetary ball milling. Thus, the Graphene/Al composites were fabricated by planetary ball milled composite powder.

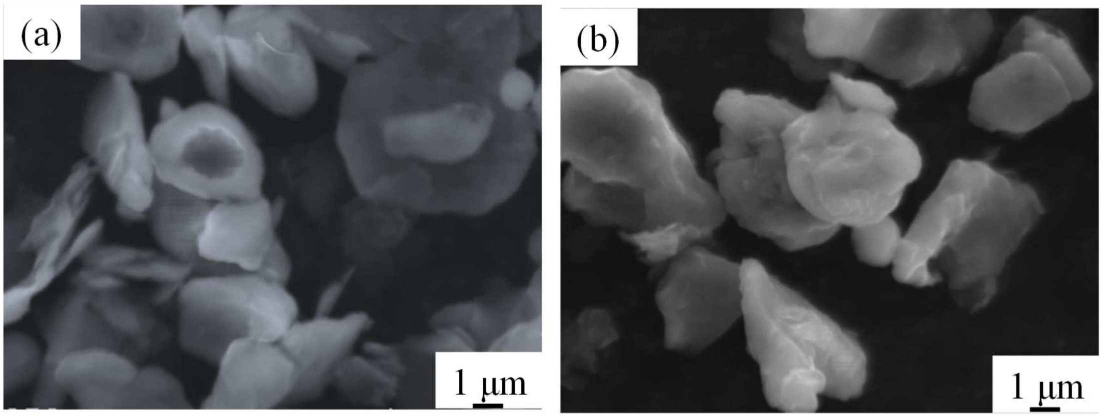

Fig. 5.3 SEM images of powder composites fabricated by

(a) V-type mixing and (b) by planetary ball milling.

5.3.2 Microstructures and phase analysis of Graphene/Al composites

Graphene/Al composite were fabricated using 10 vol.% graphene, at a pressure of 80MPa and different sintering temperature of 773, 793, and 813K. The SEM images of the cross section of the composite material is shown in Fig. 5.4. In Fig. 5.4(a) and 5.4

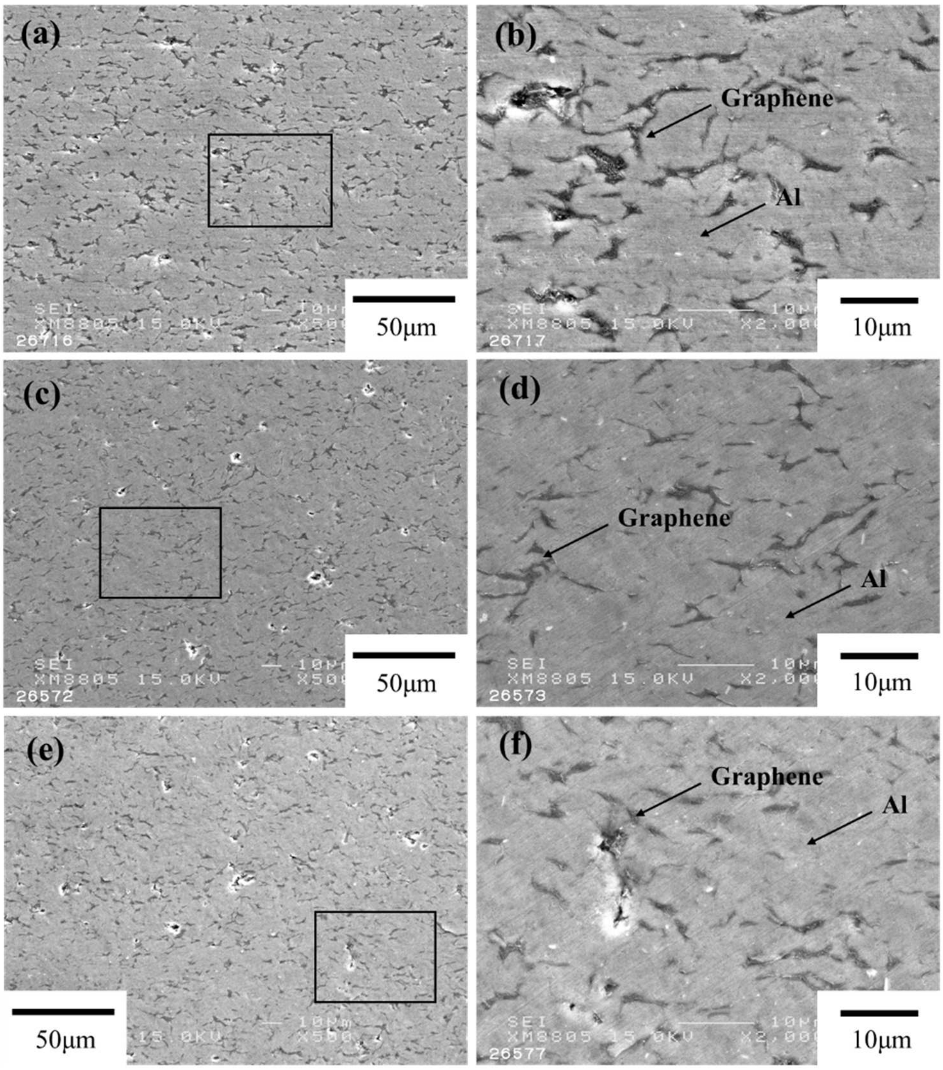

Fig. 5.4 SEM images of Graphene/Al composites (10 vol.% graphene) with different sintering temperatures: (a) 773K, (c) 793K and (e) 813K; high magnifications of (a), (c) and (e), respectively.

(b), the Al particles around the reinforcement was not densified, whereas the samples sintered at 793 and 813K, the Al particles were completely densified. On the other hand, there was no big difference in the numbers of defects. Thus, it is considered that sintering at 793K was effective in the solid phase sintering region from the viewpoint of avoidance of reactivity at high temperature and energy saving.

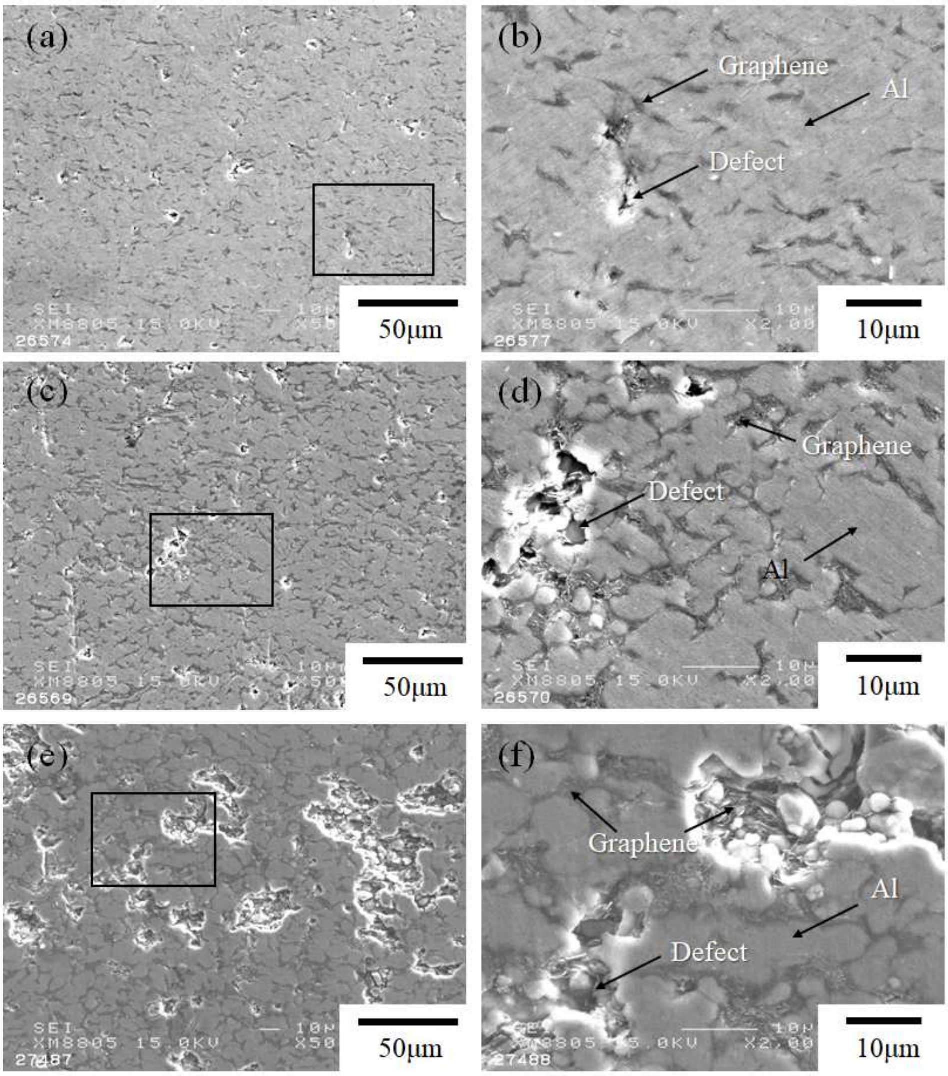

Fig. 5.5 SEM images of Graphene/Al composite with different volume fractions: (a) 10 vol.%, (c) 20 vol.% and (e) 30 vol.%; high magnifications of (a), (c) and (e), respectively.

Fig. 5.5 shows the microstructures of Graphene/Al composites fabricated with different volume fractions of graphene powders. The light gray parts were graphene and the dark gray parts were aluminum. As shown in Fig. 5.5, the graphene phases as reinforcement were easily to connect to each other with increasing volume fractions of graphene powders, but the pores as defects also increased. Moreover, the relative density of Graphene/Al composite with 10 vol.%, 20 vol.% and 30 vol.% graphene was 98.2%, 95.2% and 93.2%, respectively.

Fig. 5.6 shows FE-SEM images of the interface between aluminum matrix and graphene. The thickness of graphene was about 220 nm which is above the thickness of as-received graphene particles. This result was caused by the easy aggregation of graphene powders. Defects in 10 vol.% Graphene/Al composite and its element distribution are shown as Fig. 5.7. As shown in Fig. 5.7(a) and 5.7(b), the defects were formed by aggerated graphene in the Graphene/Al composite. In Fig. 5.7(b), there were no diffusion of carbon in aluminum matrix. For a further analysis, the XRD was

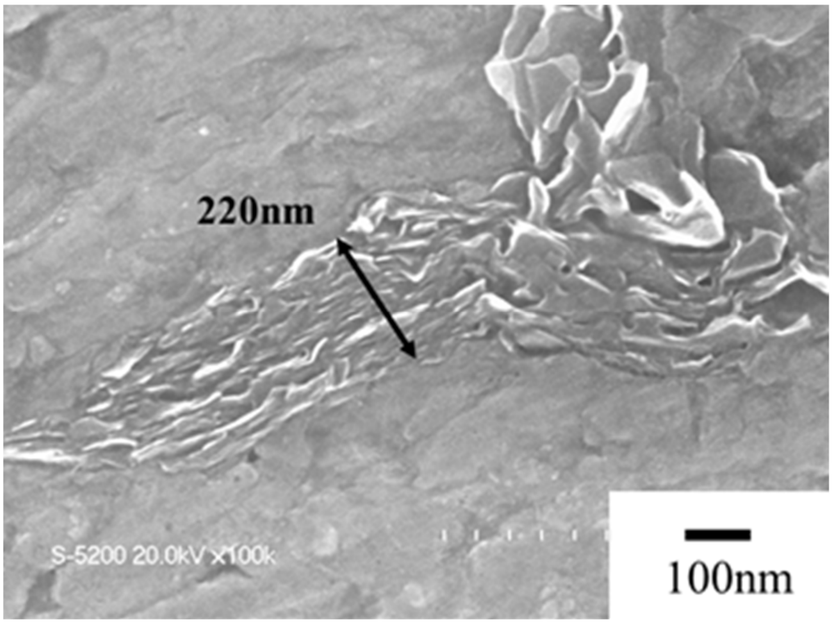

Fig. 5.6 Interface of Graphene/Al composite.

conducted on with Graphene/Al composites, and result of the XRD patterns of this sample is shown in Fig. 5.8. As shown in Fig. 5.8, XRD patterns shows only the diffraction peaks of Al and graphite. No evidence of Al_4C_3 indicates that this phase was not formed in the Graphene/Al composite.

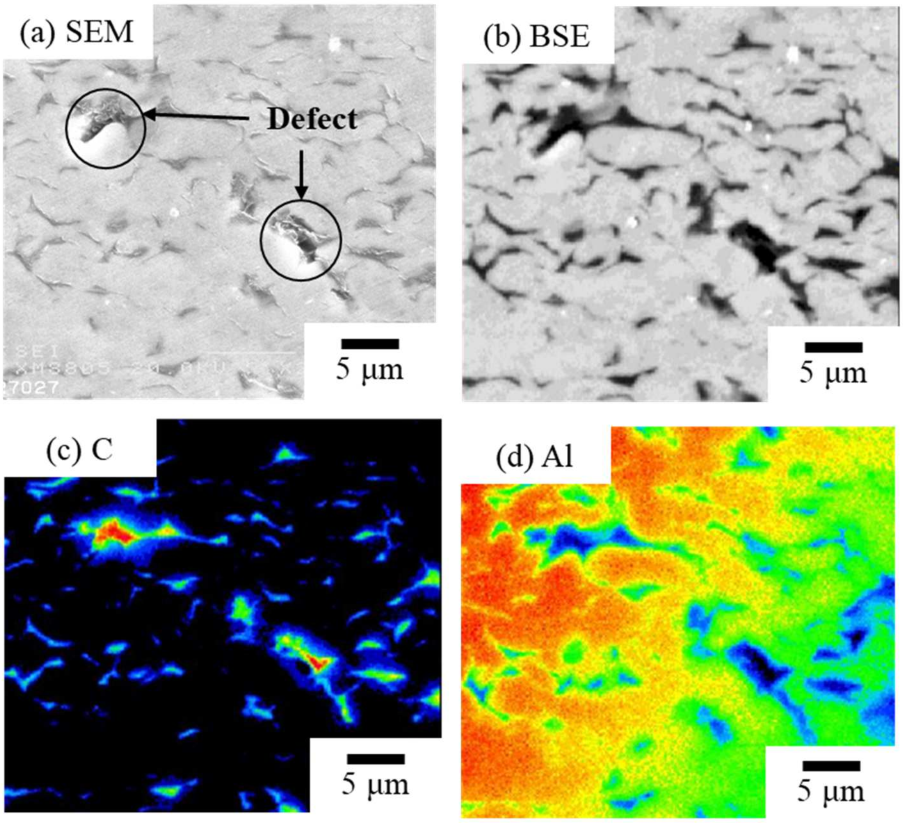

Fig. 5.7 (a) Defects in 10 vol.% Graphene/Al composite and its element distribution: (b) BSE image, (c) C element and (d) Al element.

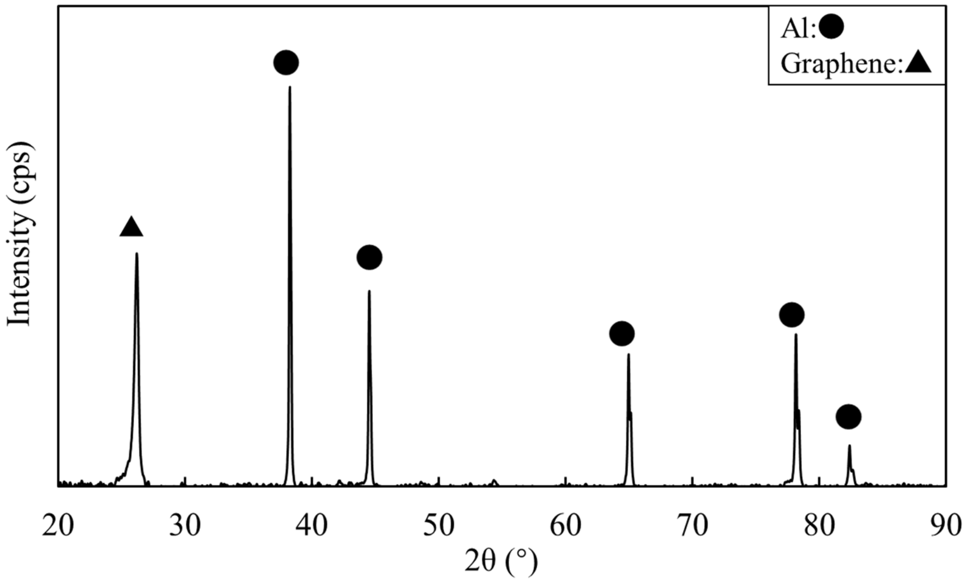

Fig. 5.8 XRD pattern of 10 vol.% Graphene/Al composite.

5.3.3 TC and hardness of Graphene/Al composites

The TCs of pure aluminum sintered with same conditions and Graphene/Al composites are shown as Fig. 5.9. The TCs of Graphene/Al composites were lower than the pure aluminum for low relative density [15] and thermal resistance. But, the TC of Graphene/Al composites with 20 vol.% graphene was higher than Graphene/Al composites with 10 vol.% graphene. The reason was graphene formed a continuous phase in the composite, then reduced the effect of thermal resistance. However, the TC of Graphene/Al composites with 30 vol.% graphene was further decreased owning to the defects. As those defects were formed by aggerated graphene, As the graphene can be dispersed by simple acid treatment, the Graphene/Al composites is thought to achieve less defects by dispersed graphene. On the other side, there are reports that addition of 5 vol.% Al-Si alloy power into the pure Al powder achieved a graphite

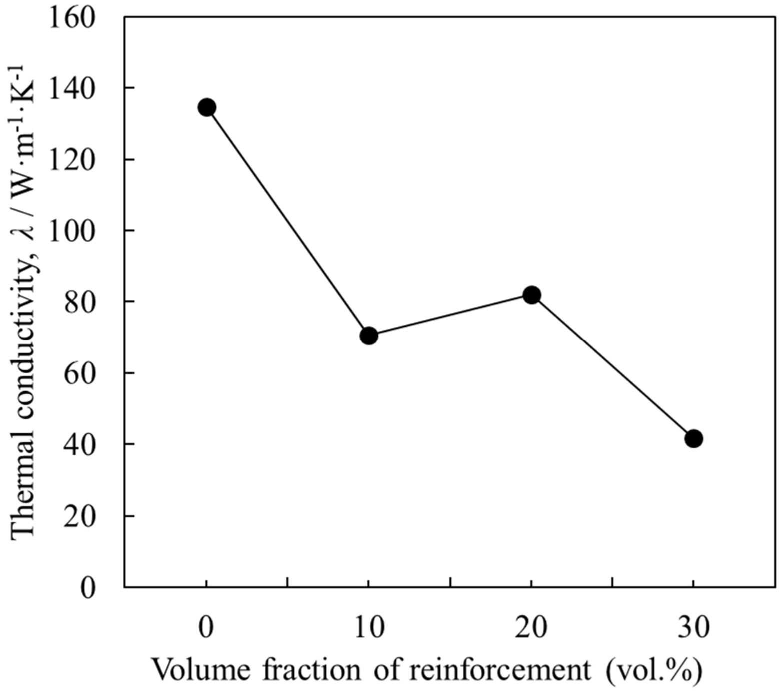

Fig. 5.9 TC of Graphene/Al composites with different volume fraction of graphene.

reinforced Al matrix composite, which was fabricated by hot pressing [16], have a relative density. Thus, the Graphene/Al composites are promising composite and need a further study on their fabrication process.

The Vickers hardness of pure aluminum sintered with same conditions and Graphene/Al composites are shown as Fig. 5.10. The Vickers hardness of Graphene/Al composite with 10 vol.% graphene was improved than pure aluminum for reinforcement of graphene. However, the Vickers hardness of Graphene/Al composites were decreased with increasing volume fraction of graphene for decreasing relative density.

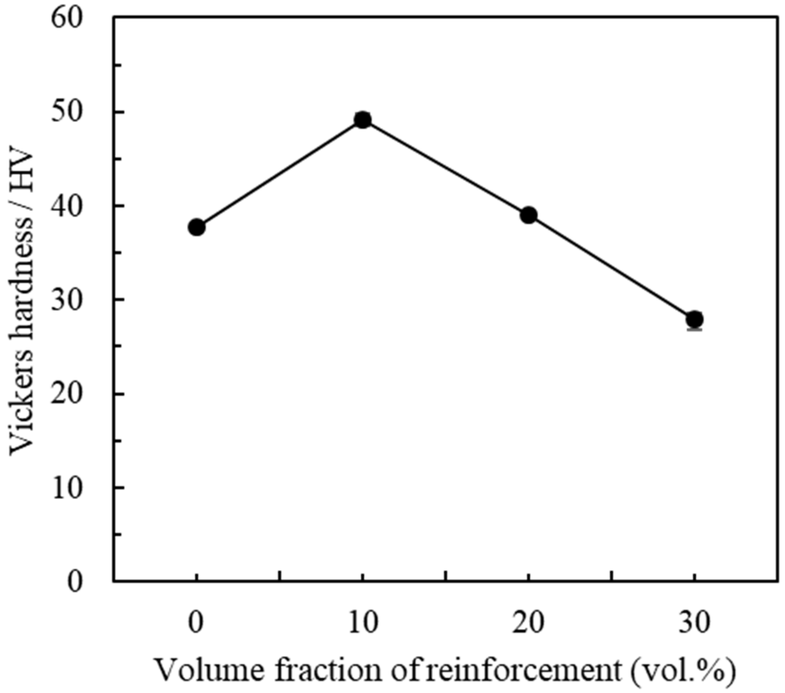

Fig. 5.10 Vickers hardness of Graphene/Al composites with different volume fraction of graphene.

5.4 Summary

Graphene and Al composite powders were fabricated by mechanical alloying method and Graphene/Al composite was fabricated by spark plasma sintering process. The main conclusions are as follow:

(1) Aluminum powders and graphene powders, as composite powders, were mechanical alloyed planetary ball milling. Graphene powders was attached on the aluminum power surface.

(2) Defects were formed by agglomerated graphene. And the defects were increased with increasing volume fraction of graphene.

(3) The TCs of Graphene/Al composites were lower than pure aluminum for defects in composite and thermal resistance at interface. However, under condition of 20 vol.% graphene, TC was increased by continuous graphene. The Vickers hardness of Graphene/Al composites were decreased with increasing volume fraction of graphene for decreasing relative density.

Reference

[1] S. Mallik, N. Ekere, C. Best and R. Bhatti: Appl. Therm. Eng. **31** (2011) 355-362.

[2] C. Zweben: Journal of the Minerals, Metals and Materials Society. **44** (1992) 15-23.

[3] X. H. Qu, L. Zhang, M. Wu and S. B. Ren: Progress in Natural Science-Materials International. **21** (2011) 189-197.

[4] P. K. Schelling, L. Shi and K. E. Goodson: Mater. Today. **8** (2005) 30-35.

[5] M. Fang, K. Wang, H. Lu, Y. Yang and S. Nutt: J. Mater. Chem. **19** (2009) 7098-7105.

[6] K. Chu, X.-h. Wang, F. Wang, Y.-b. Li, D.-j. Huang, H. Liu, W.-l. Ma, F.-x. Liu and H. Zhang: Carbon. **127** (2018) 102-112.

[7] S. C. Tjong: Mat. Sci. Eng. R. **74** (2013) 281-350.

[8] A. A. Balandin: Nature materials. **10** (2011) 569-581.

[9] C. Suryanarayana: Prog. Mater Sci. **46** (2001) 1-184.

[10] R. Pérez-Bustamante, F. Pérez-Bustamante, I. Estrada-Guel, L. Licea-Jiménez, M. Miki-Yoshida and R. Martínez-Sánchez: Mater. Charact. **75** (2013) 13-19.

[11] J. Fogagnolo, F. Velasco, M. Robert and J. Torralba: Materials Science and Engineering: A. **342** (2003) 131-143.

[12] K. Mizuuchi, K. Inoue, Y. Agari, Y. Morisada, M. Sugioka, M. Tanaka, T. Takeuchi, J.-i. Tani, M. Kawahara and Y. Makino: Composites Part B. **42** (2011) 825-831.

[13] B. Dun, X. Jia, C. Jia and K. Chu: Rare Metals. **30** (2011) 189-194.

[14] M. Reiter and H. Hartman: J. Geophys. Res. **76** (1971) 7047-7051.

[15] S. Ren, X. He, X. Qu and Y. Li: J. Alloys Compd. **455** (2008) 424-431.

[16] S.-Y. Chang, J.-H. Lin, S.-J. Lin and T. Z. Kattamis: Metallurgical and Materials Transactions A. **30** (1999) 1119-1136.

Chapter 6

Conclusion

The object of this thesis is to develop the carbon nanofiber/carbon nanotube/graphene composites with a cost effective fabrication process, for the application of replacement the conventional materials applying to the electronics industries. In this study, the VGCF/MP/Al composites and CNT block/Al composites were fabricated by low pressure infiltration process which enables complex/large shape and cost saving fabrication. Besides, the fabrication conditions for the VGCF/MP preform, CNT block preform, and composites fabricated by each preform were investigated to accomplish. Also, graphene/Al composites were fabricated by SPS method. Meanwhile, the thermal conductivity and the influence of the interfacial reaction on the thermal conductivity of fabricated composites were examined. The conclusions of this thesis are summarized as follows:

1. The study on the fabrication route and conditions for the high porosity of VGCF/MP preform and VGCF/MP/Al composites (Chapter 2, 3).

Prior to the fabrication of VGCF/MP/Al composites by the low pressure infiltration process, the fabrication conditions for the VGCF/MP preform by spacer method was studied. The NaCl particles were selected as spacers between VGCF/MP to maintain the continuous pores for the smooth infiltration of molten Al into the preform and appropriate compressive strength against the applied infiltration pressure. Moreover, the carbonization and electroless Ni plating were contributed to improve the thermal conductivity of VGCF/MP preform and improve the wettability between VGCF/MP preform and Al matrix. From these results, the VGCF/MP preform possessed the proper strength against the infiltration pressure and an advantage of wettability to Al infiltration hence it enabled the fabrication of VGCF/MP/Al composites by low pressure infiltration.

In the low pressure infiltration process, the variables such as capillary resistance pressure, internal friction, back pressure, gravity were considered to predict the initial infiltration pressure. The infiltration of molten Al into the VGCF/MP preform initiated over the calculated infiltration pressure and succeeded.

VGCF/MP/Al composites with anisotropy were achieved by the VGCF/MP as a continuous phase in the Al matrix. But the voids with same shape of NaCl particle were observed in the VGCF/MP/Al composites for the closed pores. The VGCF/MP/Al composites with the addition of 0–0.5 vol.% VGCFs had an intimated interface between VGCF/MP and Al matrix. While with the addition of 3 vol.% VGCFs, void was formed for the aggregation of VGCF/MP. The Al_3Ni was formed by the reaction of the Ni plating and Al matrix in infiltration process.

With the carbonization and addition of 0.5 vol.% VGCFs, the TCs of the VGCF/MP/Al composites increased because of the crystallization of the MP and the high TC of the VGCF. However, with addition of 0.5 vol.% VGCFs, the TC of the VGCF/MP/Al composite decreased because of the aggregation of VGCFs. And the Al_3Ni in Al matrix was also an unfavorable factor to the TC of VGCF/MP/Al composites.

2. The study on the fabrication route and conditions for the high porosity of CNT block preform and CNT block/Al composites (Chapter 4).

At the plating times of 15~60 s, the Cu layer wrapped the CNT blocks smoothly and uniformly. However, at the plating time of 180 s, dendritic growth occurred, making the surface of the Cu layer rough.

CNT block preforms with high porosities were prepared by electroless Cu plating of CNT blocks for different plating times. CNT block/Al composites were successfully fabricated using the LPI method at 0.1 MPa. The CNT block/Al composite with the CNT:Cu ratio of 3.7:6.3 showed IMCs, which were identified to be Al_2Cu and were formed by the reaction of Cu with Al. The formation of Al_2Cu can be attributed to the rough surface of the Cu layer, which facilitated the reaction between Cu and molten Al.

The thickness of electroless Cu plating was proved to be important to the CNT block/Al matrix interface. At the area of insufficient thickness of electroless Cu plating, the cracks were happened at the interface between CNT block and Al matrix. The crack was a combination of the damaged structure of CNT block and thermal stress.

With an increase in the volume fraction of Cu, the TCs of the fabricated CNT block/Al composites increased because of improvement in the structure of the CNT block/Al interface. However, the TC of the CNT block/Al composite decreased because of the presence of Al_2Cu formed by the reaction of Al matrix and over plated Cu on CNT block.

3. Graphene and Al composite powders was utilized to fabricate graphene/Al composite by spark plasma sintering process (Chapter 5).

Aluminum powders and graphene powders were mechanical alloyed planetary ball milling. Graphene powders was attached on the aluminum power surface. As to the graphene/Al composites, defects were formed at the area of aggerated graphene. And the defects were increased with increasing volume fraction of graphene.

The TCs of graphene/Al composites were lower than pure aluminum for defects in composite and thermal resistance at interface. However, under condition of 20 vol.% graphene, TC was increased by continuous graphene.

Acknowledgements

I would like to express my sincere gratitude to Associate Professor Yongbum Choi for his great guidance and insight throughout this study. He gave me full support not only on my research, but also on my life and career, which has played an important role in both of my professional and personal development. I am also greatly indebted Professor Kazuhiro Matsugi. He gave me so much positive help on the research, the accumulation of the knowledge and my life, and I have learnt so much from them. In addition, I would like to express my heartfelt thanks to Professor Gen Sasaki and Associate Professor Kenjiro Sugio for their technical advice and experimental assistance.

I would like to thank Mr. Shaoming Kang, Mr. Xuan Meng, Mr. Ning Wang, Mr. Yujiao Ke, Mr. Xilong Ma and Mr. Zeze Xiao for considerable assistance and help in my experiments and my life. Moreover, I would also like to thank all the past and present members of Property Control of Materials Laboratory, in Department of Mechanical Physical Engineering, Hiroshima University, for their enthusiastic help to both of my life and study.

Finally, my thanks would go to my beloved family for their loving considerations and great confidence in me all through these years. Grateful to my fiancée for unconditional support and care over the years. I also owe my sincere gratitude to my friends who gave me their help and time in helping me work out my problems during the difficult course of the thesis.

Published papers regarding this thesis

1. **F. Gao**, Y. B. Choi, K. Matsugi. Development of VGCF/MP Reinforced Al Matrix Composite by Low Pressure Infiltration Method and Their Thermal Property. Materials Transactions, submitted (Chapter 2 & 3).
2. **F. Gao**, Y. B. Choi, K. Matsugi. Fabrication and Thermal Conductivity of Carbon Nanofiber Reinforced Aluminum Matrix Composites by Low Pressure Infiltration Casting. 21st International Conference on Composite Materials, in China, August 2017 (Chapter 2).
3. **F. Gao**, Y. B. Choi, K. Matsugi. Microstructure and Thermal Conductivity of Carbon Nanotube Block-Reinforced Aluminum Matrix Composite. Materials Transactions, Vol. 61, No. 4 (2020) pp. 626 to 631 (Chapter 4).
4. **F. Gao**, Y. B. Choi, Y. Dobashi and K. Matsugi. Development of Graphene Reinforced Metal Matrix Composite by Spark Plasma Sintering. International Journal of Engineering & Technology. Vol. 7, (2018) pp. 76 to 79 (Chapter 5).

Presentations

1. **Fei Gao**, Moonhee Lee, Youqiang Yao, Yongbum Choi, Zhefeng Xu, Kazuhiro Matsugi, Kenjiro Sugio and Gen Sasaki: Development of manufacturing process of porous vgcf and their mechanical property. The 10th Asian-Australasian Conference on Composite Materials, October 16 - 19, 2016, Busan, Korea.

2. 高　飛、崔　龍範、松木　一弘、杉尾　健次郎：低圧含浸法による炭素ナノファイバー強化アルミニウム基複合材料の作製及び熱特性。日本複合材料学会 第４４回複合材料シンポジウム、2019 年 9 月、岡山理科大学。

3. **Fei Gao**, Yongbum Choi, Kazuhiro Matsugi, Kenjiro Sugio, Hiroyuki Suzuki: Fabrication and characterization of porous material using CNTs block for fabrication of matrix composites materials. The technical program of the 10th Pacific Rim International Conference on Advance Materials and Processing (PRICM-10), August 2019, Xi'an, China, pp. 117.

4. **Fei Gao**, Yongbum Choi, Kazuhiro Matsugi, Zhefeng Xu, Kenjiro Sugio and Gen Sasaki: Fabrication and thermal conductivity of carbon nanofiber reinforced aluminum matrix composites by low pressure infiltration casting. 21st International Conference on Composite Materials,20-25th August 2017, Xi'an, China.

5. **Fei Gao**, Yongbum Choi, Kazuhiro Matsugi and Gen Sasaki Fabrication of porous carbon nano fiber with high porosity and their thermal property. International Journal of Engineering & Technology. 金属学会 2018 年秋期講演大会、仙台、2018 年 9 月。

6. 高　飛、崔　龍範、松木　一弘、許　哲峰：Fabrication of carbon nanofiber reinforced aluminum matrix composites by low pressure infiltration method 第 9 回軽金属学会中国四国支部 講演大会、愛媛、2017 年 7 月。

7. **高　飛**、崔　龍範、松木　一弘、許　哲峰、佐々木　元、杉尾　健次郎：カーボンナノチューブを用いた多孔体の製造プロセスの開発及びその圧縮特性、第８回軽金属学会中国四国支部　講演大会、鳥取、2016年7月。

Awards

1. 第９回 軽金属学会中国四国支部 講演大会、優秀講演賞、2016年7月29日、愛媛、日本。

2. The 10th Asian-Australasian Conference on Composite Materials, The best presentation award, October 18, 2016, Busan, Korea.